Modelling the cross-shore grain size distribution in the intertidal zone

R. Breedveld

Modelling the cross-shore grain size distribution in the intertidal zone

by

R.Breedveld

in partial fulfilment of the requirements for the degree of

Master of Science
in Civil Engineering

at the Delft University of Technology,
to be defended publicly on Monday March 28, 2022 at 14:00.

Student number:	4499298	
Thesis committee:	prof. dr. ir. A.J.H.M. Reniers,	TU Delft, chair
	dr. S.E. Vos,	TU Delft, daily supervisor
	C.O. van IJzendoorn, MSc,	TU Delft
	dr.ir. S De Vries	TU Delft

An electronic version of this thesis is available at `http://repository.tudelft.nl/`.

Summary

The Building with Nature approach has been gaining ground in hydraulic engineering, increasing the importance of understanding the cross-shore morphodynamic processes. The cross-shore profile is continuously adapting to the varying conditions at the beach. The intertidal zone, where marine and aeolian processes come together, is an important link in the transport of sediment from the sea towards the dunes. The sediment grain size affects the sediment supply in the intertidal zone. This research investigates the effect of marine processes on the cross-shore variations of the grain size distribution in the intertidal zone by using a one-dimensional non linear shallow water XBeach model.

The intertidal zone is subject to shoaling, surf and swash zone processes. The grain size affects the beach slope — and as such the beach states and wave conditions — the initiation of motion and settling to the bed. The cross-shore sediment transport contains contributions of sediment that is stirred up from the bed and subsequently transported. Breaking induced turbulence enhanced the stirring of sediment from the bed and keeps sediment in suspension. The amount of stirring and the direction of transport is dependent on the wave conditions.

Input and control data for the model study was provided by the Scanex fieldwork campaign at Noordwijk, the Netherlands, that took place from February to April 2020. The ADV velocity data combined with a pressure signal has been used to obtain the tidal and incoming wave signal. The ADV data has been filtered for quality based on the Signal to Noise value, the pulse correlation and an outlier correction. Cross-shore profiles have been determined in Matlab by fitting a surface to terrestrial laser scan point clouds. For the initial profile a 20 m long horizontal offshore extension was added and interpolation was used to fill in the gap between the bed level at the ADV and the laser scan profile. Soil samples of the 2 mm top layer were taken with a sand scraper and analyzed with a sieve tower. The initial grain size distribution has been computed as the averaged distribution of 14 samples along a cross-shore transect. Based on wave, wind and soil sampling data a model period from 29-2-2020 02:00 to 10-3-2020 13:00 was selected.

The XBeach model used is as described by Reniers et al. (2013), but with a time-averaged turbulent kinetic energy and a different implementation of the Riemann boundary. The model consisted of a 176 x 3 grid with a grid size of dx = 1 m and dy = 5 m. For the initial bathymetry the laser scan of 29-2-2020 02:00 was used. The initial grain size was imposed on all the model grid cells and layers. Additional to the standard run other runs have been performed. The five-day run is used to investigate the effect of a storm at the start of the model period. One day long sensitivity runs have been performed to investigate the response of the model to seven different parameters. The aeolian run simulates the effect of aeolian transport that has likely taken place over the model period.

The model shows a pattern of cross-shore grain size variations with coarser sediment from x = 20 to x = 56 m, finer sediment from x = 57 to x = 105 m and fluctuating grain size from x = 106 to x = 136 with respect to the initial grainsize. After 24 h the grain size pattern establishes after 24 hours with a clear deposition of fine sediment on the upper beach. The pattern remained stable for nearly the full model period. After 200 hours the fines become less prominent and move onshore. On the intratidal scale sediment becomes coarser when submerged and finer when emerged, except near the high water line where fine sediment is deposited.

Measurement uncertainties were introduced to the soil sampling, caused by local variations in the grain size and human activity. Limitations of the model are related to the model stability, the bed composition over the vertical and the alongshore processes, creating differences between the model and the situation on the beach. The modelled grain size was found to be very sensitive to the position of the ADV, and to a lesser extent to the adaptation.

The XBeach model showed an overactive morphological response around the intertidal bar, but higher in the intertidal zone the differences with the laser scan profile were small. The model was able to reproduce

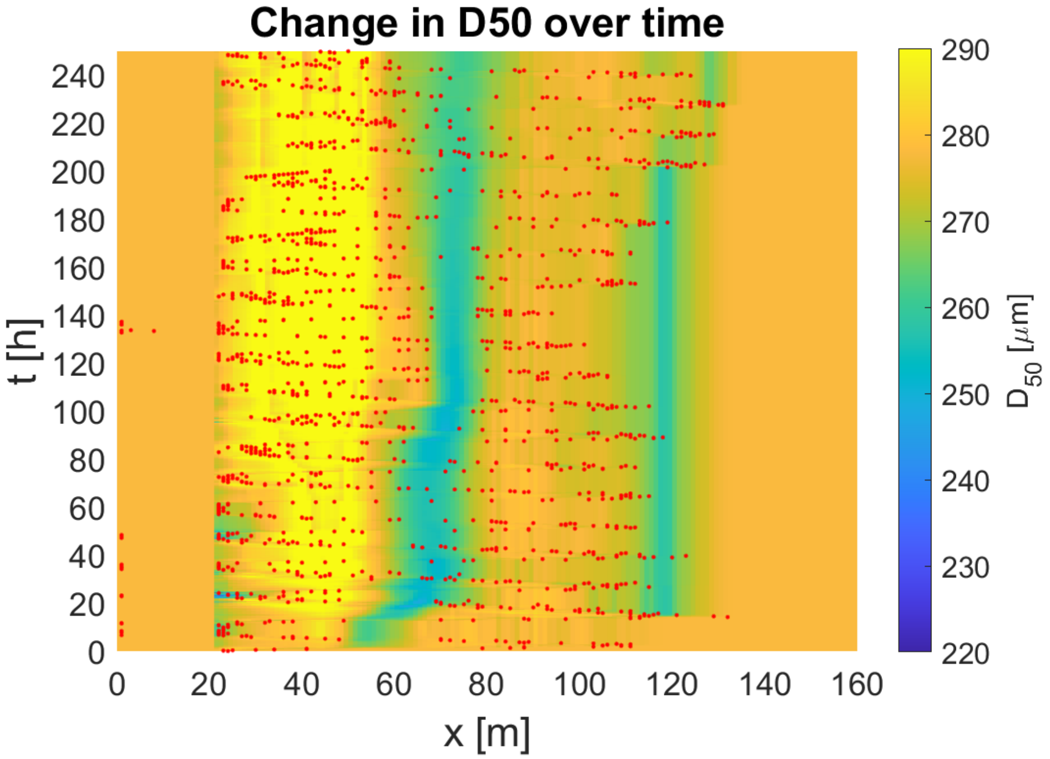

Figure 1: Modelled grain size over the model period. The position of the waterline is marked with red dots.

the same pattern of grain size variations over the cross-shore as was found in the soil samples of 10-3. As the cross-shore grain size pattern remained stable during the model period, processes on the spring-neap time scale or storm time scale seem to govern the cross-shore variations of the grain size. As a correctly modelled bathymetry is an indication of correctly modelled grain size distribution, the relation between the morphology and grain size was investigated. A correlation was found between the change in bed level and the change in grain size with respect to the initial bathymetry.

Taking into account the aeolian transport can lead to coarser sediment in the upper intertidal zone and a better fitting model result. The aeolian simulation was very crude in time and space. To fully include the effect of aeolian transport, XBeach should be coupled with an aeolian transport model. The stable cross-shore grain size distribution implies that for aeolian transport the fine sediment supply is controlled on on the spring-neap tidal time scale or the storm time scale, just like the cross-shore grain size. Nevertheless, considering that aeolian transport could have resulted in coarsening of the fines in the upper intertidal zone, processes over a single tide, could have been more important than is visible in the model result.

To conclude, on the intratidal time scale fine sediment is deposited near the high water line. On the intertidal time scale a stable pattern for the cross-shore grain size distribution is established, in which the contributions of the single tides are not very noticeable. It seems that for the considered model period the cross-shore grain size distribution and consequently the fine sediment supply were controlled by processes on the spring-neap tidal time scale or storm time scale, but because of aeolian transport in the upper intertidal zone, processes on the intratidal time scale, could have been more important than the model result shows.

Preface

This thesis is the final part for completing my master degree in Hydraulic Engineering at the TU Delft. I would be lying if I said it wasn't a struggle, but now that it is done, I know that I can be proud of completing my thesis.

First of all, I would like to thank my graduation committee. I couldn't have wished for a more involved committee and I feel very lucky that you were there to guide me. You were always available to talk, brainstorm and provide feedback. During the meetings your excitement was contagious and helped me remember that I was actually doing pretty cool stuff. A special thanks also goes out to Anneloes, who helped me navigate the swamp which is the process of writing a thesis. Lastly, I would like to thank my family, friends and of course my boyfriend, for supporting me during my master thesis and all the years of studying leading up to it.

Rosanne Breedveld
Amersfoort, March 2022

List of Symbols

A	constant.
a	1. near-bed reference level. 2. wave amplitude.
C	1. average concentration. 2. empirical sediment sorting coefficient. 3. Chezy coefficient.
c	1. concentration. 2.wave celerity.
C_a	concentration at near-bed reference level $z = a$.
C_D	drag coefficient.
c_{eq}	equilibrium concentration.
c_f	friction factor.
c_g	wave group velocity.
c_k	calibration factor for the turbulent kinetic energy sink.
c_r	calibration factor for the turbulent kinetic energy source.
C_s	sediment concentration.
D	reference grain diameter, 0.25 mm.
d	1. grain diameter. 2. water depth.
D_{50}	median grain size.
d_{ADV}	water depth at the location of the ADV.
d_j	characteristic diameter of the jth sediment class.
eps	threshold water depth above which cells are considered wet.
F_F	friction force.
F_D	drag force.
F_{dr}	driving force.
F_L	lift force.
F_{ret}	retaining force.
F_S	shear force.
g	gravitational constant.
H	wave height.
h	water depth.
H_b	wave height at breaking.
h_{min}	threshold water depth above which Stokes drift is taken into account.
k	wave number, $2\pi/L$.
$\overline{k}$	time averaged turbulent kinetic energy.

K	1. dynamic wave pressure correction factor. 2. horizontal diffusivity coefficient.
k_{bed}	near bed turbulent kinetic energy.
L_0	deep water wave length.
m_{cr}	critical slope of wave front.
n	porosity.
p	pressure.
p_j	sediment fraction of the jth sediment class.
q	aeolian sediment transport capacity.
Q_s	total aeolian sediment transport.
R	roller thickness.
Re_*	grain Reynolds number.
s	relative density, $\frac{\rho_s}{\rho}$.
S_b	bed load sediment transport.
S_r	turbulent kinetic energy sink.
S_s	suspended sediment transport.
S_t	total sediment transport.
S_w	turbulent kinetic energy source.
S_x	sediment transport in cross-shore direction.
S_y	sediment transport in alongshore direction.
t	time.
T_{rep}	representative period for turbulent kinetic energy averaging.
T_s	adaptation time.
U	time-averaged velocity.
$\overline{u}$	mean cross-shore velocity.
u	velocity in cross-shore direction.
U_0	mean Longuet Higgins streaming velocity.
$\hat{u}_0$	mean free stream velocity.
u_c	critical velocity.
u_{high}	time varying flow on the short wave timescale.
u_{low}	time varying flow on the wave group timescale.
U_s	sediment velocity.
u_{*c}	critical shear velocity.
u_*	shear velocity.
u_{wind}	wind velocity in the cross-shore direction.
v	velocity in alongshore direction.
v_{wind}	wind veloctiy in the alongshore direction.
W	weight.
w	vertical velocity.
w_s	fall velocity.
x	cross-shore position.

y	alongshore position.
z	vertical position.
z_b	bed level.
	.
β	bed slope.
β_s	slope parameter.
γ	calibration factor for the adaptation time T_s.
γ_b	breaker index.
Δ	relative density, $\frac{\rho_s-\rho}{\rho}$.
ϵ_s	suspended load efficiency.
η	surface elevation.
η_{cr}	critical surface elevation for breaking waves.
θ'	shear stress acting on the grain.
θ_{cr}	critical Shields parameter.
κ	Von Karman constant, 0.4.
ν	kinematic viscosity.
ν_h	turbulent horizontal viscosity.
$\nu_{h,fac}$	roller induced turbulent horizontal viscosity.
$\nu_{t,s}$	turbulent diffusivity.
ξ	Irribarren number.
ρ	density.
ρ_{air}	air density.
ρ_s	sediment density.
τ_b	bed shear stress.
τ_{bx}	bed shear stress in cross-shore direction.
τ_c	critical bed shear stress.
Φ_b	dimensionless bed load transport.
Φ_t	bed load transport parameter.
ω	wave frequency, $2\pi/T$.

List of Figures

Contents

1

Introduction

In recent years Building with Nature has been gaining ground in hydraulic engineering. The Building with Nature approach strives to design sustainable solutions starting from an understanding of the natural and societal systems it is acting on. It aims to optimize ecological value and uses the natural systems at hand (de Vriend et al., 2015). An example of Building with Nature is the Dutch coastal management strategy of sand nourishments that was implemented in 1990 and is still in place today. As of 2003 the nourishments have been placed in the shoreface where possible, which has resulted in the stabilization of the dune foot (Van der Spek & Lodder, 2015). The sand is transported towards the dunes via naturally occurring processes such as wave, current and wind forcing. Under influence of these processes the cross-shore beach profile is continuously adapting, resulting not only in changes to the bathymetry, but also to the grain size distribution.

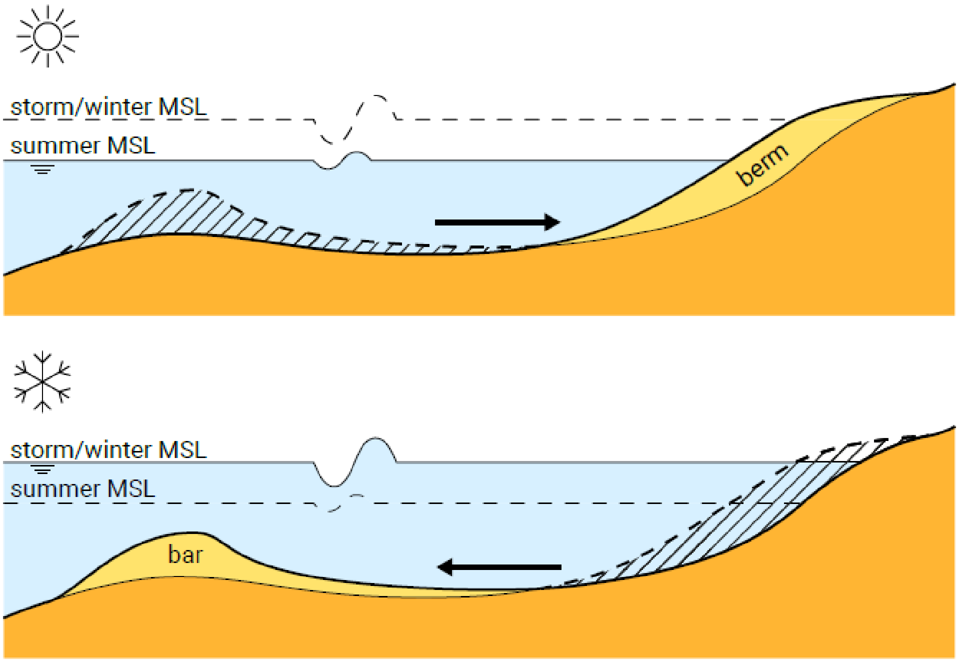

Figure 1.1: Summer and winter cross-shore profile (Bosboom & Stive, 2015)

The cross-shore beach profile is the cross-section of the beach taken perpendicularly to the direction of the coast. Depending on the wave conditions the profile will adjust differently. During high energy wave conditions, the undertow will be the dominant cross-shore process and sediment will be transported offshore. The beach slope will flatten and sediment will be stored on a subtidal bar. Under low wave energy conditions, wave asymmetry and skewness are governing. Sand from the subtidal bar is deposited on the beach, creating a berm and resulting in a steeper slope (Bosboom & Stive, 2015). Since high energy conditions are more frequent in winter and low energy conditions in summer, the corresponding profiles are referred to a summer and winter beach profile (fig. 1.1; Bosboom and Stive (2015)).

The intertidal zone is a very morphodynamically active part of the cross-shore profile. It is defined as the region of the beach between high tide and low tide. In the intertidal zone marine and aeolian processes come together. While the upper beach is only subject to aeolian processes, and the nearshore only to hydraulic processes, the intertidal zone experiences both.

When the intertidal zone is submerged, it is under the influence of marine processes. In the cross-shore direction the intertidal zone can be subject to either shoaling, surf and swash zone processes depending on the water depth. Waves will transform and become more skewed and asymmetric, until they eventually break. The waves continue towards shore and run up and down the beach in the swash zone. The breaking of waves and the interaction with the bed add turbulence to the water column stirring sediment from the bed. The sediment is then transported by currents, such as the undertow, wave orbital motion and the swash flows.

As the intertidal zone emerges the beach becomes affected by the wind. High wind velocities do not necessarily correspond to the largest sediment transport rates (De Vries, Stive, Van Rijn, & Ranasinghe, 2012), since the sediment supply available for aeolian transport can be limited. In the intertidal zone aeolian sediment transport is first limited by the moisture content, but as the beach dries grains are picked up by the wind. This aeolian transport favors the finer sediment and is active on the 2 mm top layer of the bed.

The interaction between wind and waves in the intertidal zone is already found within a period of a single tide, or on the intratidal time scale. Due to changing wave, wind and tidal conditions the interaction can vary between different tides or on the intertidal time scale. The aeolian transport takes place in a small active surface layer of 2-3 mm (Van Rijn, 2019). Therefore, most interaction between marine and aeolian transport is expected in this top layer.

The grain size distribution is a very important factor in controlling what happens in the intertidal zone. The median grain size D_{50} is representative for the size of the sediment particles. It is found in formulations for the initiation of motion, the fall velocity and the sediment transport rates. The grading of the sediment is an indicator for the uniformity of the sediment. Variations in grain diameter result in a certain amount of exposure or hiding (Van Rijn, 1997) and are required for armoring — the formation of a layer of coarse sediment, protecting the smaller grains in the bed below (Hoonhout & de Vries, 2017).

The marine processes and their effect on the grain size distribution can be modelled with the XBeach one-dimensional non linear shallow water model (XBeach 1D NLSW model). It is a hydraulic numerical model that solves for individual waves in shallow water, that only considers the processes in the cross-shore direction (Reniers et al., 2013). XBeach can model the grain size distribution, as for each individual grid cell the grain size distribution can be specified with multiple sediment grain size classes. These sediment classes are then taken into account, when computing the sediment transports and updating the bed level and bed composition.

1.1. Problem statement

The transition to sandy solutions in coastal management strategies increases the need for understanding the morphological processes responsible for transporting sediment from the sea towards the dunes. Transport of sediment in the intertidal zone is greatly dependent on the grain size distribution, as fine sediment particles are more easily picked up than coarse particles. In the intertidal zone sediment is mixed, eroded and deposited under influence of marine processes, resulting in variations in the grain size distribution over the width of the intertidal zone as well as over time.

As a location in the intertidal zone can be subject to many different marine processes over the course of one single tide, changes in the grain size distribution on the intratidal scale are of interest. Furthermore, the spring-neap cycle and the wave conditions determine where in the intertidal zone which processes are found, resulting in changes on the intertidal time scale. Investigating the effect of marine processes on the grain size distribution on both time scales will provide insight in where and when sediment is available for transport in the intertidal zone.

The grain size variations that are established in the intertidal zone under marine influence, could have important consequences for the aeolian transport of sand towards the dunes. It is hypothesized that not the upper beach but the intertidal zone is the most important source of sediment for the dunes (De Vries, Harley, De Schipper, & Ruessink, 2015). A study of the beach profile at three different locations showed that dune growth occurred even though the upper beach profile remained nearly the same. The stable upper beach can be explained by the formation of an armor layer, limiting the sediment supply. This suggests that the dune growth can be attributed to sediment transports originating from the intertidal zone. Thus, investigating the cross-shore grain size distribution in the intertidal zone could lead to better understanding the full chain of events leading to sediment deposition in the dunes.

Modelling the bed composition of the intertidal zone can done on much smaller spatial and temporal scales than the alternative method of taking soil samples in the field. Therefore, the XBeach 1D NLSW model can provide more detail on the changes to the grain size distribution caused by marine processes, while being less time consuming. In order for the modelled grain size distribution to be valid, the model should be a correct representation of the beach. By analyzing the model performance and which processes the modelled grain size distribution is most sensitive to, the model limitations are better understood and future XBeach model setup and calibration can be improved.

1.2. Research objective

The aim of this thesis is to determine how marine processes influence the cross-shore grain size variations in the top layer of the intertidal zone.

Five research questions have been formulated to achieve this:

RQ1 What are the dominant cross-shore processes for modeling the grain size distribution on the beach?

RQ2 How do marine processes change the grain size distribution of the top layer on a intra-tidal timescale?

RQ3 How do marine processes change the grain size distribution of the top layer on a inter-tidal timescale?

RQ4 What are the implications of the grain size variations in the intertidal zone for aeolian transport?

RQ5 To what extent is the XBeach 1D-NLSW model suitable for predicting the development of the grain size diameter in the field?

1.3. Thesis Approach

First, a literature study will be performed on the cross-shore processes that influence the grain size distribution and vice versa in order to answer RQ1. Then, the cross-shore grain size distributions will be modelled with the 1D NLSW XBeach model. As input for the model data gathered at the Scanex fieldwork campaign in Noordwijk will be used. The data will be processed to obtain the incoming wave and tidal signal, the initial cross-shore profile and initial bed composition. The model results are used to answer RQ 2,3 and 4. Lastly, the model end result is compared to the bed composition and morphology on the beach and the model sensitivity is tested. Both are used to answer RQ 5.

1.4. Thesis Structure

Chapter 2 will describe the processes in the intertidal zone that are important to this thesis. The focus will be on the cross-shore hydraulic processes. In order to better understand the effect the modelled the grain size distribution will have on the aeolian transport, a section on aeolian transport is included as well. Chapter 3 presents an overview of the ScanEx fieldwork campaign and the collected data. It describes the processing methods and presents the results of the data processing. Based on this data a model scenario is selected. Chapter 4 presents the information related to the XBeach model. It explains the choice for 1D-NLSW model, provides the model background and outlines the model setup. The model results will be presented in chapter 5 and discussed in chapter 6. In chapter 7 the conclusion will be presented and recommendations for improving the result and for further research are made.

2

Literature

This chapter presents a literature study on the most important cross-shore processes in the intertidal zone relevant to this research. First, it introduces the cross-shore profile and sediment characteristics used to describe the situation on the beach. Then, it discusses the movement of a single sediment particle, marine and aeolian transport and the wave generated turbulence important for sediment transport.

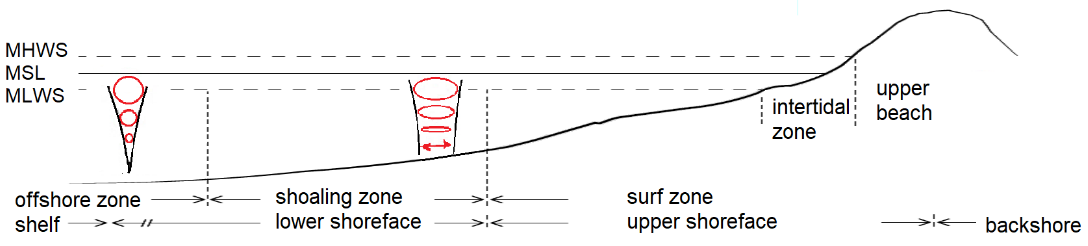

Figure 2.1: Overview of the cross-shore profile

2.1. Cross-shore profile

The cross-shore beach profile can be split into different regions based on the characteristic processes occurring in each (fig. 2.1). The main zones that can be distinguished are the offshore, shoaling and surf zone.

The offshore zone is characterized by waves that do not reach the bed. The water particles in a wave exhibit a circular orbital motion, with equal maximum horizontal and vertical velocities. The orbital velocities decrease with the water depth and go to zero.

In the shoaling zone waves do reach the bed and the wave characteristics change because of it. As the water depth decreases, the wave height increases and the wave length and wave celerity decrease. The waves become positively skewed with high narrow crests and low troughs. The orbital motion of the water particles becomes ellipsoid with smaller vertical velocities than horizontal velocities. Near the bed the vertical velocity approaches zero, while a horizontal velocity remains present that varies over the wave period.

The surf zone is characterized by breaking waves. Waves break when the water depth becomes too small. The wave height of a wave at breaking is related to the water depth via a breaker index γ (eq. 2.1; Bosboom and Stive (2015)). As the waves break, wave energy is dissipated. This generates an alongshore current, that is found only in the surf zone (Bosboom & Stive, 2015).

$$H_b = \gamma_b h \approx 0.88h \tag{2.1}$$

where:

H_b = wave height at breaking
γ_b = breaker index
h = water depth

At the waterline two additional regions can be defined. The waterline is the transition between water and land and varies in time. On the scale of a single wave, the wave will run up the beach, slow down and fall back due to gravity. The region between the maximum uprush and backwash is called the swash zone. At the offshore boundary of the swash zone the shore break is located, which is an area with a sudden steeper slope (Reniers et al., 2013). On a longer time scale the waterline varies with the tide. The intertidal zone is the part of the beach that is covered by water during high tide and emerges during low tide. Above the intertidal zone the upper or dry beach is predominantly under aeolian influence. Due to tidal variations it is possible that over time a fixed location in the intertidal zone is affected by shoaling, surf as well as swash motions. The slope of the cross-shore profile is related to the grain size, as generally, larger grain sizes correspond to steeper beach slopes (Bosboom & Stive, 2015). Figure 2.2 shows the relationship between the beach slope and the median grain size based on 2133 data points found in 78 published studies (Bujan et al., 2019). The beach slope increases rapidly with the grain size for fine and medium sand and slows down for coarse sand and gravel. However, this relation alone can't be used to predict the beach slope, since many other factors, such as grain shape, wave conditions and tidal range contribute as well and all these processes are interconnected (Bujan et al., 2019).

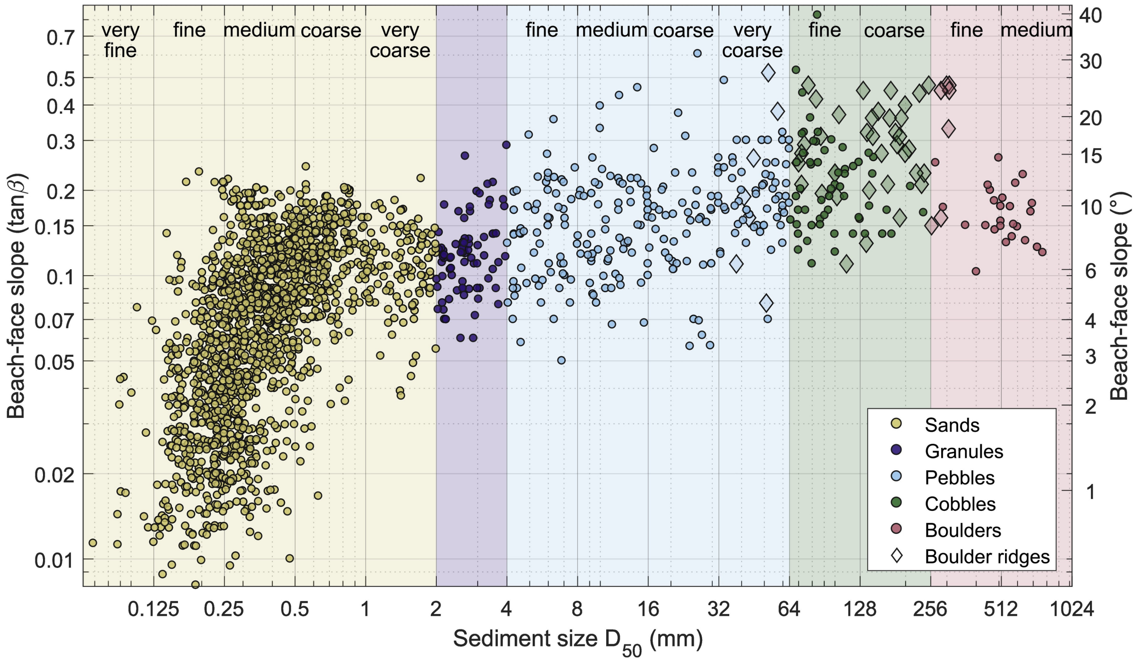

Figure 2.2: Beach slope versus grain size for 2133 published data points. Circles correspond to sand, gravel and boulder beaches, while diamonds correspond to supratidal boulder ridges. (Bujan et al., 2019)

2.2. Sediment characteristics

There are multiple ways that sediment can be classified, such as grain size, grain shape, the presence of organic material or the origin of the sediment. Classification based on grain size is the most straight-forward. The different sediment classes with their minimum and maximum diameter are presented in table 2.1 (Verruijt, 2002).

Sediment does not have to be uniform in size. The variability of the grain size can be described with a grain size distribution curve showing the mass percentage of the sediment that is smaller than a certain diameter (fig. 2.3) . The diameter D_x is used to describe the value for which x % of the sediment is smaller. Often the median grain size D_{50} is used as the characteristic grain size of the sediment. On one hand, a shallow

Sediment class	min. [mm]	max. [mm]
clay	-	0.002
silt	0.002	0.063
sand	0.063	2
gravel	2	63

Table 2.1: Soil classification based on grain size (Verruijt, 2002)

gradient in the distribution curve indicates that a sediment contains a wide range of sediment sizes. This is called poorly sorted or well graded sediment. On the other hand a steep curve corresponds to sediment without much variation. The sediment is well sorted or poorly graded. The steeper the distribution curve the more the sediment approaches a uniform grain size (Verruijt, 2002).

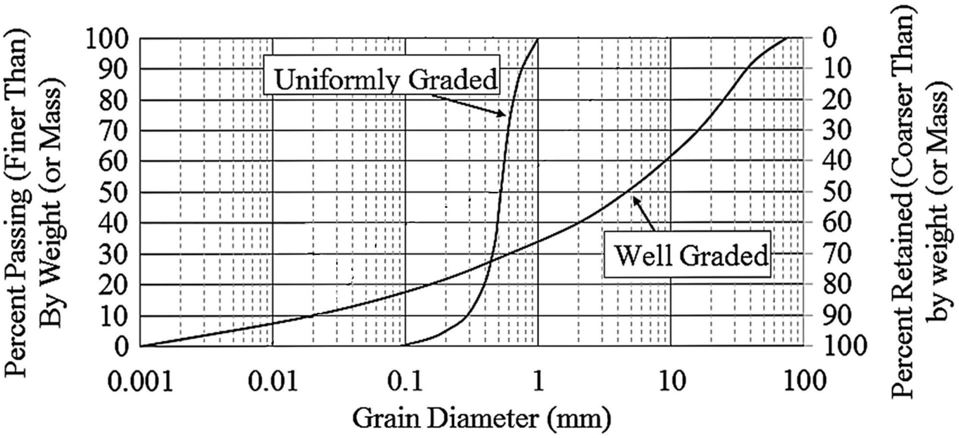

Figure 2.3: Grain size distribution curves. Adapted from: Shakoor,(2018)

2.3. Cross-shore and temporal variations of the grain size

The median grain size and the grain size distribution on the beach varies over the cross-shore profile. Van Rijn (1997) presented an overview of field studies on the grain size distribution for micro-tidal and meso-tidal regimes, showing all a similar pattern. Coarser sand is found in the swash zone at the shore break and sediment fining occurs in the onshore as well as offshore direction of the shore break. In the onshore direction this is caused by fine particles that are deposited higher on the beach by the uprush. In the offshore direction finer particles are brought into suspension and transported seaward by the return currents. Additionally, in the presence of breaker bars an alternating pattern of coarser grain size on the bar crests and finer grain size in the bar troughs is found.

Terwindt studied the grain size distribution on the beach of Katwijk, the Netherlands (1962). Katwijk beach is located 3 km south of Noordwijk and can be a good indicator of the expected grain size variations in this research. Coarser grains were found with a D_{50} of 0.3 mm close to the waterline. During calm conditions the grain size decreased to 0.14 mm at the offshore boundary and 0.22 mm at the dune top. In the surf zone the contribution to the bed composition of the different sediment fractions varied depending on the wave conditions. The largest variation was found for the light grain fraction of 0.105–0.150 mm. During calm conditions this fraction contributed 50% to the bed composition, while it reduced to 20% in storm conditions. During a storm the finer grains are suspended and moved offshore. In calmer conditions coarser sediment is transported back to the surf zone via bed load transport (Terwindt, 1962).

2.4. Forces on a sediment particle

Sediment transport is the volume of sediment particles that is moved over a period of time. Sediment particles on the bed are set into motion under hydraulic or aeolian forcing, are moved with the flow and eventually return to the bed. The transport of a single particle can be understood by looking at the forces that are acting on it. For a sediment particle that is brought into motion as well as for a sediment particle in the water column that is returning to the bed a force balance can be set up.

2.4.1. Initiation of motion

An individual grain is set into motion when the driving forces exceed the retaining forces (Schiereck, 2016). A grain that protrudes from the bed experiences a horizontal drag and shear force, F_D and F_S respectively, caused by the flow over it. The flow contracts around the particle and accelerates, leading to a decreased pressure and an upwards directed lift force F_L. Assuming the sediment particle is round, the driving forces are all proportional to $\rho u^2 d^2$ (eq. 2.2). In the vertical direction the driving forces are balanced by a gravitational force W and in the horizontal direction by a friction force F_F. As both retaining forces are dependent on the mass of the sediment particle, they are proportional to $\rho g d^3$ (eq. 2.3). By equating the lift force and the retaining force a critical velocity is found above which a particle will start to move (eq. 2.4). The difficulty is that this expression uses the the flow velocity near particle, but it is not well defined where this velocity should be determined (Schiereck, 2016).

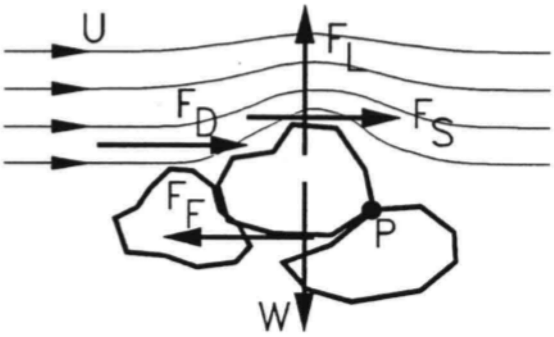

Figure 2.4: Forces acting on a grain under a flow (Schiereck, 2016).

$$F_{dr} \propto \rho u^2 d^2 \tag{2.2}$$

$$F_{ret} \propto (\rho_s - \rho) g d^3 \tag{2.3}$$

$$u_c = A\sqrt{\Delta g d} \tag{2.4}$$

where:

F_{dr} = driving force
F_{ret} = retaining force
ρ = fluid density
ρ_s = sediment density
u = flow velocity
d = grain diameter
g = gravitational constant
u_c = critical velocity
A = constant, ≈ 1.7
Δ = relative density, $\frac{\rho_s - \rho}{\rho}$

The density ρ used in the equations above is the density of the fluid the particle is exposed to. As such, the force balance can be used for a particle in water flow as well as aeolian flow as long as the right density is used. Since the density of air is an order of magnitude of 1000 smaller than the density of water, particles of the same size will have a larger critical velocity in water than in air.

The initiation of motion is often described with the Shields parameter (Schiereck, 2016). Shields used the same approach of a driving and retaining force, but selected the bed shear stress as the driving force (eq. 2.5). The Shields parameter is a dimensionless shear stress parameter, showing the ratio between the bed shear stress and the gravitational force (eq. 2.6). The critical Shields parameter was found to be a function of the grain Reynolds number Re_* (eq. 2.7) and the relation between the two is the well-known Shields curve. For large grain Reynolds numbers the critical Shields parameter becomes constant at 0.055 (Schiereck, 2016).

$$\tau_c = \rho u_{*c}^2 \tag{2.5}$$

$$\theta_{cr} = \frac{\tau_c d^2}{(\rho_s - \rho) g d^3} = \frac{u_{*c}^2}{\Delta g d} \tag{2.6}$$

$$R_e* = \frac{u_* d}{\nu} \tag{2.7}$$

where:

τ_c = critical bed shear stress
u_{*c} = critical shear velocity
u_* = shear velocity
θ_{cr} = critical Shields parameter
Re_* = grain Reynolds number
ν = kinematic viscosity

The Shields parameter was determined for uniform flow on a flat bed (Schiereck, 2016). In a coastal setting wave action, a sloping bed and ripple formation can't be neglected. To include the wave action a combined wave and current shear stress should be used.

2.4.2. Fall velocity

A sediment particle that has been suspended in the water column is subject to a downward gravitational force and an upward drag force caused by the flow along the particle. When these forces are in balance the particle will fall down with a constant velocity, which is called the fall velocity (Bosboom & Stive, 2015).

$$\frac{1}{2} C_D \rho \frac{\pi}{4} d^2 w_s^2 = (\rho_s - \rho) g \frac{\pi}{6} d^3 \tag{2.8}$$

$$w_s = \sqrt{\frac{4(s-1)gd}{3C_D}} \tag{2.9}$$

where:

C_D = drag coefficient
w_s = fall velocity
s = relative density, $\frac{\rho_s}{\rho}$

The drag coefficient is dependent on the grain Reynolds number. For Re_* smaller than 0.1–0.5 the drag coefficient is equal to $24/Re_*$ and for $Re_* > 400 - 210^5$ the drag coefficient is approximately 0.5. For sandy beaches the drag coefficient will most of the time be somewhere in between this range (Bosboom & Stive, 2015).

If the concentration of particles is high, the presence of other particles nearby will interfere with the settling. This hindered settling is slower than unhindered settling and is a function of the concentration.

A particle in motion can be subject to a settling lag and a scour lag. Settling lag is when a particle is advected by the flow, while the velocity is not high enough to keep it in suspension. A particle in suspension at depth h will take h/w_s to return to the bed, during which it can be transported by the flow (Gatto et al., 2017). Coarser grains will settle faster to the bed than fine grains and will settle nearly instantaneously. The finer the grain, the larger the settling lag. For very long settling times it is even possible that flow reversal has taken place before settling and that the transport direction has reversed. The scour lag is related to the fact that it is much easier for sediment to remain in suspension than it is to be suspended from the bed. Once the particle has settled a higher velocity will be needed to pick it up again (Masselink & Puleo, 2006).

2.4.3. Movement types

There are different ways in which a sediment particle can be set in motion. Once the critical flow velocity has been reached the sediment particles roll over the bed due to the direct pressure of the flow. Rolling can also occur below the critical flow velocity, if they are subject to faster-moving turbulent eddies. At higher wind speeds particles make small jumps from the bed, which is called saltation. The height of the jump is dependent on the initial upward velocity. Once lifted from the bed the particle gains momentum from the flow it is in. Upon return to the bed, the particle can hit a particle on the surface, which is then ejected from the bed and continues the saltation. However, most of the energy of the impact is transferred to a large number of particles that remain in the bed. The continuous impact of saltating grains returning to the bed, results in a slow surface creep. When the jump of a saltating particle becomes large enough, the particle becomes suspended. It will move with the same velocity as the flow velocity (Bagnold, 1941).

2.5. Sediment transport

Sediment transport is the volume of sediment particles that is moved over a period of time. When considering the transport over one meter width, the unit is $m^3/s/m$. Erosion or deposition of sediment occurs when there is a gradient in the sediment transports. The change in the bed level thickness can be seen as the difference between the sediment transports coming in and out of a control volume (eq. 2.10). The total sediment transport is a combination of the bed-load transport and suspended sediment transport (eq. 2.11), which will be discussed in their own subsections below (Bosboom & Stive, 2015).

$$(1-n)\frac{\partial z_b}{\partial t}+\frac{\partial S_x}{\partial x}+\frac{\partial S_y}{\partial y}=0 \tag{2.10}$$

$$S_t = S_b + S_s \tag{2.11}$$

where:

n = porosity
z_b = bed level
S_x = sediment transport in cross-shore direction
S_y = sediment transport in alongshore direction
x = cross-shore position
y = alongshore position
S_t = total sediment transport
S_b = bed load sediment transport
S_s = suspended sediment transport

2.5.1. Bed load transport

Bed load transport is the transport of sediment in a thin layer close to the bed. Particles are rolling or saltating over the bed. At higher shear stresses sheetflow occurs, where sediment is moving in multiple layers instead of in one single layer of rolling and jumping particles. The layer can be in the order of centimeters thick and is moving back and forth as one sheet on top of an otherwise immobile bed. Since the grain-grain interaction and grain-water interaction is important in sheet flow transport, it is considered a form of bed load transport (Bosboom & Stive, 2015).

Bed load transport starts when the critical shear stress is exceeded. The transport is assumed to respond instantaneous to the bed shear stress. This is because near the bed the turbulent eddies are small and gravity limits the upward motions (Bosboom & Stive, 2015).

The bed load transport can be written in a dimensionless form Φ_b (2.12). Many formulas for the bed-load transport exist. Most of them are a function of the shear stress on the grains and as such include a form of the Shields parameter θ (eq. 2.13). The influence of the waves is included into the Shields parameter by either using a wave-averaged bed shear stress or by using the instantaneous bed shear stress combined for waves and currents(Bosboom & Stive, 2015). The differences between the transport formulas can be up an order of magnitude. This highlights the importance of calibration (Bosboom & Stive, 2015).

$$\Phi_b = \frac{S_b(t)}{\sqrt{(s-1)gD_{50}^3}} \tag{2.12}$$

$$\Phi_b(t) = f(\theta'(t), \theta_{cr}) \tag{2.13}$$

where:

Φ_b = dimensionless bed load transport
θ' = instantaneous dimensionless shear stress
θ_{cr} = critical dimensionless shear stress parameter

2.5.2. Suspended sediment transport

Above the bed layer sediment is in suspension in the water column. Sediment particles do not immediately return to the bed, but are kept in suspension via turbulent motion. They are moving with the water particles at the same velocity.

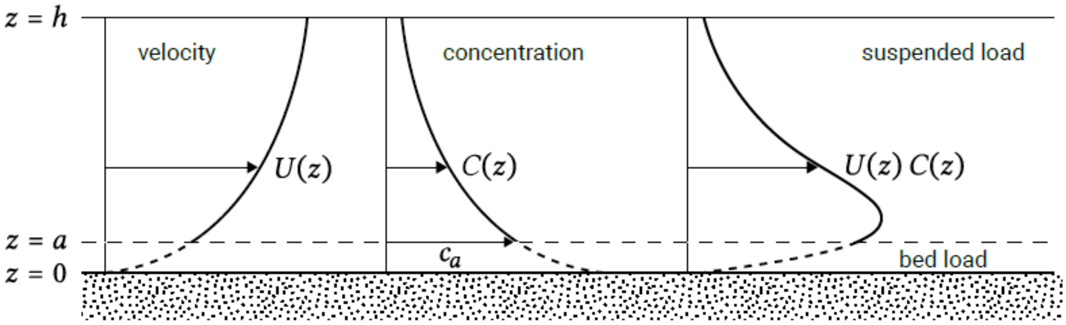

Figure 2.5: Examples of time averaged velocity U(z) and concentration C(z) varying over the water depth, with the resulting depth varying sediment flux U(z)C(z). The region between z = 0 and z = a is where bed-load transport takes place (Bosboom & Stive, 2015).

Therefore, the suspended sediment transport can be seen as the product of the sediment concentration c and the horizontal flow velocity u (eq. 2.15). Both the velocity and concentration are varying over the water depth (fig. 2.5). The vertical concentration profile can be obtained from the advection-diffusion equation for the concentration (eq. 2.14). The change in concentration over time is a balance between upward vertical transport caused by turbulent diffusion and the downward vertical transport under influence of the sediment fall velocity (Bosboom & Stive, 2015).

$$\frac{\partial c}{\partial t} - w_s \frac{\partial c}{\partial z} - \frac{\partial}{\partial z}\left(\nu_{t,s}\frac{\partial c}{\partial z}\right) \tag{2.14}$$

where:

c = concentration
w_s = fall velocity
$\nu_{t,s}$ = turbulent diffusivity

Solving the advection-diffusion equation for the concentration, results in the Rouse-profile (eq. 2.16). The solution is dependent on the concentration C_a at a reference bed level $z = a$, which is often determined from bed-load transport models. The largest concentration is found near the bed and is decreasing when moving up the water column. Therefore the flow near the bed will be governing for the direction of the suspended sediment transport.

The Rouse-profile gets its name from the exponent in the solution, the Rouse number. The Rouse number is a ratio between the downwards and upwards velocity of a sediment particle. For increasing grain size the settling velocity and thus the Rouse number will be larger. The effect is that more sediment will be concentrated near the bed (Bosboom & Stive, 2015).

$$\langle S_s \rangle \approx \int_a^h U(z)C(z)dz \tag{2.15}$$

$$\frac{C}{C_a} = \left[\frac{h-z}{z}\frac{a}{h-a}\right]^{\left(\frac{w_s}{\kappa u_*}\right)} \tag{2.16}$$

where:

$\langle S_s \rangle$ = time-averaged suspended sediment transport
u = horizontal flow velocity
U = time-averaged flow velocity
c = concentration
C = time-averaged concentration
a = near bed reference level
κ = Von Karman constant, 0.4
u_* = shear velocity
z = vertical position
h = water depth
C_a = concentration at a near bed reference level $z = a$

2.6. Cross-shore sediment transport

The cross-shore sediment transport is what determines the shape of the beach profile. To analyse the contribution of different processes to the cross-shore sediment transport the velocity signal can be split up in a mean flow, a low frequency oscillatory flow caused by long waves and a high frequency oscillatory flow caused by short waves (eq. 2.17). Considering the bed load to be proportional to $\langle u|u|^2 \rangle$ and using a Taylor expansion, three main contributors to the cross-shore sediment are found (eq. 2.18) (Bosboom & Stive, 2015).

$$u = \overline{u} + u_{low} + u_{high} \tag{2.17}$$

$$< u|u^2| >= 3 < \overline{u}|u_{high}|^2 > + < u_{high}|u_{high}|^2 > +3 < u_{low}|u_{high}|^2 > +... \tag{2.18}$$

where:

u = cross-shore velocity
$\overline{u}$ = mean cross-shore velocity
u_{low} = time varying flow on the wave group time scale
u_{high} = time varying flow on the short wave time scale

All three terms on the right hand side of equation 2.18 include the factor $|u_{high}|^2$. This represents that sediment is stirred from the bed by short wave action. The sediment is then transported by either mean currents, long waves or short waves (Bosboom & Stive, 2015). The combined effect of all the contributions will determine whether the cross-shore transport is offshore or onshore directed. This is highly dependent on the wave conditions. During high energetic wave conditions the offshore directed undertow is the dominant transport process, while during low energy conditions the sediment is transported back onshore and the wave skewness is the most important transport mechanism (Cohn et al., 2018). The cross-shore beach profile will recover after an erosion event, as long as the eroded sediment has remained in the system.

2.6.1. Mean current

The first term on the right hand side of equation 2.18 is related to the transport of sediment by the mean current. As the concentration of sediment is largest near the bed, the near bed flow direction is governing for the net sediment transport direction. Depending on the direction of the flow, the contribution of the mean current to the sediment transport can either be onshore or offshore directed depending on the direction of the flow.

Next to the horizontal wave motion an additional horizontal flow, called the Longuet Higgings streaming, is present in the shoaling zone. The streaming is found near the bed and contributes to onshore sediment transport. The mean streaming velocity is dependent on the free stream velocity $\hat{u}_0$ caused by the wave motion (eq. 2.19; Bosboom and Stive (2015)).

$$U_0 = \frac{3}{4}\frac{\hat{u}_0^2}{c} \tag{2.19}$$

where:

U_0 = mean Longuet Higgins streaming velocity
$\hat{u}_0$ = maximum free stream velocity
c = wave celerity

In the surfzone the velocity profile shows onshore directed flow near the surface and offshore directed flow near the bed (fig. 2.6). The breaking waves cause an onshore mass transport near the water surface called the Stokes's drift. As the coast is a closed boundary, this flow is compensated by an offshore directed undertow below the wave through level (fig. 2.6. The result of the mean velocities in the surfzone is an offshore directed sediment transport (Bosboom & Stive, 2015).

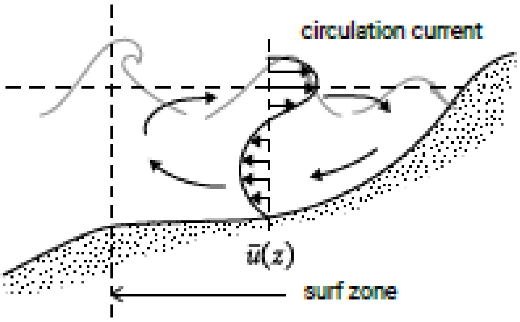

Figure 2.6: Depth varying velocity in the surf zone. The onshore Stokes' drift is compensated by the undertow (Bosboom & Stive, 2015).

2.6.2. Short waves

The second term on the right hand side of equation 2.18 is associated with transport caused by short wave skewness. A skewed wave has a asymmetric profile along the horizontal axis. If the wave is positively skewed, the crests are larger than the troughs and the time averaged cube of the surface elevation $\langle\eta^3\rangle > 0$ (Bosboom & Stive, 2015). For negatively skewed waves the situation is reversed.

In the shoaling zone waves gradually transform from a symmetric sinusoidal wave to a positively skewed wave with high narrow peaks and broad shallow troughs (fig. 2.7). The non-linear relationship between the bed shear stress and the velocity (eq. 2.20) results in significantly more sediment that is stirred from the bed under the velocity peaks. Therefore, more sediment is transported onshore under the wave peaks than transported offshore under the troughs, causing an net onshore sediment transport (Bosboom & Stive, 2015).

$$\tau_b = \rho c_f u^2 \tag{2.20}$$

where:

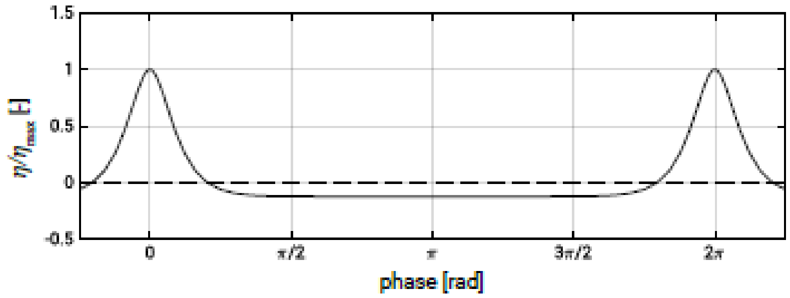

Figure 2.7: Example of a positively skewed wave (Bosboom & Stive, 2015)

τ_b = bed shear stress
c_f = friction coefficient

2.6.3. Long waves

The third term term on the right hand side of equation 2.18 signifies that sediment stirred by short wave action is transported by the long wave motion. Long waves have a frequency between 0.004 Hz and 0.04 Hz and are generated by the wave group motion (Bosboom & Stive, 2015).

Depending on the correlation between the long wave motion and the short wave variance of the wave group, the net sediment transport direction will be onshore or offshore directed. Outside the surf zone the long waves are bound to the wave group motion. They have the same wave length and period and travel at the wave group velocity c_g. The bound long waves are π out of phase, so the troughs of the long wave coincide with the highest and the crests with the lowest wave group energy. Hence, the largest sediment stirring occurs when the bound long wave velocity is offshore directed, contributing to net offshore transport (fig. 2.8). Inside the surf zone the long waves are released and the correlation between the long waves and the wave group energy can become positive, resulting in onshore directed transport (Bosboom & Stive, 2015).

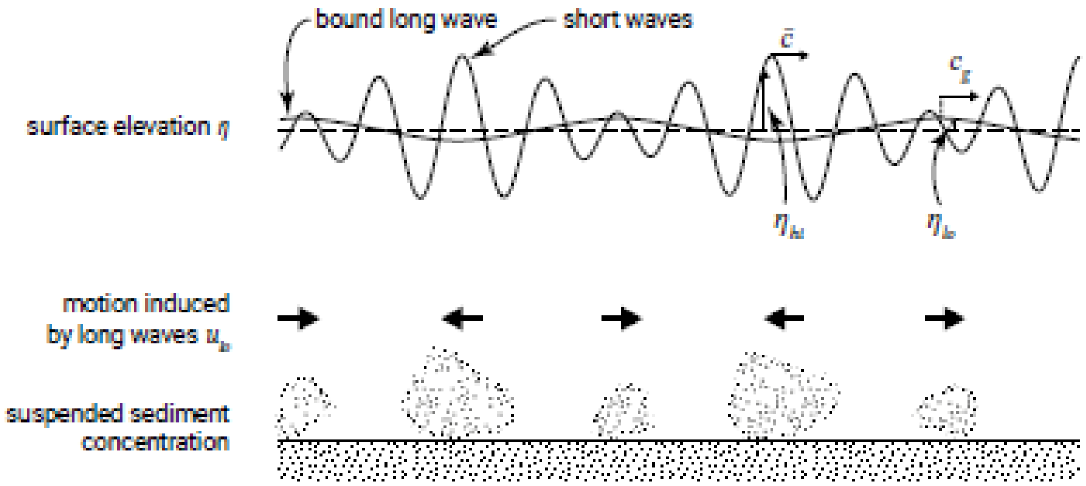

Figure 2.8: Suspended sediment transport under bound long waves. Sediment concentrations are largest when the bound long wave velocity is offshore directed, resulting in a net offshore transport (Bosboom & Stive, 2015)

Long waves become increasingly more important as the water depth decreases. As short waves break, wave energy is transferred from the short wave frequencies toward the long wave frequencies. In the inner surf zone on gently sloping beaches the long waves become dominant and have been found to stir up sediment as well (Bertin et al., 2018). In such a case, only considering the three terms of equation 2.18 related to $|u_{high}|^2$ will not be sufficient and terms including sediment stirring by long waves need to be included as well.

2.7. Swash zone transport

Swash is the variation of the waterline over a single wave. It is a cyclic process that starts with a bore moving onshore, while there is a strong offshore directed current near the bed (fig. 2.9a). When the bore collapses the flow up the beach is accelerated(fig. 2.9b). As the maximum uprush is being reached, water already starts to move offshore as backwash in the lower surf zone (fig. 2.9c). During backwash the flow is accelerated offshore due to gravity and is decelerated as it collides with the next bore (fig. 2.9d; Masselink and Puleo (2006)).

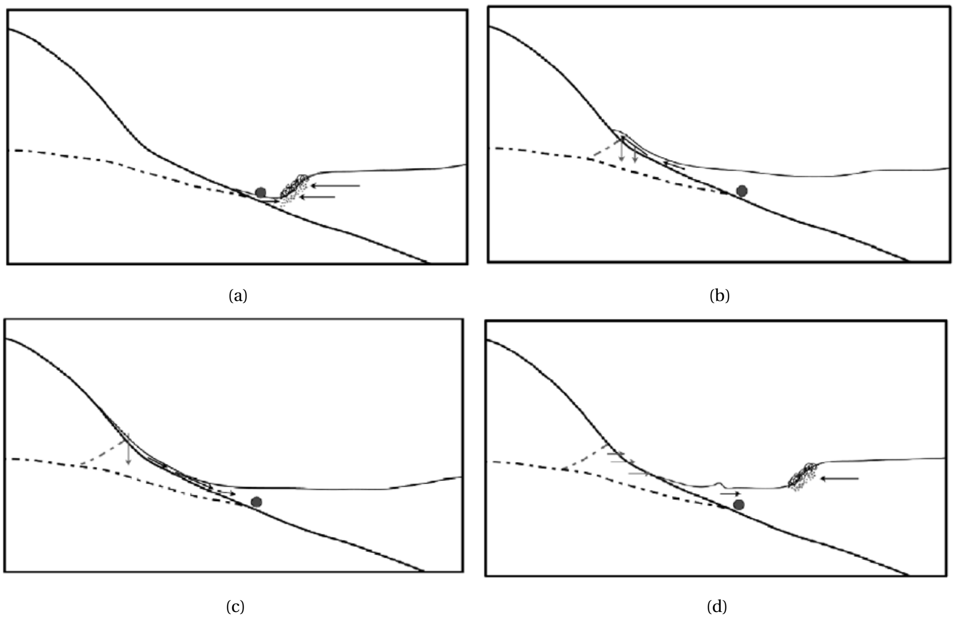

(a) (b) (c) (d)

Figure 2.9: The cyclic motion in the swash zone. a) the bore approaches. b) the bore collapses and flow accelerates onshore. c) the maximum uprush. backwash starts in lower swash zone. d) offshore flow is decelerated by next incoming bore (Masselink & Puleo, 2006)

The swash zone is a highly turbulent region. Turbulence is highest at the start of the uprush. As the bore collapses, turbulence moves toward the bore front and is injected into the water column suspending sediment from the bed. The turbulence then rapidly decreases allowing the sediment to settle and consequently the water is clear at flow reversal. During backwash the turbulence is mainly generated at the bed. The sediment transport will be predominantly sheet flow, although at the end of the backwash the offshore flow has accelerated enough to suspend sediment (Masselink & Puleo, 2006).

The duration of the uprush is shorter than the backwash, while the flow velocities are of the same magnitude. This would imply that more sediment would be transported offshore than onshore. It that were the case, the swash zone would be continuously eroding. Masselink and Puleo (2006) discerned the following four counterbalancing processes that contribute to onshore sediment transport. First, in- and exfiltration of water into the beach affects the boundary layer shear stress and the vertical pressure on the grains. For coarser grains this assists onshore sediment transport. Second, the very turbulent bore collapse and the flow accelerations when changing from backwash to uprush increase the bed shear stresses during the uprush, suspending more sediment and transporting it onshore. Third, the sediment entrained in the surf zone can be advected to the swash zone and add to the onshore transport. Last, the settling and scour lag can result in fine particles being deposited high in the swash zone, that can't be picked up by the smaller backwash velocities.

2.8. Breaking induced turbulence

Turbulence has a crucial influence on sediment transport. It increases the shear stress acting on the grains, setting sediment particles in motion. Also, it aids in keeping sediment particles suspended in the water column. Wave induced turbulence is caused by two distinct processes: the wave orbital motion generates shear stress near the bed and breaking waves convert wave energy to turbulent kinetic energy at the surface (Christensen et al., 2018). Breaking induced turbulence is the largest contributor the turbulence in the surf-zone (Boers, 2005). The type of breaker affects the way turbulence is generated and reaches the bed. In this section first the breaker types will be discussed followed by the effect of the breaker type on the turbulence and sediment transport.

2.8.1. Breaker types

The breaker type is determined by the relative steepness of the beach slope in relation to the wave skewness. The Irribarren number can be used to predict the breaker type (eq. 2.21; Bosboom and Stive(2015)).

$$\xi = \frac{tan(\beta)}{\sqrt{H/L_0}} \tag{2.21}$$

where:

ξ = Irribarren number
β = bed slope
H = wave height
L_0 = deep water wave length

First, an Irribarren number of $\xi < 0.5$ corresponds to spilling breakers. Spilling breakers are present on a shallow slope, with a large breaker zone. There is nearly no reflection of energy as almost all energy is dissipated. Second, plunging breakers occur for values of ξ between 0.5 and 3.3. They have a curling crest that breaks on top the lower part of the wave. The plunger introduces a lot of turbulence and exerts a large force on impact. Third, surging breakers correspond to a value of $\xi > 5$. Surging waves surge up and down very steep beaches with a narrow breaker zone. They don't really break but are reflected back into the sea, creating a standing wave pattern. Last, the collapsing breakers are an intermediate type between the surging and plunging breakers (Bosboom & Stive, 2015).

2.8.2. Effect of breaker type on turbulence and sediment transport

When waves break in the surf zone, wave energy is converted to turbulent kinetic energy. The type of breaker affects the way that turbulence is generated and injected into the water column. Plunging breakers have large plunger vortices that directly transport turbulence towards the bed and increase the bed shear stress. The turbulence is highest under the wave front and decreases rapidly after the wave crest has past, resulting in large fluctuations in turbulent intensity between breakers (Ting & Kirby, 1995; Christensen et al., 2018). Spilling breakers, on the other hand, are much more diffusive in nature. Turbulent motion is generated in the surface roller. Turbulent kinetic energy is dissipated inside the roller but also slowly diffuses into the water column below (Boers, 2005). Because of the slower, diffusive mixing the turbulent intensity decreases slowly towards the bed. The turbulence will reach the bed on the back of the wave and the variation over a wave period is much smaller than for plunging breakers (Ting & Kirby, 1996; Christensen et al., 2018).

Onshore suspended sediment transport is easier for plunging breakers than spilling breakers. Plunging vortices reach the bed at the front of the wave and are able to stir up larger amounts of sediment than the diffusive turbulence of spilling breakers. Thus, a larger sediment concentration coincides with the positive onshore velocities (Christensen et al., 2019).

2.9. Aeolian transport

Aeolian transport is the transport of particles by the wind. For wind-driven transport saltation is the dominant type of particle movement. Formulations for the aeolian transport are dependent on whether enough sediment is available to reach the transport capacity or the sediment supply is limited.

2.9.1. Transport capacity

When sediment is sufficiently available the the sediment transport capacity will determine the magnitude of sediment transport. The most known formulation has been derived by Bagnold (fig. 2.22 ; Bagnold (1941)).

The transport capacity is proportional to the cube of the wind shear velocity u_*. The coefficient C is an empirical constant that includes the effect of sediment sorting. Typical values are 1.5 for nearly uniform sand, 1.8 for naturally graded sand found in the dunes and 2.8 for very poorly sorted sand (Bagnold, 1941).

In order to use the wind velocity in stead of the shear velocity, equation 2.22 can be rearranged using a conversion factor α and a critical wind velocity u_c (Bagnold, 1941). The critical wind velocity is dependent on the grain size. For dry, loose sand the relation between the critical wind velocity and the grain size is shown in figure 2.10 (Van Rijn, 2019).

$$q = C\frac{\rho_{air}}{g}\sqrt{\frac{d}{D}}u_*^3 \tag{2.22}$$

$$q = \alpha C\frac{\rho_{air}}{g}\sqrt{\frac{d}{D}}(u-u_c)^3 \tag{2.23}$$

where,

q = aeolian sediment transport capacity
= empirical sediment sorting coefficient
ρ_{air} = air density
d = grain diameter
D = reference grain diameter, 0.25 mm
u_* = shear velocity
u = wind velocity
u_c = critical wind velocity

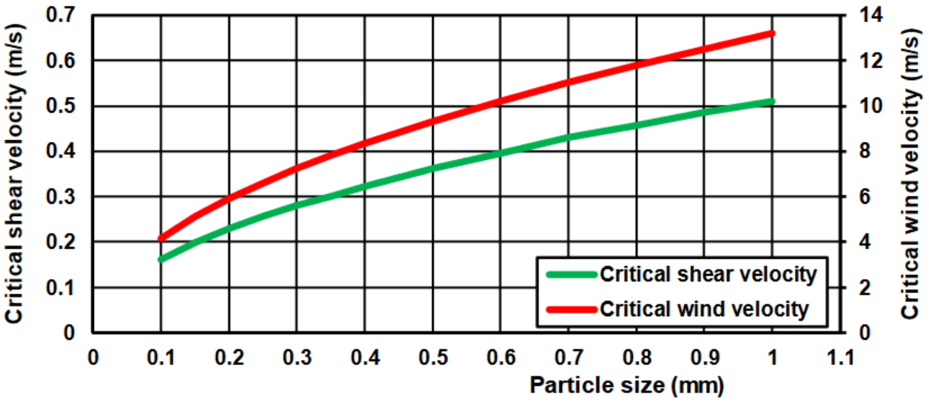

Figure 2.10: Threshold shear and wind velocity for dry, loose sand (Van Rijn, 2019).

2.9.2. Supply limited transport

The Bagnold type equations have generally led to an overprediction of the aeolian sediment transports, as on most beaches the transport rates do not reach the transport capacity. In that scenario the aeolian transport is said to be supply limited. A linear relation between the aeolian sediment transport and the wind velocity is proposed by De Vries et al. (2012):

$$Q_s = C_s \times U_s \tag{2.24}$$

where:

Q_s = total aeolian sediment transport
C_s = sediment concentration
U_s = sediment velocity

Factors limiting the aeolian sediment supply are critical fetch, sorting effects, moisture content cementation and vegetation. The first three are more important when considering the intertidal zone and will be discussed below.

Critical fetch

The critical fetch is defined as the length required for the aeolian transport to become saturated. If the supply is limited, saturated transport will take longer to develop. Therefore, there is a inverse relation between the critical fetch and the sediment supply (Hoonhout & de Vries, 2017). For uniform dry sand the critical fetch is a couple of meters, but in field studies the critical fetch was found to be in the order of tens of meters (Davidson-Arnott, MacQuarrie, & Aagaard, 2005). The tide becomes an important factor on supply limited beaches (Sarre, 1989). The falling tide increases the width of the beach and hence the available fetch. Therefore, larger transport rates can be achieved during low tide. The increase in fetch is dependent on the tidal range, beach slope and the wind direction.

Sorting effects and armoring

Different grain sizes have different threshold velocities. Under a steady wind velocity only particles up to a certain grain diameter will be picked up and transported downwind. What remains is a top layer of larger and heavier particles protecting the finer particles in the layers below. (McKenna Neuman, Li, & Nash, 2012). The remaining coarser grains create an armor layer that reduce the amount of sediment available for transport. Small shells, pebbles and little rocks contribute to the formation of an armor layer as well (Hoonhout & de Vries, 2017). Armoring on the upper beach has been the main reason why the intertidal zone is seen as an important source of sediment on supply limited beaches (Hoonhout & de Vries, 2017).

Moisture content

The tide induces variations in moisture content in the intertidal zone in time and space. When the intertidal zone is submerged, the beach will be fully saturated and after the beach is exposed the moisture content diminishes due to exfiltration and evaporation of water. Surface moisture increases the resistance of grains to aeolian transport. Adhesive forces between the water and the grain keep the grains together making it more difficult to entrain sediment. Further, a sediment particle that is in saltation, will be more likely to reattach to the bed of a wet surface (Wiggs et al., 2004).

Higher moisture content will increase the critical wind velocity. However, above the critical moisture theshold of 4-6% that was found on the beach, sediment entrainment is difficult and the aeolian transport is suppressed (Wiggs et al., 2004). The variations in moisture content on the beach cause large variations in the critical wind velocity, ranging from 5 to 9 m/s on a sandy beach with grains of $260\mu m$ (Davidson-Arnott (2007), as cited in Van Rijn (2019)).

3

Scanex field experiment

The Scanex campaign was a collaboration between multiple researchers from the civil engineering faculty of the TU Delft. Their combined measurements on the beach are a valuable resource for investigating the processes on the beach, and in this case in particular in the intertidal zone. The experiment took place from February 20202 until April 2020 at Noordwijk (fig. 3.1). In order to model the grain size distribution the Scanex fieldwork data has been used as input for the wave and tidal conditions, bed composition and bathymetry. Furthermore, it provided control data to compare the model result to. This chapter describes the Scanex fieldwork experiment and data collection (section 3.1), data processing methods (section 3.2 and data processing results (section 3.3). At the end of the chapter the Scanex data will be used to select a model scenario (section 3.4).

Figure 3.1: The ScanEx fieldwork location (GoogleEarth, n.d.).

3.1. Experiment site

Noordwijk is a small town situated on the Dutch central coast (fig. 3.1). The beach at Noordwijk is a dissipative, sandy beach with an average grain size of 300 micrometer (De Vries et al., 2015). It has a microtidal regime with a tidal range of 1.8 m and a sea wave climate (De Vries et al., 2015). The intertidal zone is characterized by an intertidal bar and runnel. Further offshore one or two subtidal bars are present. Several beach clubs are situated on the upper beach. Sand that has accumulated behind these clubs, is removed by bulldozers and redistributed on the beach.

A schematized view of the set up is shown in figure 3.3. A measurement pole was placed in the nearshore right in front of the Breakers Beach Club. On this pole a Nortek Vector Acoustic Doppler Velocimeter (ADV) and a Nortek pressure sensor were installed (fig. 3.4a) to measure the flow velocities and pressures caused by the tidal, wave and wind forcing . Soil samples were taken from the intertidal zone using a sandscraper (fig. 3.4b). The bathymetry of the beach was measured with a terrestrial laser scanner (TLS) located on top of a hotel at the beach front (fig. 3.4c). A weather station and video camera were placed next to it. Additional wind and meteorological data could be obtained from the WindGuru station that was already in place at local sailing club. An overview of the data that is available is shown in table 3.1.

Table 3.1: Overview of available data collected at Noordwijk, mainly during ScanEx

At beach club breakers		
Pressure sensor	5/10 Hz	Placed nearshore
ADV	2 Hz	Placed nearshore
Laser scanner	Every 30 min.	More detailed than regular scan
Soil samples	Biweekly	Surface sample
	5 February	Vertical samples
Moisture content	Biweekly	Can be obtained from soil samples
Full beach		
Laser scanner	Hourly	Ongoing after ScanEx
Camera images	Every 5 min.	
	Once a month few days at 5 Hz	
Wind data	Until 25 March	From WindGuru station at Sail Club
Weather station		Installed near laser scanner
Moisture content samples	During 5 days at low tide	For a 70m x 70m area
		Good correspondence with moisture from soil samples
Around container		
Laser scan	Several single scans	Around container

Figure 3.2: The sea at Noordwijk beach (photo taken by Scanex fieldwork camera).

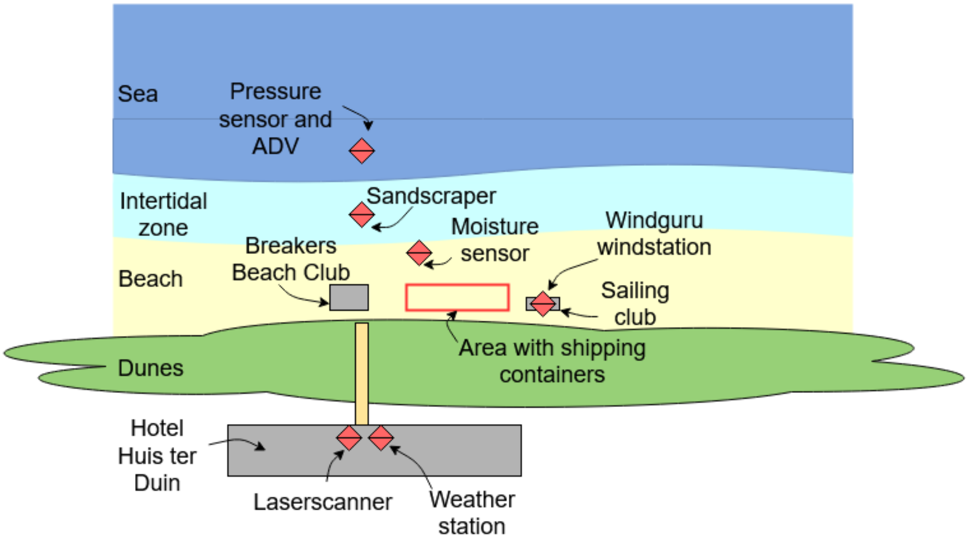

Figure 3.3: Overview of the ScanEx data collection setup

(a) The Nortek ADV and pressure sensor directly after set up during low water

(b) The sandcraper set up. The metal pins around the sampler control how far the sampler is pushed into the ground.

(c) The set up of the Permanent Laser Scanner on the topmost balcony at Hotel Huis ter Duin in Noordwijk. Next to the laser scanner the weather station is placed.

Figure 3.4: Instrument set up during ScanEx

3.2. Data processing methods

The data of the Scanex fieldwork is used as input for the XBeach model and as a control for the model result. The pressure sensor is used to check the ADV-data and to provide a general idea of the wave conditions. The XBeach model requires the incoming wave and tidal conditions which are retrieved from the ADV-data. For the initial bed composition a transect of soil samples were used to compute the averaged grain size distribution on the beach. The initial bathymetry of the model is based on a cross-shore transect of the laser scan point cloud. The Windguru Windstation data is processed, so it can be used next to the wave data when determining the model scenario. The methods to derive wave, flow, tidal and wind conditions from raw pressure and velocity data, grain size distributions, the 1D cross-shore profiles from the laser scanner and the wind station are discussed below.

3.2.1. Pressure sensor

The raw pressure signal obtained directly from the pressure sensor shows a sudden jump of 0.11 bar on the 9th of April (fig. 3.5a). This event coincides with the deployment of a new pressure sensor. As the jump cannot be explained by natural variations it is likely caused by a different offset of the pressure sensors that has been removed creating a continuous pressure time series (fig. 3.5b).

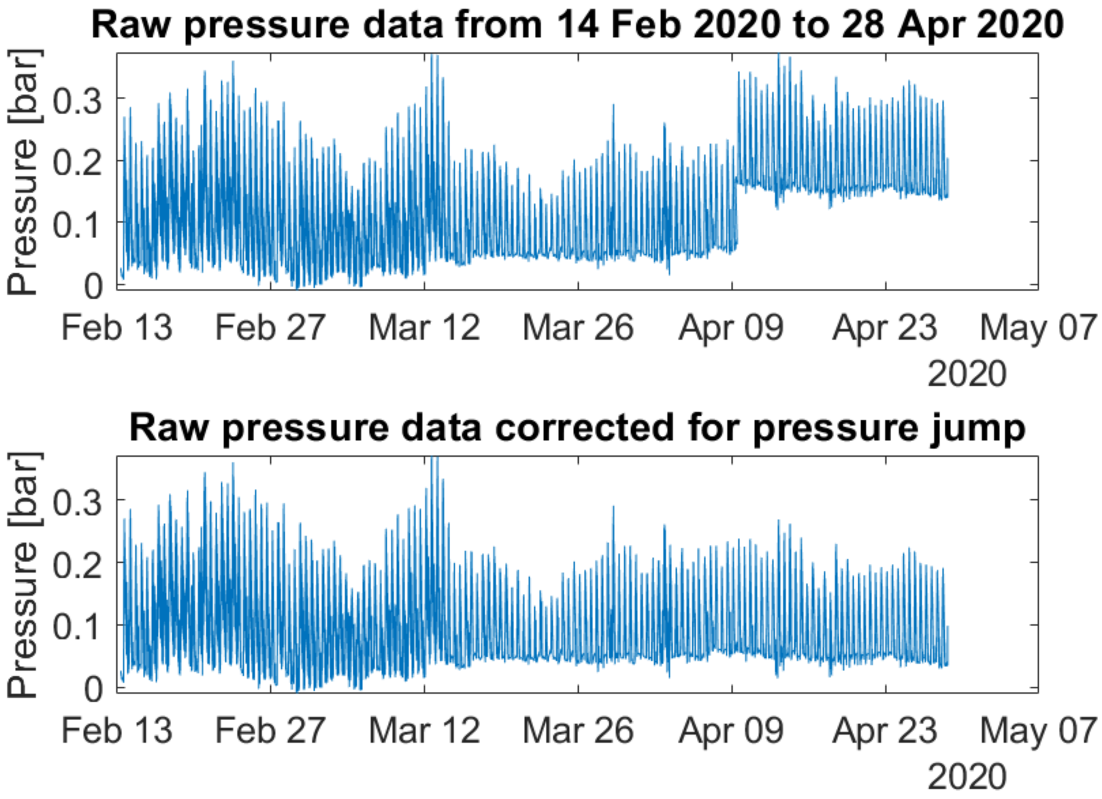

Figure 3.5: Raw pressure sensor data a) before offset correction and b) after offset correction

To obtain the wave height the raw pressure signal is converted to a surface elevation. If hydrostatic pressure is assumed, this is done by dividing the pressure signal p (in N/m^2) by the salt water density $\rho = 1025 kg/m^3$ and the gravitational constant $g = 9.81 m/s^2$.

In reality the pressure measured at the sensor is a combination of both hydrostatic and dynamic wave pressures (fig. 3.6). The total pressure for a regular wave can be computed with equation 3.1 (Holthuijsen, 2007). Both the figure and the equation assume a positive z-axis upward, with $z = 0$ at the mean water level and the bed level at $z = -d$. The wave amplitude is a, the wave number k, the wave frequency ω and position x.

$$p = -\rho g z + \rho g a \frac{cosh[k(d+z)]}{cosh(kd)} sin(\omega t - kx) \tag{3.1}$$

$$K = \frac{cosh(kd)}{cosh[k(d+z)]} \tag{3.2}$$

where:

p = pressure
ρ = salt water density
z = vertical position
a = wave amplitude
k = wave number, $\frac{2\pi}{L}$
d = water depth
ω = wave frequency, $\frac{2\pi}{T}$
t = time
x = horizontal position
K = dynamic wave pressure correction factor

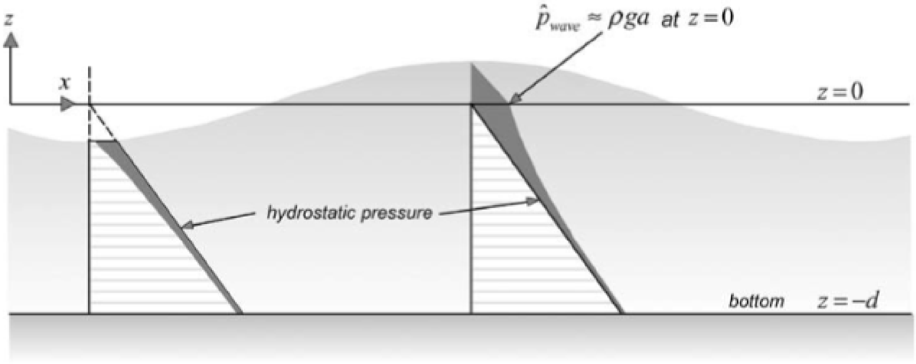

Figure 3.6: Combined wave-induced and hydrostatic pressure over the vertical (Holthuijsen, 2007).

To correct for the presence of the dynamic pressure the time series are divided into 30 minute segments. This length has been chosen such that the segment is short enough to be considered stationary and long enough to maintain the detail in the time series (Holthuijsen, 2007). The segments are detrended and a Fast Fourier Transformation (FFT) is used to convert them into an amplitude spectrum with a frequency dependent amplitude a. Next, for each frequency the wave number is obtained from the linear dispersion relation resulting in a frequency dependent correction factor K (eq. 3.2) that is applied to the spectral amplitudes. Finally, the corrected spectral amplitudes are converted back into a time series of the surface elevation using an inverse FFT.

The pressure correction is shown in figure 3.7a together with the uncorrected surface elevation assuming hydrostatic pressures only for the complete measuring period. Figure 3.7b zooms in on the signal to show the correction of individual waves. Due to the correction the troughs are lower and the crests higher than initially computed with the hydrostatic pressure assumption.

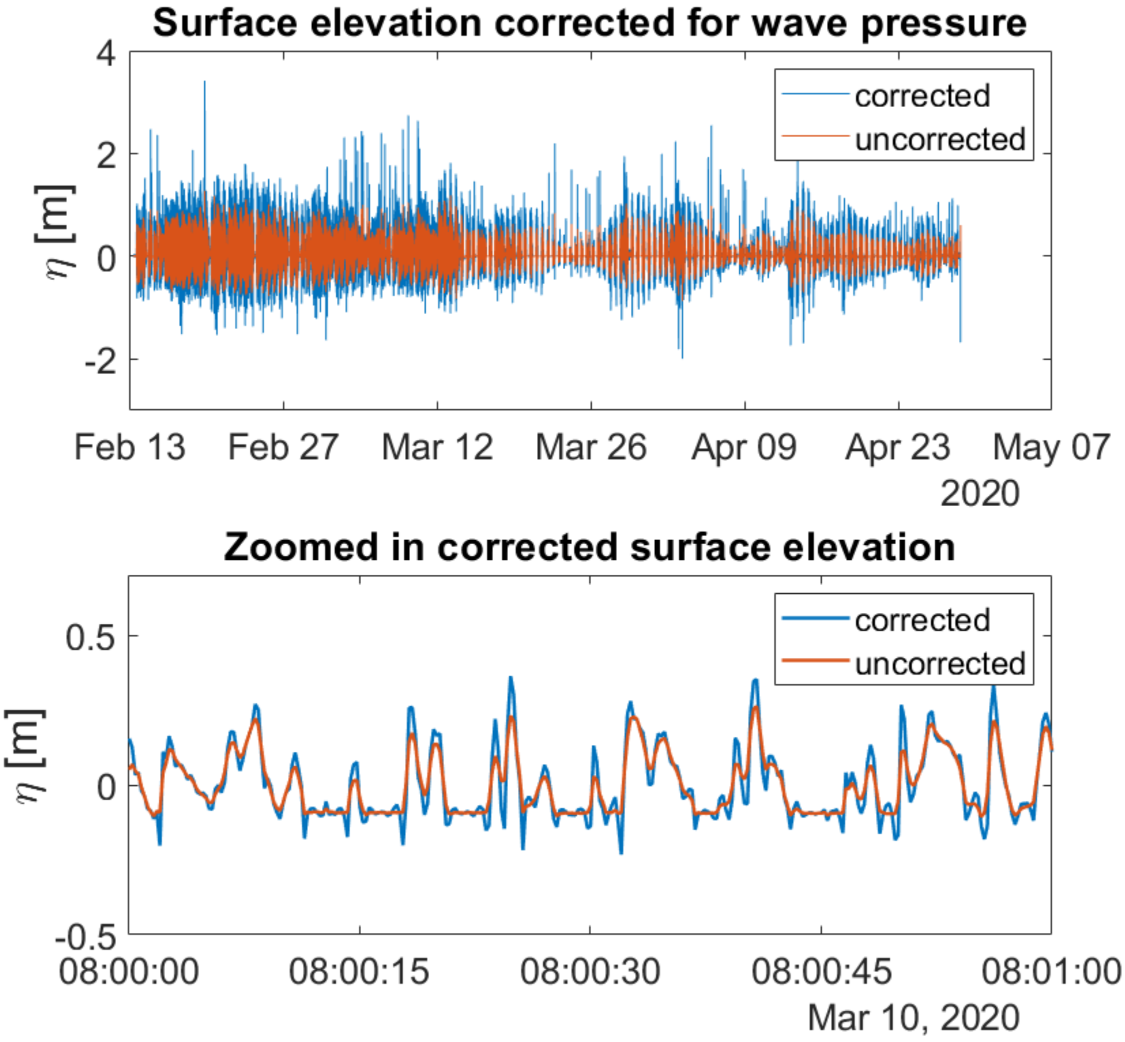

Figure 3.7: The surface elevation assuming hydrostatic pressure (orange) and the surface elevation that is corrected for the wave pressure (blue) for a) the full measuring period from 14 Feb to 28 April and b) zoomed in on a 2 minute period to visualize the individual waves.

3.2.2. ADV

The X-Beach model requires the incoming wave and tidal conditions at the offshore boundary. This subsection describes how these inputs have been computed with the Guza method (Guza et al., 1985) from the processed cross-shore velocity u and the pressure p obtained with the ADV.

The Acoustic Doppler Velocimeter or ADV is an instrument that uses ultrasound to determine the 3D-velocity vector. It emits ultrasound waves that are scattered by particles in the flow. The reflected signal is picked up again by the receivers. The flowing water causes a Doppler shift in the frequency of the ultrasound waves, which is proportional to the flow velocity. The Nortek Vector ADV has three receivers positioned in such a way that it is possible to construct a 3D-velocity vector (Nortek, 2018).

The Nortek Vector ADV also includes a built in pressure sensor. For the wave analysis this pressure signal is used instead of the signal from the separately installed pressure sensor discussed in the previous subsection, because the time stamp of the pressure needs to match the time stamp of the velocity measurements to enable the separation between incoming and outgoing waves (Guza et al., 1985).

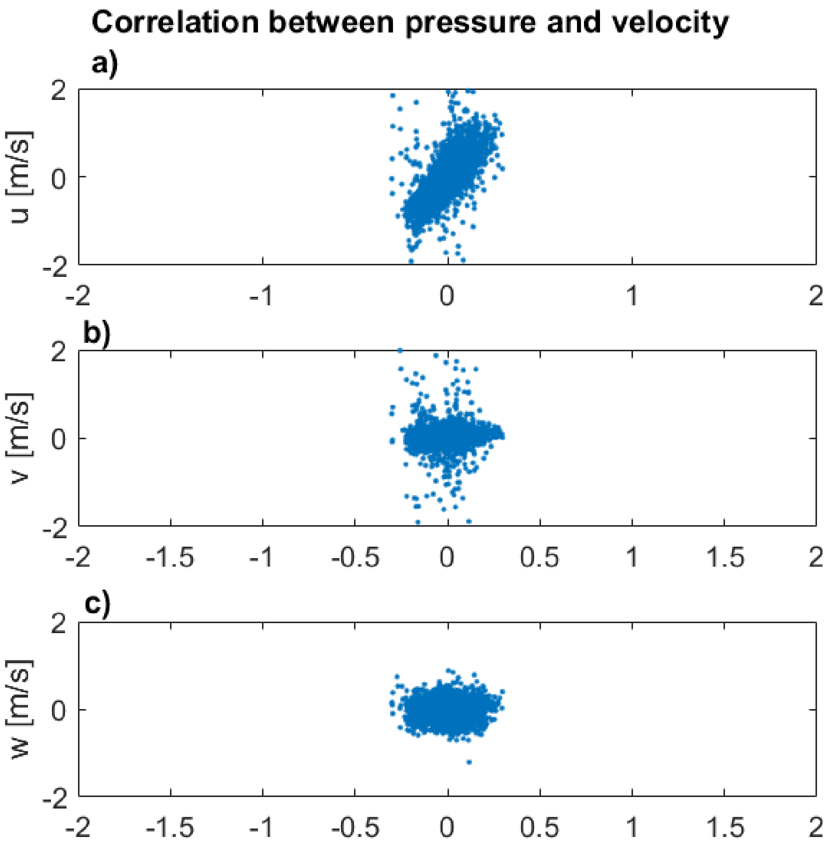

Figure 3.8: Correlation between detrended pressure and the velocity components: a) positive correlation between cross-shore velocity u and the pressure, b) no correlation between alongshore velocity v and the pressure, c) smaller velocity variations and signals that are out of phase corresponding to vertical velocity z

The ADV at Noordwijk was in place from the 24th of February till the 29th of April. It operated in continuous mode at a frequency of 2 Hz. The measurements were stopped twice during ScanEx, resulting in three sensor output files. The sensor output files were converted from a binary file into different data structures of which two were used: a .hdr file containing the sensor settings and output formats of the other data structures and a .dat file, in which the velocity and pressure measurements are stored, together with reliability indicators (Nortek, 2018). The distance from the ADV to the bed was measured two times during the measurement period. An average distance to the bed of 0.3 m was found and used for computing the incoming and outgoing waves.

Orientation of the sensor

The cross-shore velocity u at the beach is needed to compute the wave input for the model, but the velocity data is described with three components in the XYZ-direction local to the ADV-sensor. These local velocities need to be related to the cross-shore horizontal velocity u, the alongshore horizontal velocity v and the vertical velocity w at the beach. Since the ADV has been carefully installed in line with the used coordinate system at the beach, the ADV velocity components do not need to be rotated and can be used directly. This is confirmed by examining the correlation between the pressure and the velocity discussed next (fig. 3.8).

Linear wave theory shows that the pressure of the horizontal orbital velocity is in phase with the pressure, while the vertical orbital velocity is 90^o out of phase (Holthuijsen, 2007). It also shows that in shallow water the near bed vertical velocity decreases to zero, while a much larger horizontal streaming velocity is present. When applying this to figure 3.8 the vertical velocity w was found because it is much smaller than the other components. For waves coming in at an angle from the shore normal, both horizontal velocity components will have a contribution from the horizontal orbital velocity. Due to refraction towards the shore normal, the contribution to the cross-shore velocity is much larger. Thus, it was possible to distinguish the two horizontal velocity components from each other. The cross-shore velocity u shows a clear positive correlation between the pressure and the velocity. For the alongshore velocity v the positive correlation is not as apparent, as the signal contains more noise compared to the smaller velocities.

If the cross-shore velocity u would have shown a perfect correlation, all the points in the figure would lie on a single line. Deviations from this line are related to instrument noise, directional spreading of the waves and reflections from the beach.

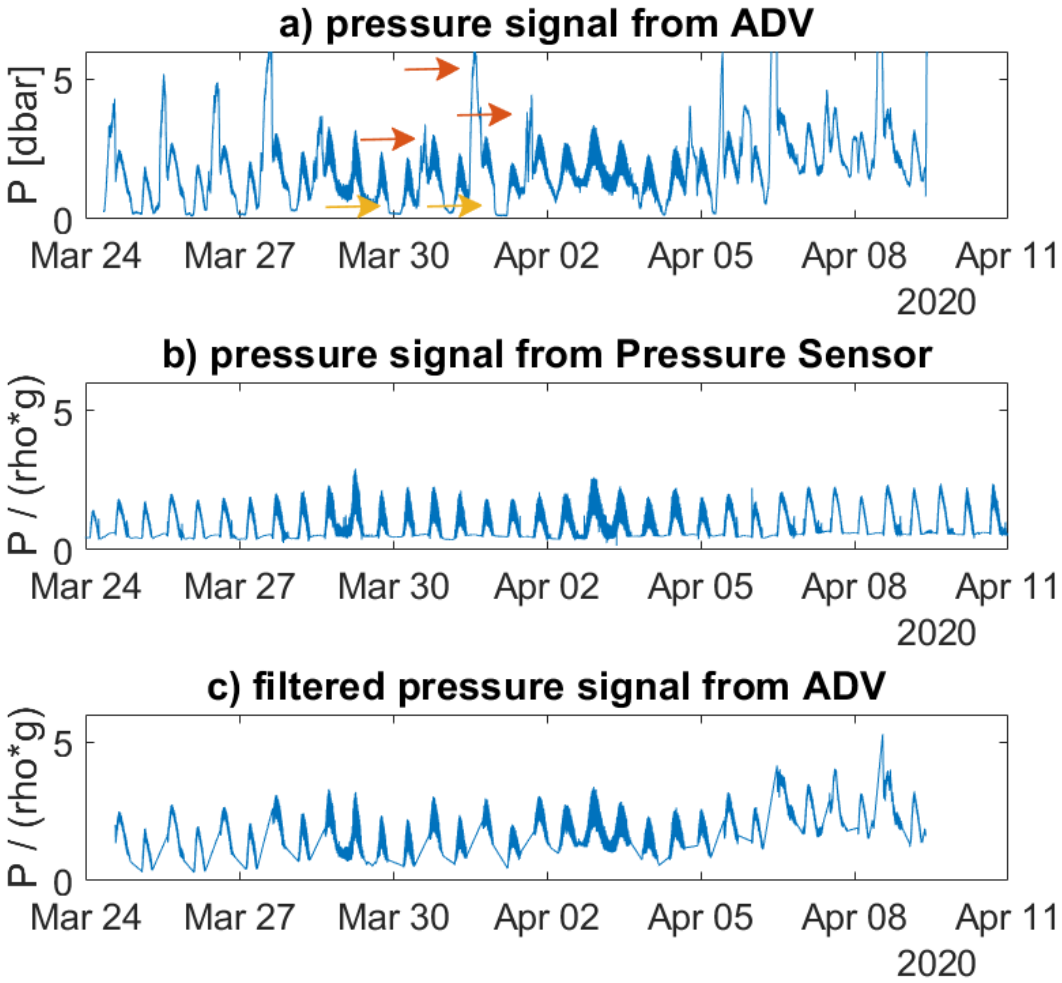

Figure 3.9: Comparison between pressure sensor and the the pressure signal from the ADV. a) The pressure signal from the ADV has segments with low readings (yellow arrows) and segments with unexpected spikes (red arrows). b) The pressure signal from the pressure sensor, showing that the unrealistic spikes coincide with the low readings of the emerged sensor c) the filtered pressure signal from the ADV, where the low readings and the spikes have been removed

Quality check

After establishing the orientation of the ADV sensor, the reliability of the measurements was checked. First, it was found that at the end of the data files the recording was not continuous anymore and multiple bursts of measurements were present with unreliable frequencies. For these bursts it is not possible to establish the correct time stamp, so they were removed from the dataset. This has had a significant influence on the available data. During the Scanex fieldwork the ADV stopped measuring with a continuous frequency on 15-3-2020, six days before it was taken out of the water for a check up. The ADV was reinstalled on 24-3-2021, which means that in the intermediate period ADV data was missing.

Second, the measurements were checked on their Signal to Noise Ratio (SNR) and the correlation. The SNR is a measure of strength of signal that is returned to the ADV and should be higher than 15. For a single measurement two similar signals are emitted by the ADV and their echoes are returned. A high correlation between these echoes increases the probability that the ADV has picked up the right signals (Nortek, 2018). A minimum value of 60% was used for the correlation. The SNR is given for the x-, y- and z-directions and the correlation for the three receivers, resulting in six requirements in total. Data points that did not meet all the requirements were removed. In the three data sets 32.6%, 56.8% and 60.0% of the points were removed after filtering for SNR and correlation.

Lastly, some unrealistically large spikes remained in the cross-shore velocity. This could be caused by vibrations in the pole the ADV was mounted on (Nortek, 2018). To remove the spikes a velocity threshold was set to $u < 2.0$ m/s or $u > -2.0$ m/s. Velocities that were not within this range, were removed. The gaps were filled by linear interpolation between the neighbours that were not part of the velocity spike.

After filtering the remaining points were compared to the signal of the separate pressure sensor to see if the loss of points was acceptable (fig. 3.9). The unfiltered pressure signal from the ADV in figure 3.9a shows segments of very low, constant pressure (yellow arrows) but also segments with unexpected spikes (red arrows). When comparing this signal from the ADV to the signal of the pressure sensor (fig. 3.9b) it can be seen that both types of segments occur during low water and are most likely caused by the sensor being above water. During these times no waves can be registered by the ADV. In the filtered pressure signal (bottom image) it can be seen that mainly these low water segments are filtered out. Once the sensor is underwater the amount of reliable measurements is sufficient to use for the wave input.

Incoming waves and mean water level

The correlation between the cross-shore velocity and the water pressure suggests that partial reflection could play a role at the beach (fig. 3.8a). This means that the waves measured at the ADV-sensor can be seen as a superposition of waves that are coming in and waves that have been reflected at the shoreline and are going out. The Guza-method has been used in the following to separate the incoming and outgoing waves (Guza et al., 1985). Is is based on the linear shallow water equations and assumes hydrostatic pressure and a horizontal bed. With the cross-shore velocity u and the surface elevation η the incoming and outgoing waves can be determined using expressions 3.3 and 3.4 respectively.

$$\eta_{in} = \frac{1}{2}\left(\eta + u\sqrt{\frac{h}{g}}\right) \tag{3.3}$$

$$\eta_{out} = \frac{1}{2}\left(\eta - u\sqrt{\frac{h}{g}}\right) \tag{3.4}$$

Next to the waves, the 30-minute averaged mean water level was computed with respect to MSL. This mean was set to the center of the 30-minute interval and linear interpolation was applied to obtain the mean water level for every point of the time series. Fewer than 50 available measurements per 30-minute interval were found to correspond to a low tide during which the ADV stood dry. In such a case the incoming and outgoing wave signals were set to zero and the mean water level was set to the distance of the sensor to MSL, which was -0.3 m.

3.2.3. Soil samples

Information on the bed composition was gathered by taking soil samples with a sandscraper (fig. 3.4b) during low tide along a cross-shore transect (fig. 3.10). The sandscraper removes soil samples layer by layer where the thickness of each removed layer can be adjusted. In this way a top layer of 2 mm thickness only was sampled, representative of the active layer of the combined aeolian and hydraulic sediment transport.

The top-layer samples were dried in an oven and put through a sieve tower. The tower consists of nine sieves stacked on top of each other and one pan at the bottom that collects the smallest grains that fall through

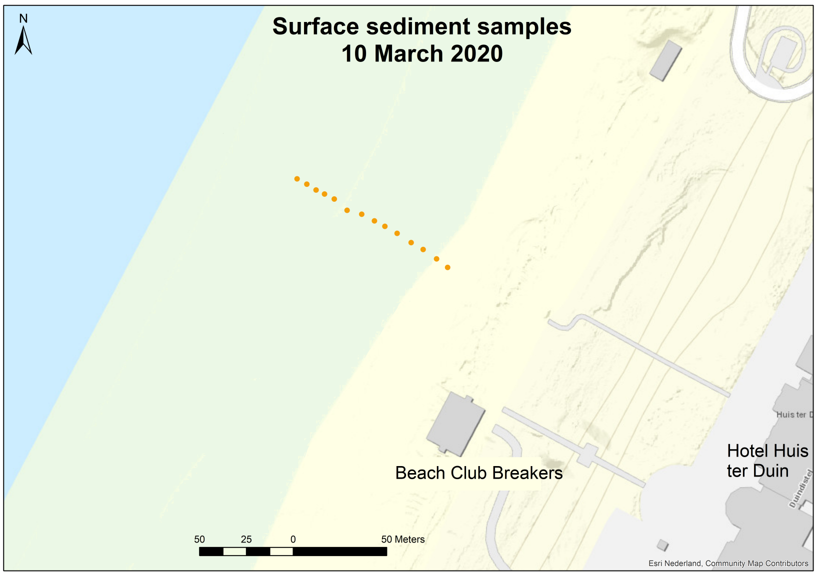

Figure 3.10: The soil sampling locations on the cross shore transect on 10-03-2020. The orange dots represent the sampling locations. (based on: Christa van IJzendoorn, 2020, not published)

all the sieves. This corresponds to ten sediment classes j. With the sieve tower the fraction p_j of each sediment class to the total soil sample can thus be measured. This yields a grain size distribution curve showing the sieve diameter versus the percentage of sediment passing. The nominal grain size D_{50} is subsequently computed as a weighted average of the grain size using the sediment fractions p_j as the weights and and a characteristic diameter d_j for each sediment class according to:

$$D_{50} = \sum_{j=1}^{10} p_j * d_j \tag{3.5}$$

where:

D_{50} = median grain diameter
p_j = sediment ffraction of the jth sediment class
d_j = characteristic diameter of the jth sediment class

For the top sieve and the bottom collection pan the characteristic diameter is estimated based on visual inspection of the soil found in there. The other sieves used the mean value of the diameter range.

The initial grain size distribution for the XBeach model is computed as the averaged sediment grain size distribution of 14 soil samples taken along the transect on the 10-3-2020. The mass contributions of each sediment class were summed over the fourteen soil samples and the fractions to the total mass were computed.

3.2.4. Terrestrial laser scanner

The 1D cross-shore profiles have been derived from the laser scanner with Cloud Compare and Matlab. They have been used for the in initial profile in X-Beach and to evaluate how well the morphological changes are modelled.

A laser scanner is an active remote sensing technology that uses infrared light to map the surroundings. Based on the time it takes for the signal to be reflected and returned to the scanner the distance to a point can be calculated. Combined with the location and position of the laser scanner, a point cloud with 3D coordinates is created from the surroundings. (Vos et al., 2017). Reference points with known GPS locations are used to transform the point cloud from its local reference system to a georeferenced system.

The terrestrial laser scanner (TLS) is stationed at Noordwijk for a period of two years as part of the CoastScan project. CoastScan aims to monitor coastline changes on multiple spatio-temporal scales and to increase the understanding of coastal topography changes (Vos et al., 2017). For this the TLS makes hourly scans of the beach at Noordwijk. During Scanex additional scans of the intertidal zone were taken every 30 minutes at an increased spatial resolution.

To obtain the intertidal bathymetry Scanex laser scans taken during low tide have been used. These scans were already georeferenced and therefore ready for further processing in Cloud Compare and Matlab where the steps discussed below have been outlined in a flow chart (fig. 3.11).

The point cloud was rotated $30.4876\ ^{o}$ to align the axes with the cross-shore and alongshore direction of the beach. A 22 meter wide segment containing the soil sampling transect was selected. This segment was cleaned where points that belonged to objects on the beach were removed (e.g. signposts, people).

The x-coordinates of the segment were offset to match the position of the ADV at x=0. The z-coordinates were translated 0.1 m upward to align the segment with the GPS-measurements of the soil samples. Next a grid was created with cell widths of $dx = 1$ m and $dy = 1$ m where cells with an elevation higher than 6.0 m were removed. From the gridded bathymetry (fig. 3.14) the transect closest to the soil sample locations was selected as the representative 1D cross-shore profile. Transect profiles have been created for each low water during a period of 10 days.

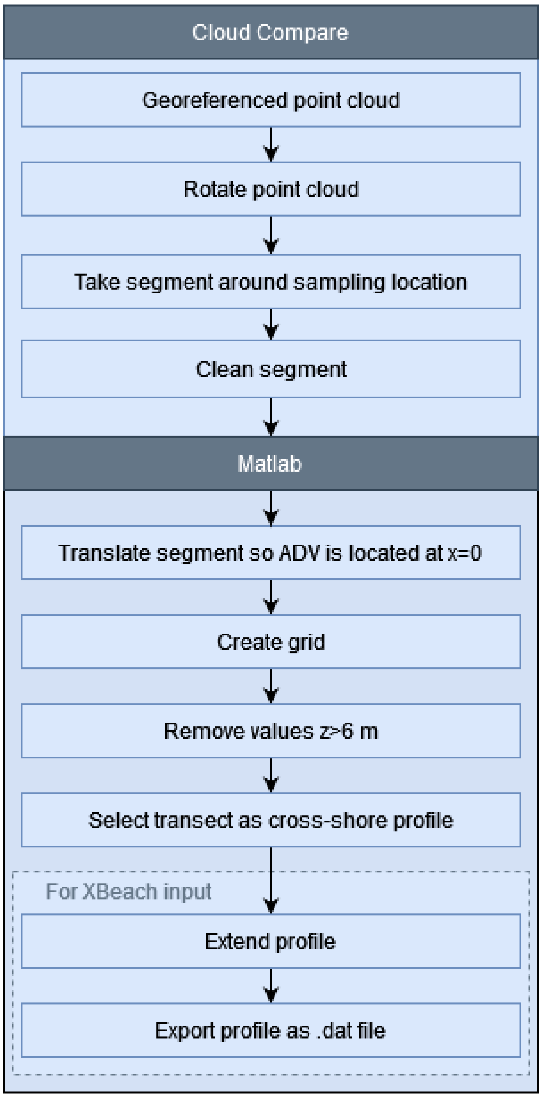

Figure 3.11: Laser scan processing steps from a georeferenced point cloud to a gridded 1D cross-shore profile

For the initial cross-shore profile of the XBeach model two additional steps were required. First, the bed level at the ADV (d_{ADV}) was calibrated for and set to -0.5 meter and the missing values between the ADV and the profile were filled in with linear extrapolation. Second, to prevent large boundary effects near the sandbar the profile was extended for 20 meters in the offshore direction. Due to the extension the wave signal measured at the ADV was imposed 20 meter further offshore. To prevent deformation of the incoming wave signal the extension was kept horizontal.

3.2.5. Wind sensor

The wind data is not needed as an input for XBeach, but is useful to see whether the intertidal zone has been under the influence of the wind during low water. As such it has also been used to determine the model period. The source of the wind data is the Windguru wind station installed on the roof of the local sailing club. It is estimated that this station measures the wind velocity and direction at a height of 3 meters from the beach. The wind data has been converted from knots to m/s. The velocity vector has been decomposed into a cross-shore component u_{wind} and an alongshore component v_{wind}.

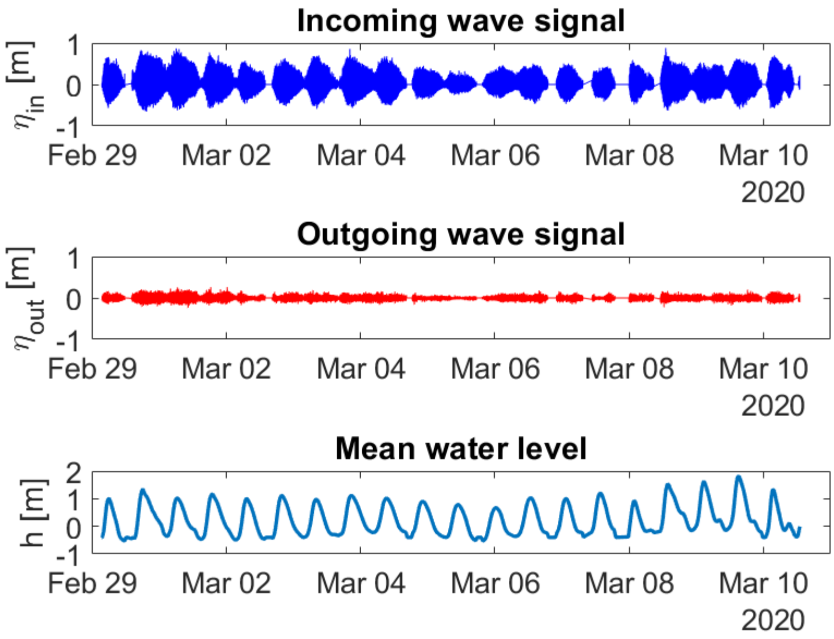

Figure 3.12: Results of the wave and tidal analysis on the ADV signal. a) incoming waves, b) outgoing waves, c) half-hourly mean water level

3.3. Data processing

With the Scanex fieldwork campaign large amounts of data was collected. This provides a good overview of the situation in the intertidal zone. In this section the results of the data processing is presented.

3.3.1. Wave and tidal conditions

For the period of approximately eleven days, the incoming and outgoing waves are shown in figure 3.12a and 3.12b. This shows that the wave conditions at the ADV location were dominated by incoming waves and reflections were generally small. In figure 3.12c the tidal signal is shown.

3.3.2. Grain size distribution in the intertidal zone

The sieve analysis showed that individual soil samples on the transect are all well sorted with fine to medium sand (see Appendix A), however they show a clear variation in both cross-shore space and time of the D_{50} at the transect (fig. 3.13). As these cross-shore variations are markedly different from each other it is not possible to determine a clear trend in the cross-shore variation.

During sampling one sample was taken at each of the sampling locations along the transect. To still get an indication of the spatial variability of the sampling, two instances of local sampling in the intertidal zone were investigated. In both cases one additional sample of the 2 mm top layer was taken within a meter distance of the first sample. On 23-3-2020 a difference in the nominal grainsize of 17 μm was observed between the two samples. On 21-11-2021, outside of the Scanex campaign, a difference of 27 μm was observed between the two samples. The number of samples on both days are not large enough to reliably compute the standard deviation of the $D-50$ but based on the found differences a crude estimation is made that the actual d_{50} on the beach will be within a range of ± 20 μm of the measured d_{50}.

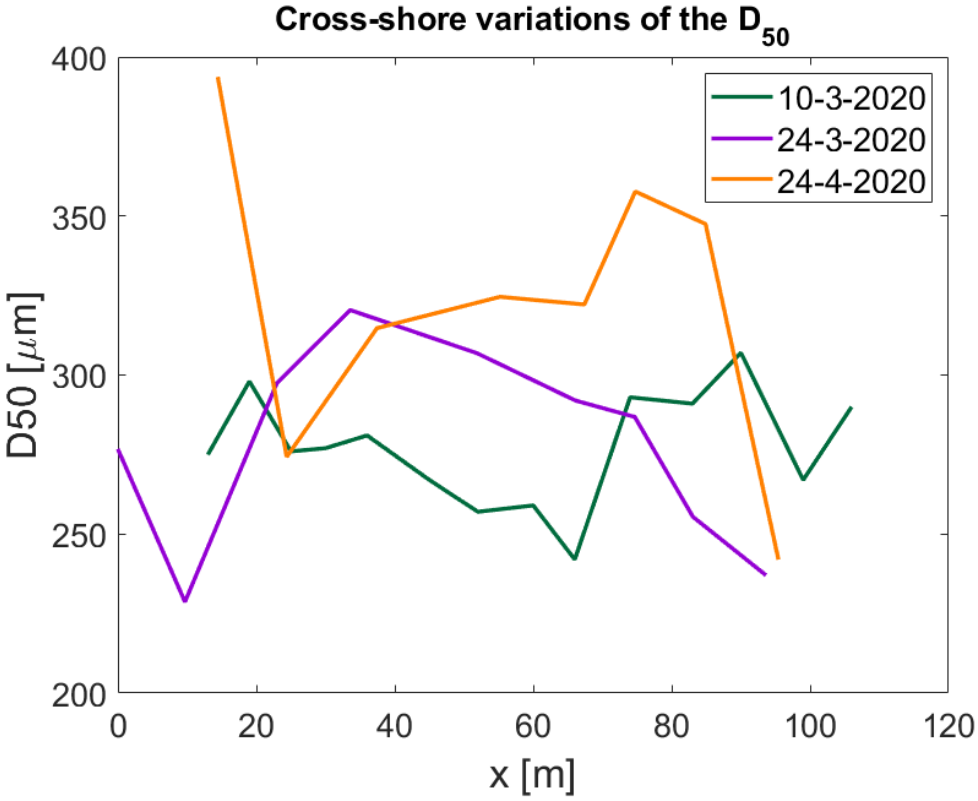

Figure 3.13: Cross-shore variations of the D_{50} on three different sampling days.

3.3.3. Morphological changes

Using the laser scan data the changes in the beach morphology can be followed in time. The initial profile shows an intertidal bar with a runnel. The bar crest is near $x = 50$ m and the bar trough near $x = 60$ m. At the 1st of March the bar has eroded. In the following 2 days the laser scan did not reach the sandbar and the sandbar behavior is unknown. On the 4th March a new sandbar is developing at $x = 40m$. It is growing and moving onshore until at the 9th of March it is nearly in the same position and the same size as the initial sandbar. At the end of the scenario, between 10th of March 00:00 and 10th of March 12:00 the sandbar was found to be eroding again.

In between the runnel and the high water line the the intertidal zone was found to be sligthly eroding at the end of the model scenario. Further, around $x = 150$ m unexpected erosion and deposition is seen between the 2nd of March 15:00 and the 6th of March 21:00.

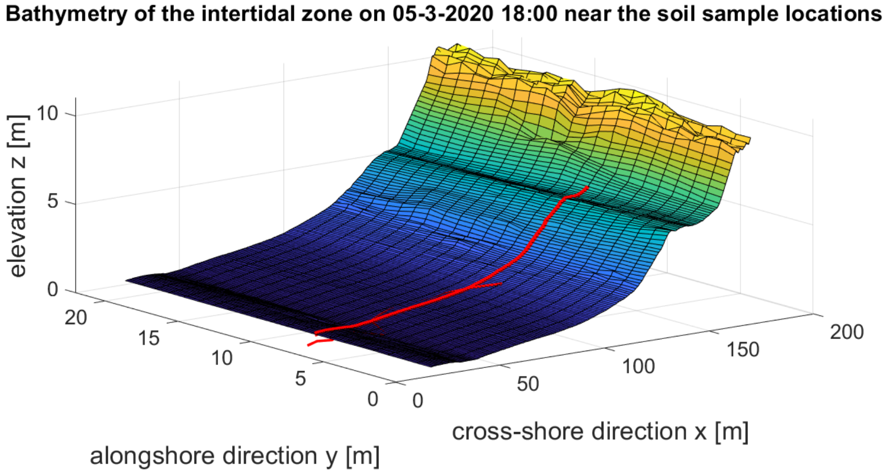

Figure 3.14: The gridded beach surface at Noordwijk on 29-2-2020 2:00. The red line corresponds to the 1D-cross-shore profile at the sampling transect.

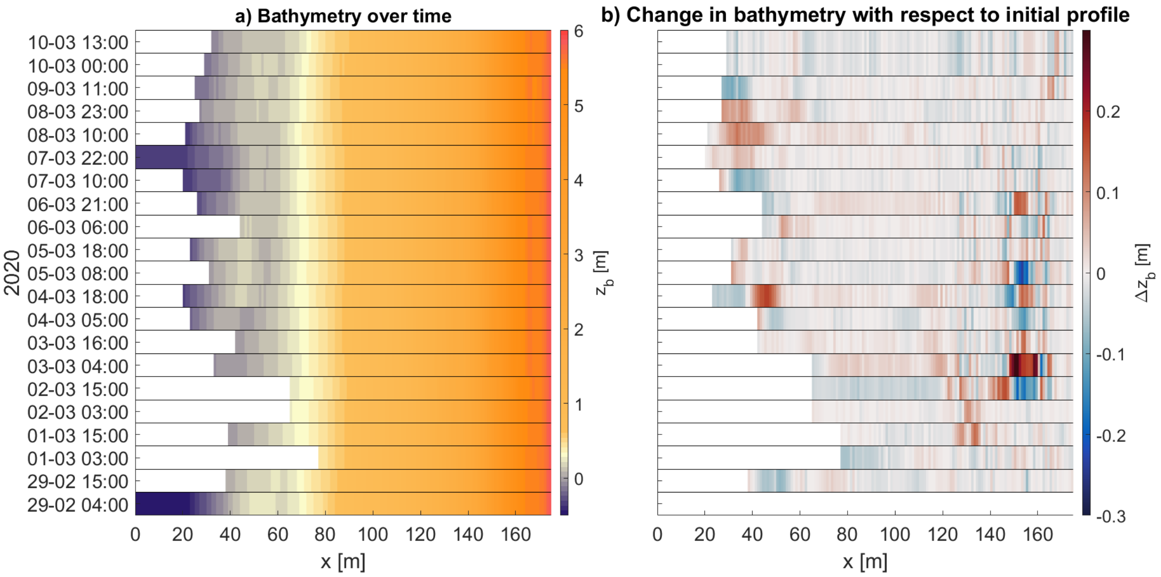

Figure 3.15: Development of the cross-shore profile from 29-2-2020 02:00 to 10-3-2020 12:00 as measured by the laser scanner during low water. a) bed level height of the cross-shore profile b) change in bed level height with respect to the initial profile of 29-2-2020 02:00.

3.3.4. Wind conditions

Figure 3.16 shows the magnitude of the wind together with the velocity component in the x-direction u_x. A positive velocity for u_x corresponds to an onshore directed wind. The magnitude of the wind velocities in combination with several considerable periods with onshore directed wind make it probable that aeolian transport has occurred on the beach over a period from 29-2-2020 to 10-3-2020.

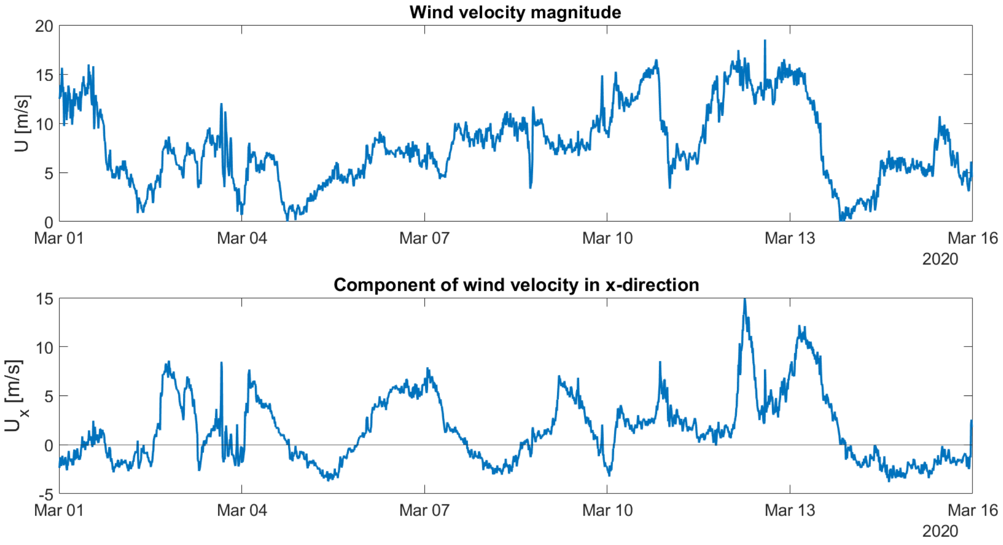

Figure 3.16: Wind velocity from the Windguru wind station. a) Wind velocity magnitude during the period off interest measured at a height of 3 m from the beach. b) The component of the wind velocity in the x-direction. Positive velocities indicate onshore wind and negative velocities indicate offshore wind.

3.4. Scenario selection

A scenario from 29-2-2020 02:00 until 10-3-2020 13:00 has been selected as the model period. In selecting the model period the wave and wind data from the Scanex fieldwork were used, as well as the significant wave height data of the IJmuiden measuring site. In deciding this period, the following considerations were taken into account:

- During the scenario both ADV data and wind data from the Windguru station should be present. The ADV data is needed for the wave input of the XBeach model and the wind data is needed when investigating the influence of aeolian transport.
- The model period should end on a day that soil samples were taken along a transect, so the modeled grain size at the end of the run can be compared to grain size of the samples.
- The model should include a storm.
- The computation time for the scenario should be less than a day.
- The scenario begins and ends during low water, so the laser scanner profiles can be used.

Based on the first two conditions the end date of the scenario was set to the 10th of March. In figure 3.17a and 3.17b can be seen that there are three sampling days in the overlap between the ADV and the wind data (25th of February, 10th of March, 25th of March). However, only the 10th of March meets the requirements. On the 25th of February there was a high set up on the beach and not the full intertidal zone was sampled and in the period right before the 25th of March the ADV data was unreliable and filtered from the dataset. The start date of the scenario has been selected based on the significant wave height data at the IJgeul (fig. 3.17c). In the days before the 10th of March the wave conditions were mild. To include high energetic conditions the start of the model period was set to right before the storm on 29th of February.

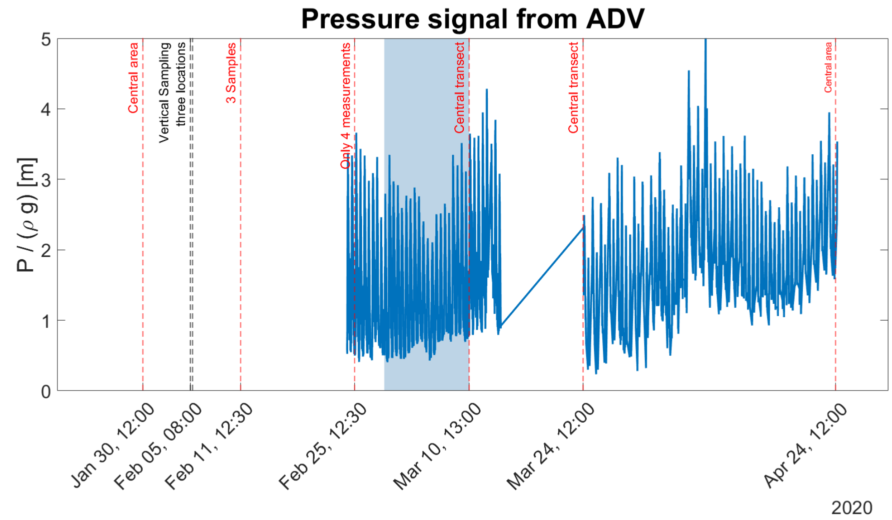

(a) Filtered pressure signal from the ADV

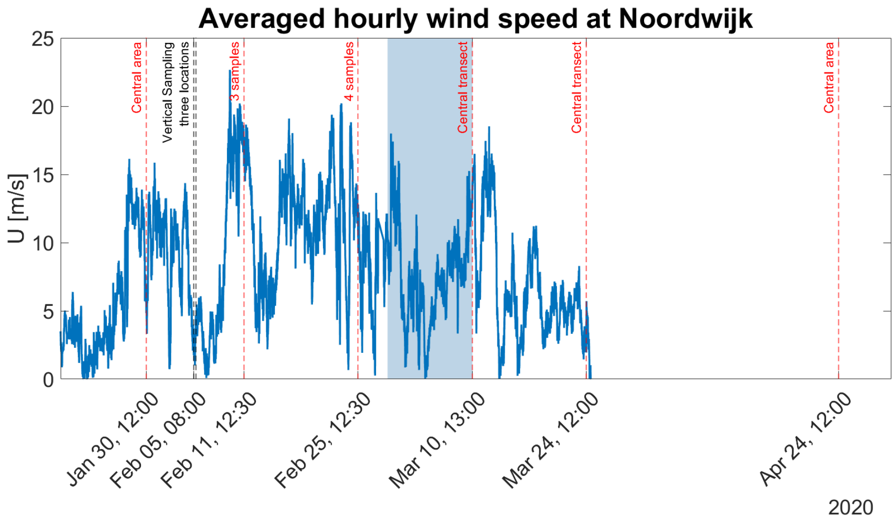

(b) Averaged hourly wind speed from the Windguru station

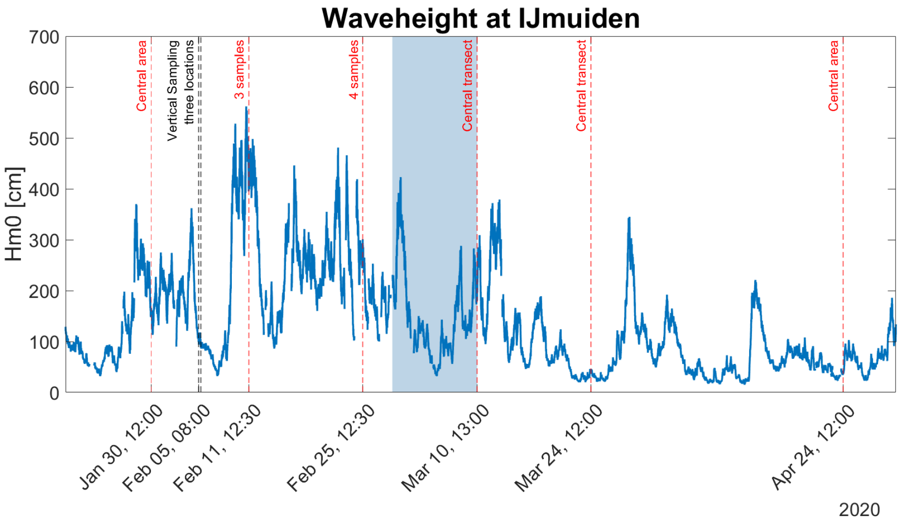

(c) Significant wave height at IJmuiden Stroommeetpaal

Figure 3.17: Scenario selection based on available pressure, wind, soil and waveheight data during the ScanEx fieldwork. The dashed, vertical lines mark the dates of surface soil sampling (red) and vertical soil sampling (black). The light blue area marks the selected model scenario. a) Filtered pressure signal from the ADV b) Averaged hourly wind speed from the Windguru station c) Significant wave height at the IJmuiden Stroommeetpaal.

4

XBeach Modelling

A one-dimensional non-linear shallow water XBeach model will be used to research the cross-shore grain size distribution in the intertidal zone. The choice for this model is motivated in section 4.1 and the model background is presented in section 4.2. The model will be used to perform a standard model run of which the setup is presented in section 4.3.1. Additionally, a five-day model run has been used to investigate the effect of a storm on the model result, sensitivity runs have been used to discern the sensitivity of the model to seven different parameters and the effect of aeolian transport has been simulated in the aeolian runs. These additional runs are presented in section 4.3.2, 4.3.3 and 4.3.4 respectively.

4.1. Choice of model

The intertidal zone has been modelled with a 1D NLSW XBeach model. By assuming that the beach morphology is mainly one dimensional and the incoming waves are in shallow water, computational time can be saved, while still solving for individual short waves. Based on the field work data these assumptions are valid and the trade-off between the errors introduced by simplifying the model and the computational effort is acceptable.

The laser scans (see section 3.2.4) show, that Noordwijk has a system with an intertidal bar and runnel (fig. 4.1). At the falling tide the runnel will empty into the sea via outflow channels, creating an alongshore flow. This flow generates a bed shear stress on the grains causing alongshore transports. As the bathymetry at Noordwijk shows small alongshore variability, large alongshore transport gradients are unlikely and the effect of the flow in the runnel is limited.

The ADV data (see section 3.2.2) was used to compute the kh-values and check the shallow water conditions. The kh-value is the product of the water depth and the wave number. Values smaller than 0.3 are associated with shallow water. For each half hour of the model period the kh-value has been computed with the mean water level and the wave number derived from the ensemble averaged amplitude spectrum of six consecutive five-minute wave records (fig. 4.2). For 60.8% of the time the kh-value was smaller than 0.3 and waves were in shallow water. For the rest of the time the values remain on the lower side of the range for intermediate waters. The computation of the kh-value contains uncertainties due to the error in the amplitude spectrum and the changing bed level over time, but provides a good indication that the errors introduced by using the shallow water equations remain within reasonable limits.

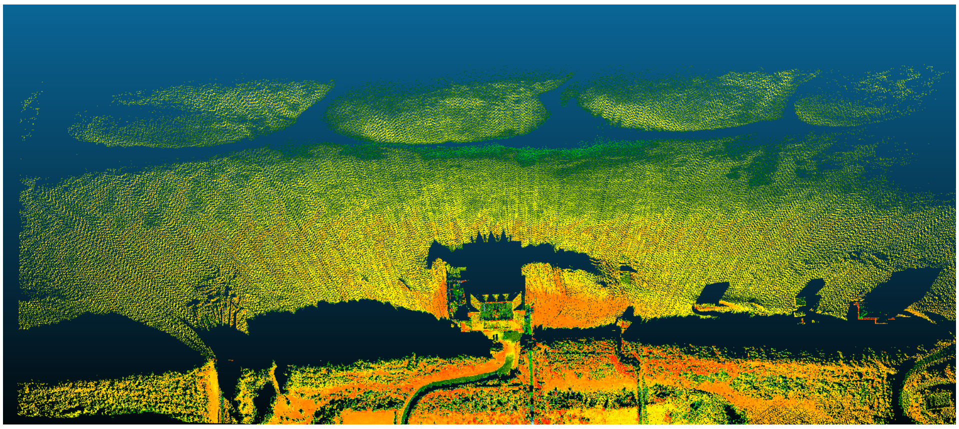

Figure 4.1: Laser scanner point cloud showing the intertidal bar and runnel at Noordwijk. Alongshore variation in the bathymetry is present as water flows alongshore through the runnel and empties into the sea via the outflow channels. The sea is black and at the top of the figure. In the centre of the figure the beach club can be discerned.

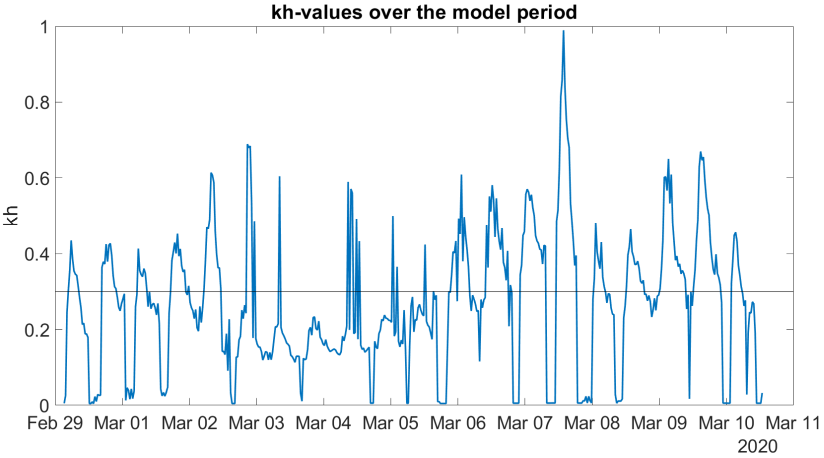

Figure 4.2: The kh-values during the model period. The black line represents limit of kh < 0.3, below which waves can be considered in shallow water.

4.2. XBeach model background

The 1D NLSW XBeach model only considers the cross-shore processes and bathymetry and simplyfies the hydraulics by using the shallow water equations. In this section the background information on the hydraulic, turbulence, bed composition and sediment transport models are provided. Except where indicated otherwise, this section is based on Reniers et al. (2013).

The basis for the hydraulic model are the shallow water equations. In the cross-shore direction the continuity and momentum equation are:

$$\frac{\partial \eta}{\partial t} + \frac{\partial hu}{\partial x} = 0 \tag{4.1}$$

$$\frac{\partial u}{\partial t} + u\frac{\partial u}{\partial x} - \nu_h\left(\frac{\partial^2 u}{\partial x^2}\right) = -\frac{\tau_{bx}}{\rho h} - g\frac{\partial \eta}{\partial x} \tag{4.2}$$

where:

η = surface elevation
h = water depth
u = cross-shore velocity
ν_h = turbulent horizontal viscosity
τ_{bx} = bed shear stress in cross-shore direction
ρ = water density

4.2.1. Turbulence

Wave breaking is implicitly modelled by the NLSWE resulting in bores, but the turbulent motions associated with wave breaking are not resolved with it. To account for turbulence a turbulence model with a depth-averaged turbulent kinetic energy balance is used.

Turbulence is generated when waves break and a surface roller is created. The surface roller R is modelled using a critical slope m_{cr} above which waves are breaking and a corresponding critical surface elevation η_{cr} that varies in height along the wave (fig. 4.3). The surface roller is defined as the part of the wave above the critical slope and the change in roller thickness over time can be defined as:

$$\frac{\partial R}{\partial t} = \left[max \left[\frac{\partial \eta}{\partial t}, 0 \right] - \frac{\partial \eta_{cr}}{\partial t} \right] \tag{4.3}$$

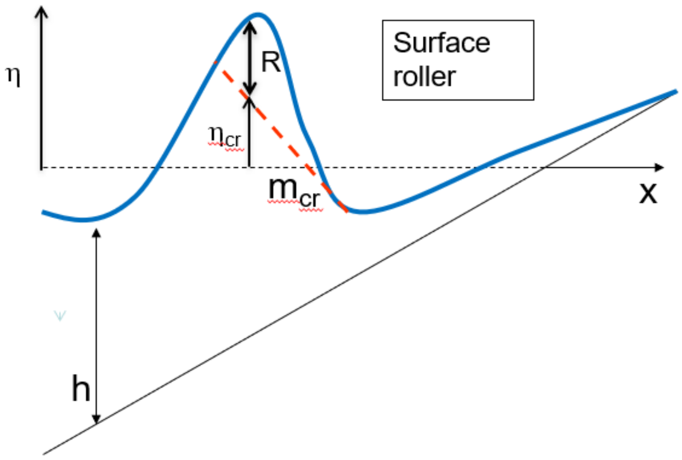

Figure 4.3: The critical slope m_{cr} is marked with the red dashed line and determines the critical surface elevation $\eta_{cr}|$. The part of the wave above the critical slope is considered to be the roller. The roller thickness R is the difference between the surface elevation η and the critical surface elevation (Adapted from A.J.H.M. Reniers, personal communication).

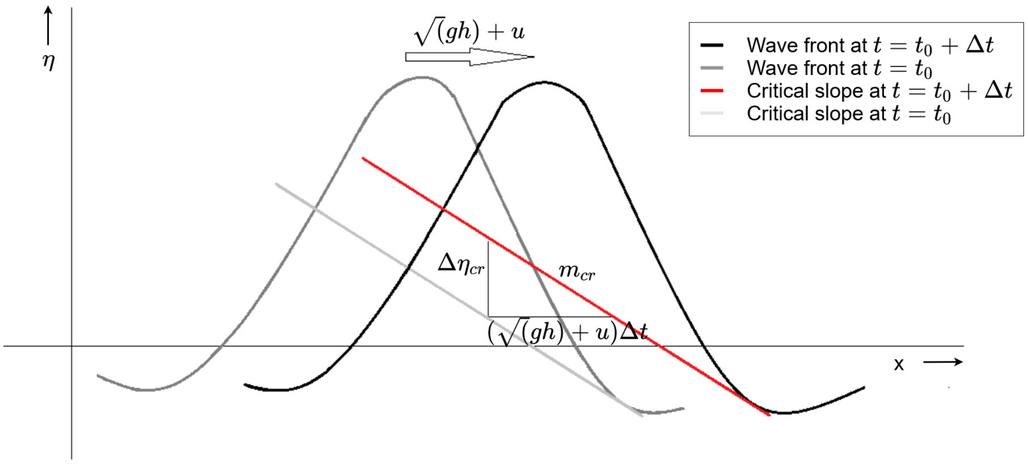

Figure 4.4: Time dependent critical surface elevation. A wave front moving with a velocity of $\sqrt{(}gh) + u$ is depicted at $t = t_o$ (grey) and $t = t_o + \Delta t$ (black). The critical slopes have been included with grey and red lines. The propagation of the wave results in a change of the critical surface elevation ηcr over time.

The change in critical surface elevation over time is found when considering that the wave front travels in shallow water with a velocity of $\sqrt{gh} + u$. In a period of Δt the wave front will have moved a distance of

$(\sqrt{gh}+u)*\Delta t$, while the critical surface elevation changes with $\Delta\eta_{cr}$ (fig. 4.4). The critical slope m_{cr} can be expressed as the ratio of these two terms (eq. 4.4). Rewriting the equation and taking the limit $\Delta t \rightarrow 0$ results in the formulation of the change in critical surface elevation over time (eq. 4.5).

$$m_{cr} = \frac{\eta_{t0+\Delta t} - \eta_{t0}}{\left(\sqrt{gh}+u\right)*\Delta t} \tag{4.4}$$

$$\frac{\partial \eta_{cr}}{\partial t} = m_{cr}\left(\sqrt{gh}+u\right) \tag{4.5}$$

The turbulent kinetic in the system is solved with a depth-averaged turbulent kinetic energy balance (eq. 4.6). The overline denotes that the turbulent kinetic energy is averaged over a representative time period T_{rep}. On the right hand side of the equation are the source and sink terms for the turbulence. The source term represents the turbulent kinetic energy generated in the surface roller (eq. 4.7). The sink term represents the dissipation of turbulent kinetic energy into heat on the smallest turbulent scales (eq. 4.8). Both the source and the sink contain a turbulence calibration parameter.

$$\frac{\partial \overline{k}h}{\partial t} + \frac{\partial \overline{k}hu}{\partial x} = S_w - S_r \tag{4.6}$$

$$S_w = c_r R g \frac{\partial \eta_{cr}}{\partial t} \tag{4.7}$$

$$S_r = c_k \overline{k}^{\frac{3}{2}} \tag{4.8}$$

where:

$\overline{k}$ = time averaged turbulent kinetic energy
S_w = turbulent kinetic energy source
S_r = turbulent kinetic energy sink
c_r = calibration factor for the turbulent kinetic energy source
c_k = calibration factor for the turbulent kinetic energy sink

Since the turbulence at the bed is important for the pick up of sediment, an exponential function is used to relate the depth-averaged kinetic energy k_{bed} to the turbulent kinetic energy at the bed:

$$k_{bed} = \overline{k}\frac{1}{exp\left(\frac{h}{R}\right)} \tag{4.9}$$

4.2.2. Bed composition

XBeach can take into account the grain size distribution by defining j sediment classes and their fractions p_j to the total sediment. Each sediment class is characterized by their D_{50} and optionally their D_{10} and D_{90} (XBeachDocs, 2020).

When more than one grain size class is used, multiple bed layers need to be specified. Three different types of bed layers can be distinguished. The first type is the top layer with a constant thickness. It is the only layer that is exposed to the water or air column and it is therefore the only layer that undergoes erosion or deposition. The second type is the variable layer that, as the name implies, can vary in thickness to account for erosion and deposition of the bed. The third type is the passive layer with a constant thickness (XBeachDocs, 2020).

After erosion of the top layer, sediment is supplied from the underlying layers up to the variable layer to maintain the constant thickness of the top layer and passive layers. If the variable layer becomes too small, it merges with the passive layer underneath it. A new passive layer is then added at the bottom to keep the number of bed layers the same. In a similar way, when sediment is deposited on the top layer, sediment is passed to the variable layer. If the variable layer becomes too large, the variable layer is split in two and the bottom passive layer is removed (XBeachDocs, 2020).

The movement sediment from one layer to another, caused by deposition and erosion, introduces numerical mixing to the model. An example of this is given in figure 4.5 (Van der Zwaag, 2014). Here, a layer fine

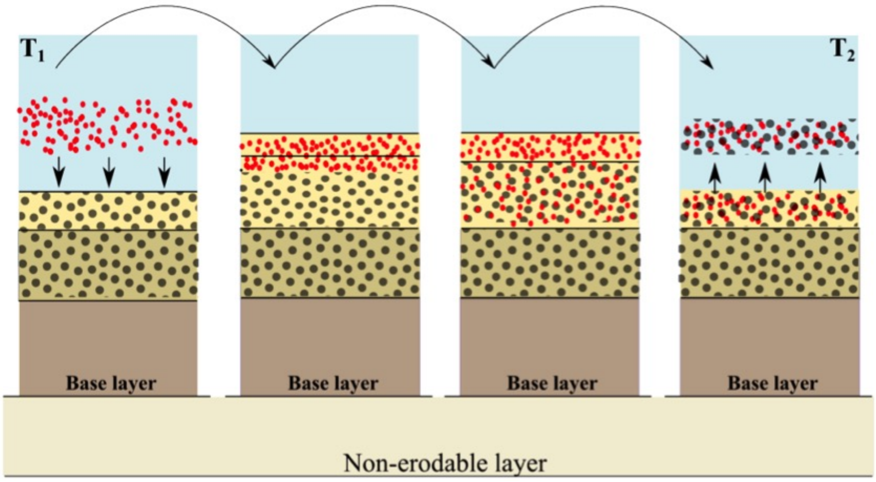

Figure 4.5: Example of numerical mixing in XBeach. A layer of fine sediment is deposited and forms the new top layer and part of the layer underneath. The sediment is evenly distributed throughout the underlying layer. When in a next time step erosion occurs, not only the fine sediment but the coarser sediment is eroded as well (Van der Zwaag, 2014 as depicted in XBeachDocs(2020))

material is deposited on the top layer. The top layer is of constant thickness and shifts upwards, and some of the fine sediment is transferred to the layer underneath. The sediment fractions are then distributed uniformly over the grid cell, mixing the coarser grains with the fine grains. When subsequently erosion occurs, in stead of removing the original layer of fines, some coarse grains are removed as well and some fine grains are left behind (XBeachDocs, 2020). This demonstrates the importance of selecting a right bed level thickness of the same order as the expected erosion or deposition. Too large bed layers will result in a too uniform behaviour of the grain size distribution, while too small bed layers will result in too much numerical mixing.

4.2.3. Sediment transport

The bed load transport is computed with the formulation of Meyer-Peter Muller with the acceleration effect of Nielsen. The formulation uses a wave averaged Shields parameter that includes the effect of oscillatory wave motion and the increased near-bed turbulence due to wave breaking.

$$S_b = 12\beta_s \left[max\left[|\theta'(t)| - \theta_{cr}, 0\right]\right] \sqrt{\theta'(t)} \frac{u(t)}{|u(t)|} \sqrt{\Delta g d^3} \tag{4.10}$$

where:

S_b = bed load sediment transport
β_s = slope parameter
θ' = instantaneous dimensionless shear stress
θ_{cr} = critical Shields parameter
Δ = relative density, $\frac{\rho_s - \rho}{\rho}$
d = grain diameter

The suspended sediment transport is modelled with a depth-averaged advection-diffusion equation (eq. 4.11). The equilibrium concentration is defined for wave breaking only (eq. 4.12) and includes a sediment efficiency parameter ϵ_s, that is an indicator for how well sediment can be brought into suspension. The adaptation time T_s indicates how fast sediment particles will return to the bed (eq. 4.13). A small value corresponds to a near instantaneous response and a large value to a settling lag. As the parameter includes the fall velocity, the adaptation time is dependent on the grain size. The suspended sediment transport is given by equation 4.14.

$$\frac{\partial hC}{\partial t} + \frac{\partial hCu}{\partial x} + \frac{\partial}{\partial x}[Kh\frac{\partial C}{\partial x}] = \frac{hc_{eq} - hC}{T_s} \tag{4.11}$$

$$c_{eq} = \frac{\epsilon_s k_{bed}^{\frac{3}{2}}}{w_s} \tag{4.12}$$

$$T_s = max\left(\gamma \frac{h}{w_s}, 0.01\right) \tag{4.13}$$

$$S_s = hCu + Kh\frac{\partial c}{\partial x} \tag{4.14}$$

where:

C = depth averaged concentration
K = horizontal diffusivity coefficient
c_{eq} = equilibrium concentration
ϵ_s = suspended load efficiency
k_{bed} = near bed turbulent kinetic energy
w_s = fall velocity
T_s = adaptation time
γ = calibration factor for the adaptation time T_s
S_s = suspended sediment transport

With multiple sediment classes the bed-load and suspended sediment transport are computed for each class separately. The total suspended sediment is the summation of the transports for each sediment class (eq. 4.15). In a similar way the bed elevation is computed for each sediment class and summed over all the classes (eq. 4.16).

$$S_t = \sum_{j=1}^{J} \left(S_s(j) + S_b(j)\right) \tag{4.15}$$

$$\frac{dz_b}{dt} = \sum_{j=1}^{J} \frac{dS(j))}{dx} \tag{4.16}$$

4.3. Model setup

For this research multiple model runs have been performed and the setup for these runs is presented in this section. First, the standard run provides the baseline model result. Additionally, the five-day run, the sensitivity runs and the aeolian run are variations on the the standard run. For the five-day run the model period is reduced to exclude the storm at the start of the model period. In the sensitivity runs is tested how sensitive the model is to 7 parameters. In the aeolian run the bed composition is adjusted to simulate aeolian transport. The setup of the standard run is presented in subsection 4.3.1 and the changes to the setup for the five-day run, sensitivity runs and aeolian runs are discussed in section 4.3.2, 4.3.3 and 4.3.4 respectively.

4.3.1. Standard run setup

The standard run is the model run that after calibration provided the best model result. The model period is from 29-2-2020 02:00 until 10-3-2020 13:00 (see 3.4). The initial cross-shore profile, the wave and tidal signal and the initial bed composition are all based on the Scanex fieldwork data.

The XBeach grid consisted of three grid points in the y-direction and 176 grid points in the x-direction. The grid size was $dy = 5m$ and $dx = 1m$. For the initial cross-shore profile the laser scan of 29-2-2020 02:00 has been used. The grid points of first 20 points were fixed, meaning that sediment transports are computed to and from the cells, but the morphology and bed composition are not updated. The resulting representative profile of 29-2-2020 02:00 used as model input, is depicted in figure 4.6.

No discharge outflow point has been included to account for the lowering of the water level in the runnel. The laser scans show that during the model period both the initial as well as a newly formed intertidal bar were eroded (see fig. 3.15). Thus, the inclusion of a discharge outflow would have introduced errors to the modelling.

The incoming surface elevation and the mean water level are imposed at the offshore boundary. The outgoing reflected waves are absorbed with a Riemann boundary condition.

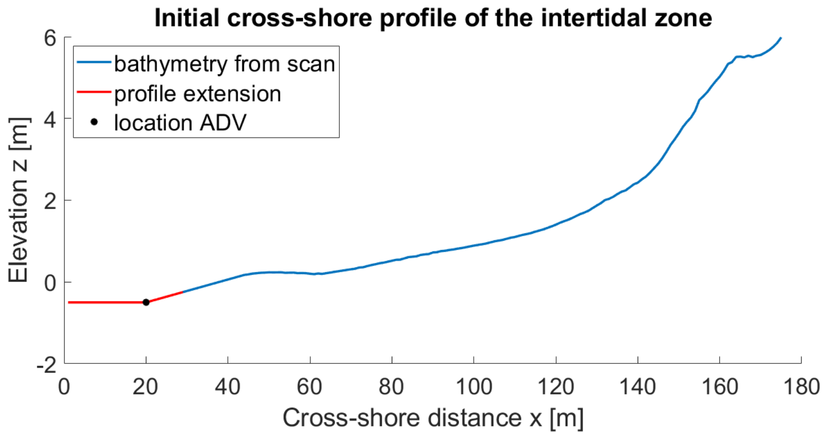

Figure 4.6: The representative cross-shore profile at the sampling transect on 29-2-2020 02:00. In blue is the profile obtained from the laser scan. In red is the extrapolation to the location of the ADV (star) and the horizontal extension needed for XBeach model input.

In the model ten bed layers have been defined. The top layer has a thickness of 2 cm and the other layers of 10 cm. The layer directly underneath the top layer is defined as the variable layer. The same initial bed composition has been applied to all grid cells in all bed layers. Table 4.1 shows the sediment classes and fractions that were used and figure 4.7 shows the grain size distribution curve. The D_{50} of the initial grain size distribution was 278 μm.

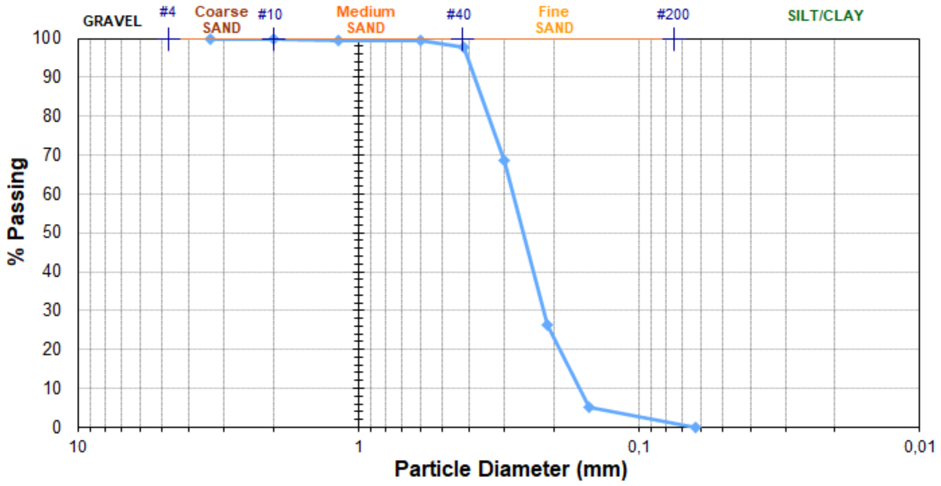

Figure 4.7: Grain size distribution in the intertidal zone on 10-03-2020

In the XBeach model a large number of parameters can be specified. The most important parameters are summarized in the table below. The settings for eps, h_{min} and T_{rep} were the smallest values that still provided a stable result. The other settings are based on (Reniers et al., 2013) (2013).

The standard model run has been calibrated based on the idea that the morphology needs to be modelled correctly for the grain size distribution to be modelled correctly as well, since the changes in morphology are a direct result of the changes of the sediment transports. Therefore, the grain size distribution of the top layer and the morphology are the model outputs that will be presented in the results. The D_{50} will be used as a rep-

Table 4.1: The grain size distribution of the combined soil samples on 10-3-2020

Grain size range [mm]	Characteristic diameter d [mm]	Mass per fraction [g]	Percentage of total mass [-]
> 0.35	0.45	4.4	0,0019
2.0 - 3.35	2.68	1.0	0,0004
1.18 -2.0	1.59	1.0	0,0008
0.6 - 1.18	0.89	5.7	0,0025
0.42 - 0.6	0.51	36.0	0,016
0.3 - 0.42	0.36	683.9	0,296
0.212 - 0.3	0.256	978.0	0,424
0.15 - 0.212	0.181	478.9	0,208
0.063 - 0.15	1.107	115.5	0,050
< 0.063	0.04	0.9	0,0004
Total		2306.8	1

Parameter	Description	Setting
C	Chezy coefficient	57
c_r	calibration factor for the turbulent kinetic energy source	0.4
c_k	calibration factor for the turbulent kinetic energy sink	0.4
m_{cr}	critical slope of wave front	0.7
ϵ_s	suspended load efficiency	0.010
γ	calibration factor for the adaptation time	0.1
$\nu_{h,fac}$	roller induced turbulent horizontal viscosity	0.3
Φ_t	bed load transport parameter	40.0
$wetslp$	critical avalanching slope under water	0.15
eps	threshold waterdepth above which cells are considered wet	0.025
h_{min}	threshold waterdepth above which Stokes drift is taken into account	0.025
T_{rep}	representative period for turbulent kinetic energy averaging	1

Table 4.2: Model parameter settings

resentative value for the grain size distribution. For the morphology the bed level and the erosion/deposition with respect to the initial profile will be used.

4.3.2. Five-day run setup

The initial grain size distribution is an averaged distribution and sediment needs to be redistributed over the cross-shore before the model represents the situation on the beach. The start of the model is important for the spinup time needed to reach a stable situation.

At the start of the standard run a storm was present. To investigate the role of a storm in the redistribution of sediment a five-day run was performed in which the storm at the start was excluded. The model period of the five-day run was from 5-2-2020 10:00 to 10-3-2020 13:00. Apart from the model period the setup was the same as for the standard run.

4.3.3. Sensitivity runs setup

The sensitivity of the model was for the seven parameters listed in table 4.3. For each parameter XBeach was run with the standard setting, a lower setting and a higher setting, while keeping the other parameters unchanged. To save on computational time the model period was limited to the first day in which the storm conditions were expected to generate the largest differences between parameter settings.

The d_{ADV} is the bed level at the position of the ADV. The model was calibrated for the d_{ADV}. Changes of the d_{ADV} result in a different initial profile, as the interpolated slope of sandbank and the horizontal offshore profile extension are both based on the imposed bed level at the ADV (fig. 4.8). For the other parameters the initial conditions remain the same as in the standard run.

The other selected parameters affect many different interconnected processes in the turbulence and sediment transport models, which affect the suspended sediment and bed load transports (fig. 4.9). In the end,

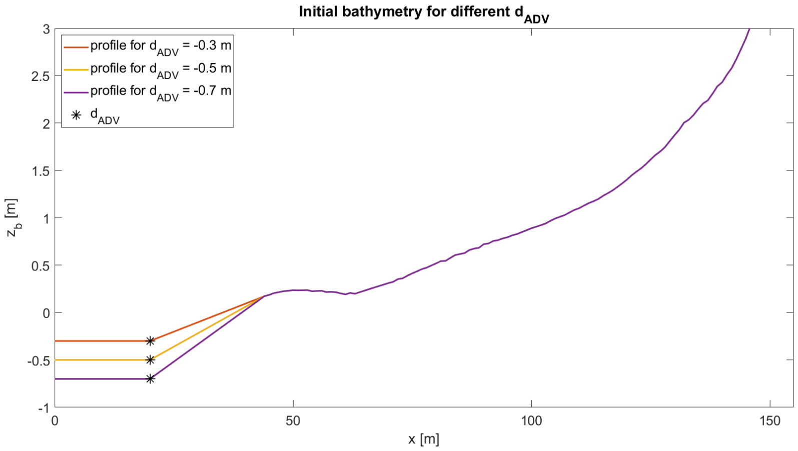

Figure 4.8: Initial profile for a d_{ADV} of -0.3, -0.5 and -0.7 m.

these processes determine the bed composition in the intertidal zone. Therefore, their sensitivity is investigated.

Parameter	Lower setting	Standard setting	Higher setting
d_{ADV}	-0.7	-0.5	-0.3
m_{cr}	0.05	0.07	0.1
T_{rep}	0.1	1	10
c_r	0.2	0.4	0.6
c_k	0.2	0.4	0.6
γ	0.05	0.1	0.2
ϵ_s	0.005	0.01	0.015

Table 4.3: Settings for the sensitivity runs

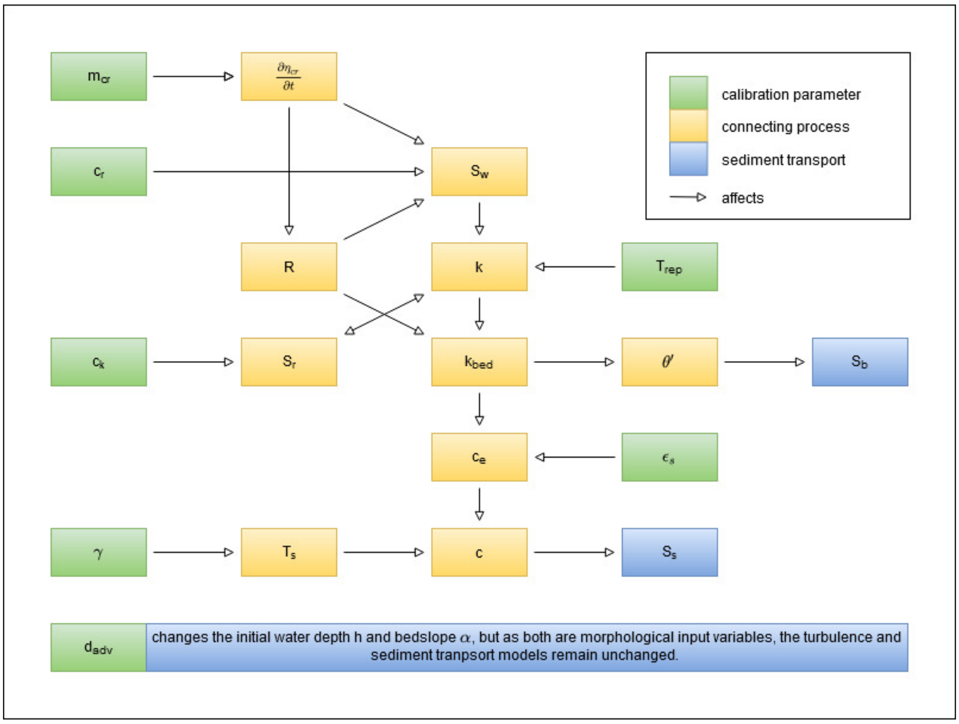

Figure 4.9: The sensitivity parameters (green) affect many different, connected processes in the turbulence and sediment transport models (yellow), which in the end affects the suspended sediment and bed load transports (blue).

4.3.4. Aeolian run setup

The combination of wind velocities and wind direction show that aeolian transport from the intertidal zone towards the dunes has likely occurred during the model period (see fig. 3.16). As XBeach cannot account for aeolian transport and aeolian transport mostly affects the smallest grain sizes, it is expected that the grain size will be underestimated when the beach is dry. To simulate the effect of aeolian transport the bed composition was reinitialized in the aeolian run. The aeolian run was paused at t = 198 h and the two smallest sediment classes were removed from the grain size distribution in the upper tidal zone from x > 120 m. The aeolian run was then completed with the adjusted grain size distribution.

5

Results

In this chapter the results of the XBeach model runs are presented. The standard model run is described in section 5.1. Next, in section 5.2 the difference is shown between the standard model run that started with a storm and the five day run in which the storm was excluded. Further, in section 5.3 the most important findings of the sensitivity runs are presented. Lastly, in section 5.4 the aeolian run is presented in which the grain size distribution has been reinitialized during the model run to simulate the effect of aeolian transport that could have occurred during the model period.

5.1. Standard model run

Figure 5.1a presents the modelled D_{50} of the top layer compared to the sampled D_{50} at the end of the model period. In the lower intertidal zone from x = 23 m to x = 56 m the D_{50} fluctuates greatly but is higher than the intitial D_{50}. The D_{50} reaches a maximum of 328.6 μm at x = 48 m and then drops markedly. At x = 57 m the D_{50} first drops below the initial D_{50} and at x = 74 m it reaches a minimum of D_{50} 260,9 μm. The D_{50} gradually increases from x = 74 m to x = 105 m, where it is approximately equal to the initial grainsize. Between the x= 106 m and x = 136 m the grain size fluctuates but remains smaller than the initial grain size. From x = 136 m and further up the beach there was no change in the D_{50}.

The morphological changes between the intitial and end profile are presented in figure 5.1b. Right at the boundary between the fixed points and free points there is a small spike of 0.03 m accretion. The beach is eroded from x = 24 m to x = 57 m with a maximum erosion of 0.22 m at x = 44 m. Between x = 58 m and x = 86 m the beach accreted and a maximum plateau of 0.14 m was reached from x = 63 m to x = 71 m. The beach shows erosion again from x = 87 m to x = 136 m. However, the erosion does not exceed 0.05 m.

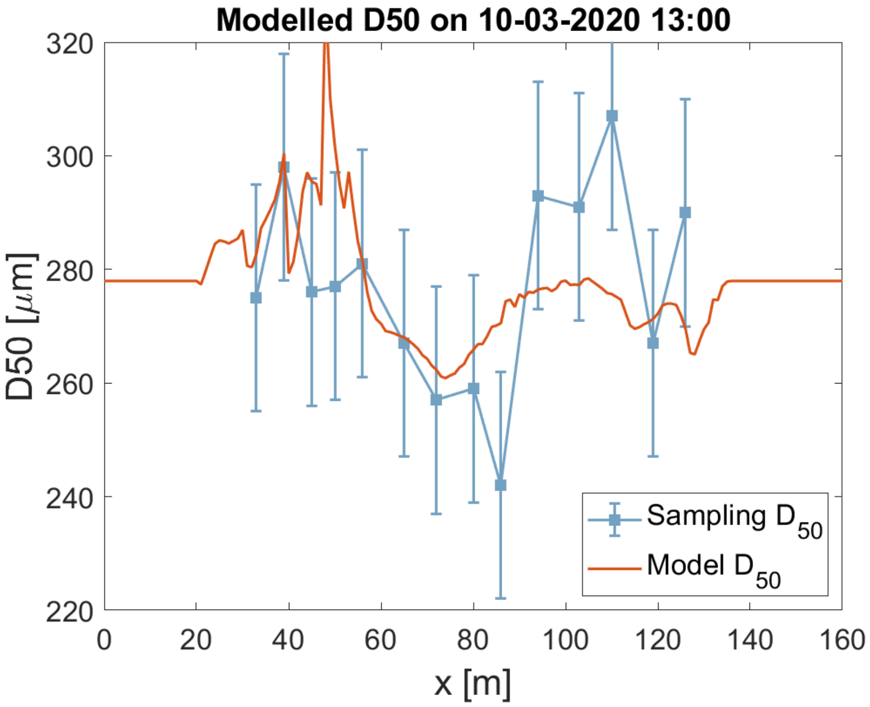

(a) Modelled D_{50} in the intertidal zone on 10-3-2020 13:00. The orange line is the modelled D_{50} of the 2 cm thick top layer. The blue dots are the D_{50} of the soil samples. The error bars show the estimated range of $\pm 25 \mu m$ for the soil sample D_{50}.

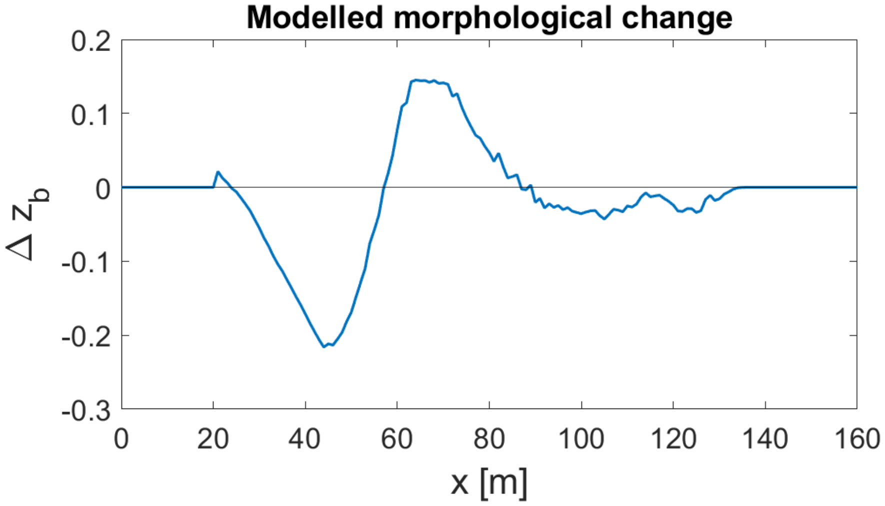

(b) Morphological change on 10-3-2020 13:00 with respect to initial profile.

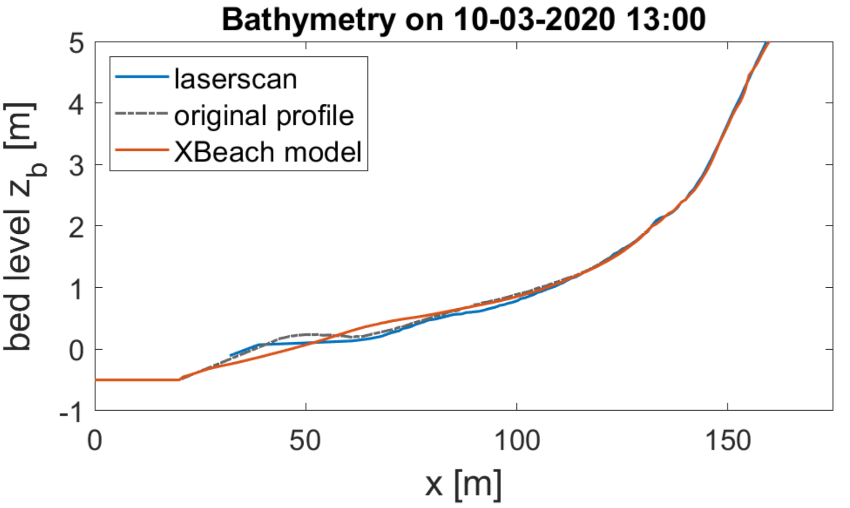

(c) Modelled bathymetry of the intertidal zone on 10-3-2020 13:00. The orange line is the modelled bathymetry, while the blue line represents the laser scan profile. The initial profile is shown with the grey dashed line.

Figure 5.1: Standard run: modelled D_{50}, bathymetry and morphological change on 10-3-2020 13:00

5.1.1. Development over time

At the start of the model period the grain size adjusts quickly (fig. 5.2a). After approximately 15 hours a cross-shore variation pattern is found that remains fairly constant over the next 185 hours. Larger grain sizes are deposited in the lower intertidal zone between x = 20 and x = 55 m. Finer particles are deposited between x = 55 m and x = 80 m and between x = 110 and x = 125 m. From x = 80 m to x = 110 m the grain size is approximately the same as the initial D50, but some small variations are seen. For values of x higher than 125 m the D50 remains unchanged.
At t = 200 h spring tide is approaching and the water line reaches its highest point during the modelling period. From this moment on the area of fine sediment is less pronounced and is found higher up the beach.

On a time scale of a single tide it can be seen that the grain size is coarser when the beach is submerged compared to when the beach is emerged (fig. 5.2b). An exception to this is near the high water line where finer sediment is found during submersion.

With regard to the bathymetry, changes to the initial profile are found after approximately 15 hours (fig. 5.3). In the region from x = 20 m to x = 55 m erosion occurs, flattening the existing sand bar. The erosion rate increases up to t=100 h after which the profile stabilizes in this region. From x = 55 m to x = 75 m the beach is accreting, the shallow trough is filled and a new sand bar starts to form. Maximum accretion is found at approximately t = 100 to t = 150 hours. After that the profile is smoothed and also the newly formed sand bar is flattened. However, the beach continues to show accretion with respect to the initial profile.

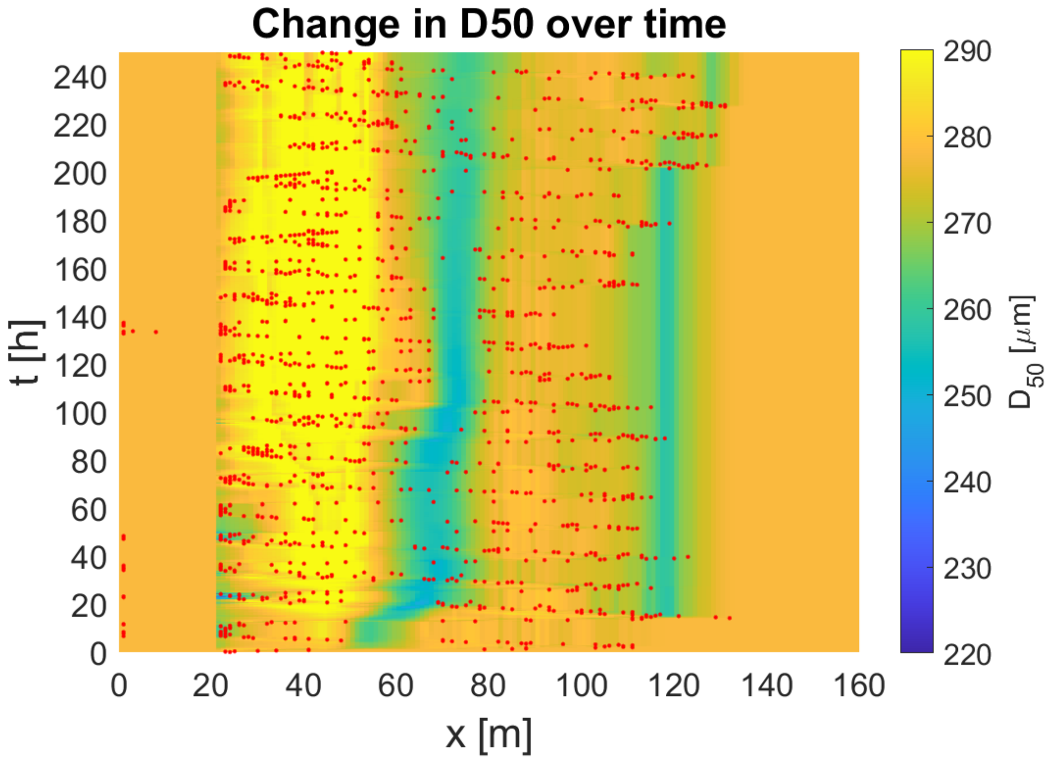

(a) a) The modelled D_50 during the full model scenario.

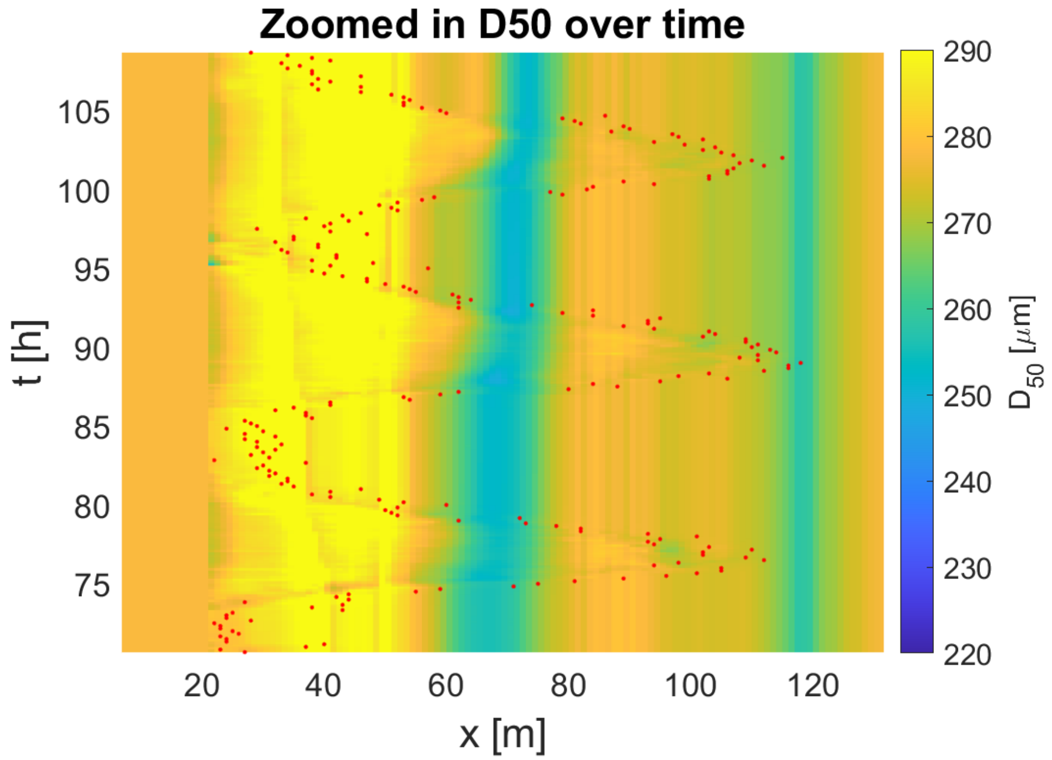

(b) b) Snapshot of the modelled grain size for three tides. Coarser sediment is found when the beach is under water, except near the water line.

Figure 5.2: Modelled grain size over time. The position of the waterline is marked with red dots.

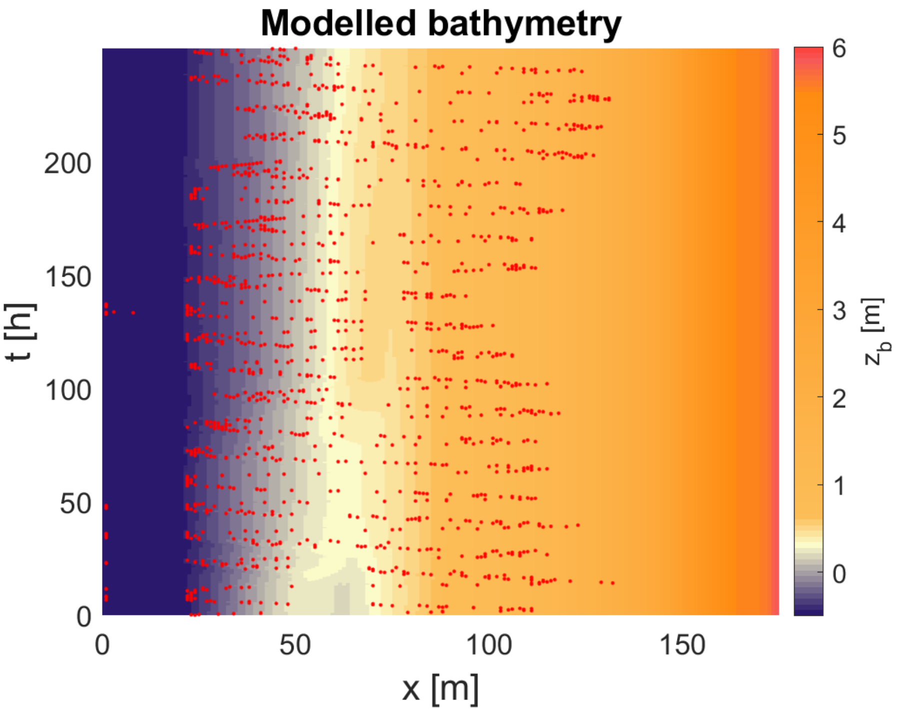

(a)

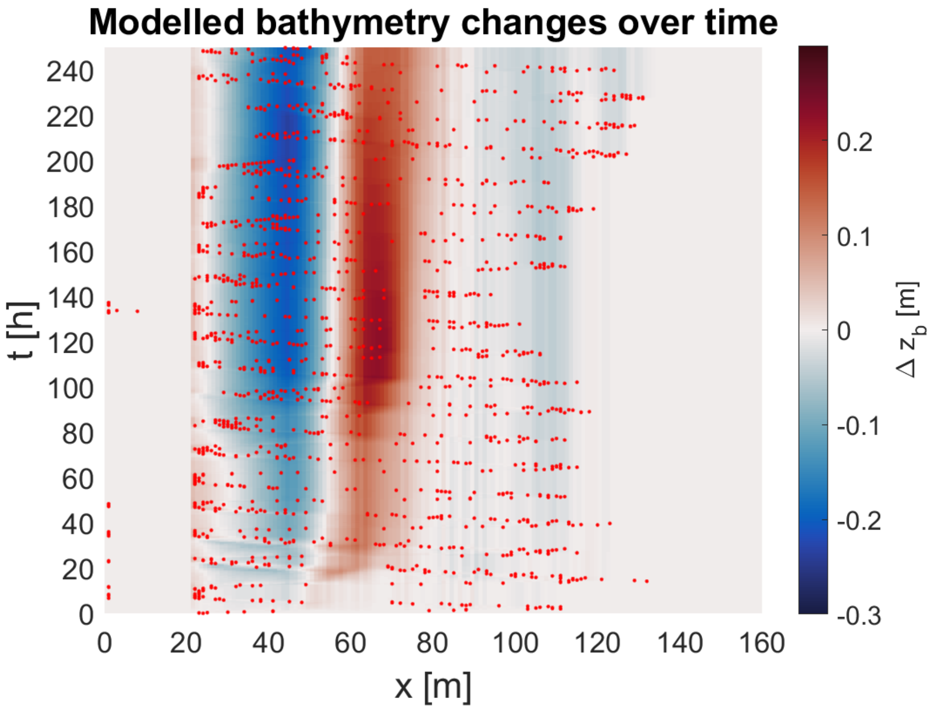

(b)

Figure 5.3: Modelled bathymetry over time. a) Modelled bed level. b) Modelled change in bed level with respect to the initial profile. In both subfigures the position of the waterline is marked with red dots.

5.2. Five-day run

The XBeach model starts with an average bed composition imposed on all the grid cells. At the start of the run the model needs time to spin up and redistribute the sediment so a representative grain size distribution on the beach is reached. The standard run started with a storm. To investigate the effect this storm has had on the spin up time a five day run has been performed from 5-3-2020 10:00 untill 10-3-2020 13:00.

In the five-day run the cross-shore variations are found to develop over time (fig. 5.4a). Fine sediment is found at the water line and with the increasing high tides the fines shift onshore. After 75 hours of simulation the cross-shore variation pattern stabilizes. When the high tide decreases at t = 122 hours, it does not significantly influence the established grain size pattern. The standard run model has a much shorter spin up time compared to the five-day run, as the cross-shore D_{50} pattern is already established after 15 hours.

At the end of the model run, a coarsening of the sediment between x = 20 and x = 48, a fining between x = 49 and x = 69 and fluctuations around the initial grain size between x = 70 and x = 134 were found (fig. 5.4b). Two local minima 260 μm are found at x = 55 and x = 122 m.

Compared to the standard run the largest differences in bathymetry are found in the middle of the intertidal zone (fig. 5.5). The local minimum grain size is positioned 19 meters more offshore (at x = 55 m versus x = 74 m). Further, the grain size changes more rapidly toward and from this minimum, resulting in a smaller area with large grain size variations followed by a larger area with less variation.

At the end of the five day run erosion of the sandbank with infilling of the trough was observed between x = 20 and x = 60 m. The maximum erosion was 0.18 m and the maximum accretion 0.07 m which is smaller than in the standard run.

In the upper half of the intertidal zone the end profile is similar to the standard run. From x = 80 m to x = 100 m erosion of 0.03 meter and from x = 100 m to x = 115 m accretion of 0.04 meter was found. Between x = 115 m and x = 134 the irregular initial profile was smoothed out.

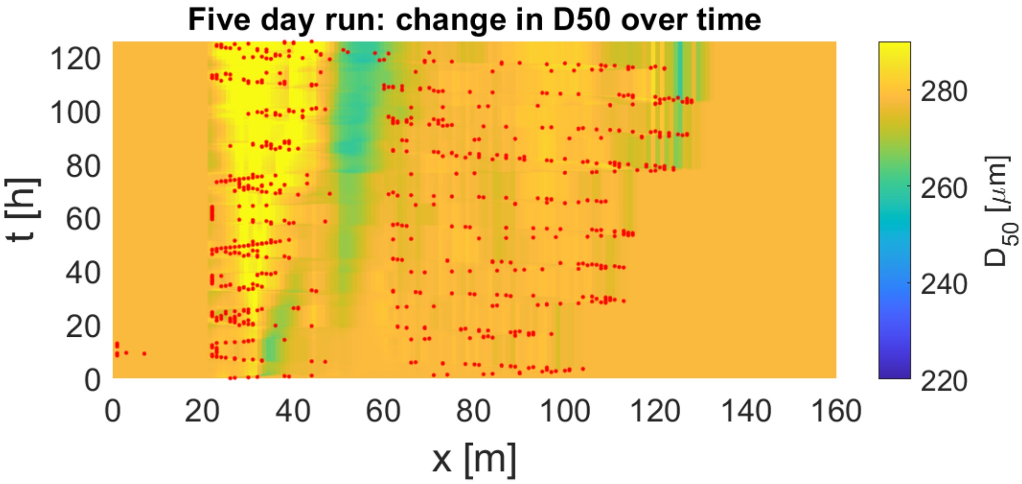

(a) Modelled D_{50} over time for a five day model period from 5-3-2020 10:00 to 10-3-2020 13:00.

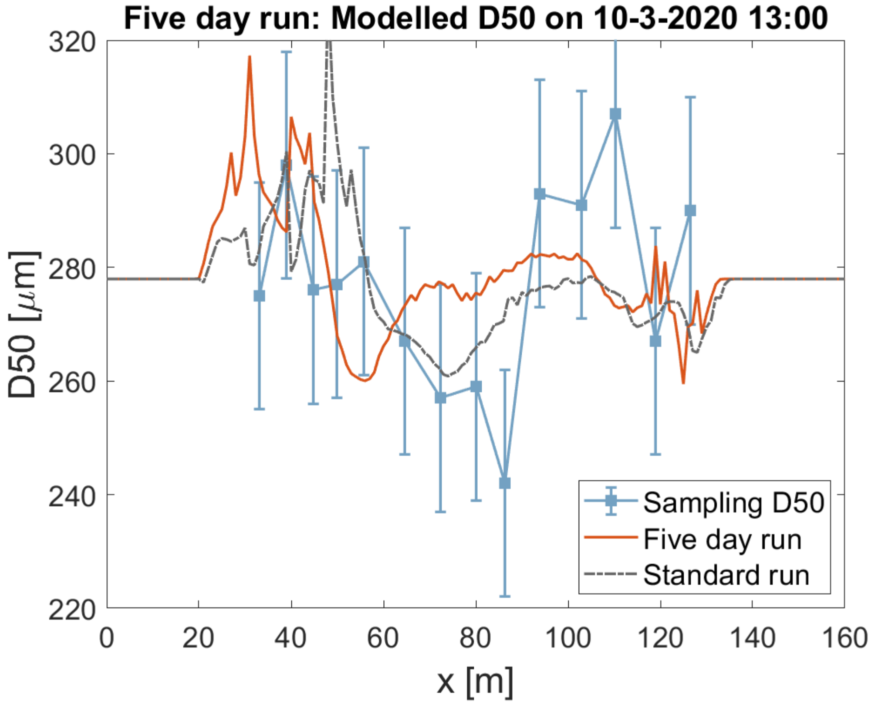

(b) Modelled cross-shore D_{50} at the end of a five day model period ranging from 5-3-2020 10:00 to 10-3-2020 13:00. The blue dots represent the soil samples taken on 10-3. The gray dashed line shows the D50 at the end of the standard run.

Figure 5.4: Modelled D_{50} for a five day model period.

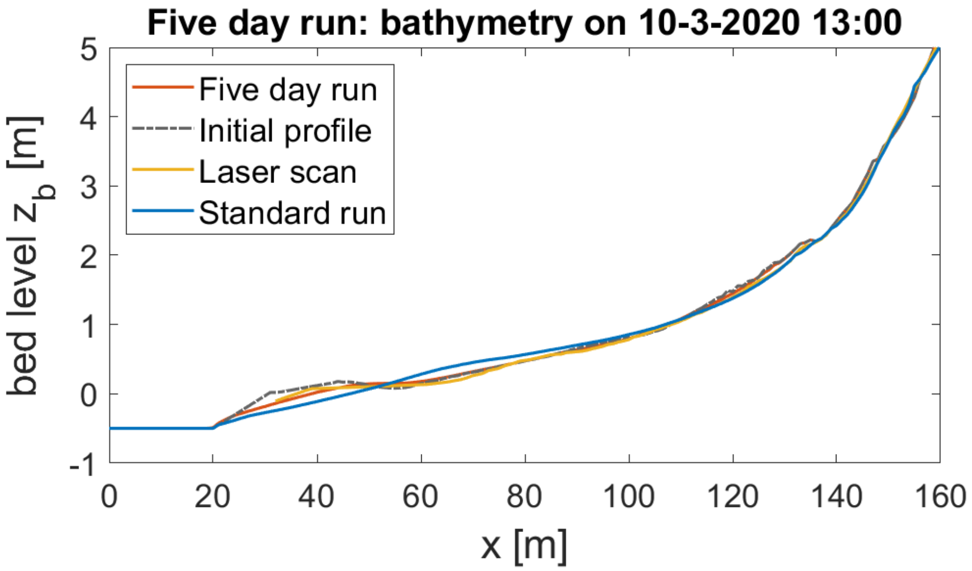

Figure 5.5: Bathymetry at the end of the modelled period ranging from 5-3-2020 10:00 to 10-3-2020 13:00. The yellow line represents the modelled result, the black line the input profile and the blue line the measured profile.

5.3. Sensitivity runs

The sensitivity of the model was tested for seven parameters, that influence the model turbulence and sediment transports and thus influence the grain size distribution in the intertidal zone (see fig. 4.9). Therefore, not only the D_{50} and morphology, but also the near bed turbulent kinetic energy, bed load and suspended sediment transport is shown. The most important findings are presented in this section. For the rest of the sensitivity results is referred to appendix B.

5.3.1. Bed level at the ADV

The cross-shore D_{50} was found to be the most sensitive to the bed level at the position of the ADV (fig. 5.6). The differences are mainly found from x = 20 m to x = 70 m. Changing the bed level results a different response at the fixed point/free point boundary. The standard setting (-0.5 m) and the higher setting (-0.3 m) give a fining of the sediment of 249 and 262 μm respectively, while the lower setting (-0.7 m) showed a coarsening of 283.3 μm.

Except for the differences at the boundary, the cross-shore variation follows a similar pattern for all three settings. However, the lower the bed level the coarser the sediment, with the largest difference between the low and the higher setting of 35 μm found at x = 46 m. The results converge going further onshore and from x = 70 m and onward no significant different between the settings is found.

In the bathymetry the main differences are in the fixed bed level and the resulting slopes towards the sandbar (fig. 5.7). Further, for $d_{ADV} = -0.7$ m the sandbar is found to be eroding and the trough is filled in. For $d_{ADV} = -0.5$ m and $d_{ADV} = -0.3$ m the sandbar migrates respectively 9 and 12 meter onshore. In the area of the initial trough most accretion takes place ranging from 6 cm for $d_{ADV} = -0.7$ m to 14 cm for $d_{ADV} = -0.3$ m. Around x = 70 m and further onshore the bathymetry is similar for all three variants.

In the first five hours of the model run the lowest bed level shows suspended sediment transports around x = 50 m, which are not present in the other runs (fig. 5.8ace). A higher bed level corresponds to larger positive and negative transports. For the bed load transport no large differences are observed between the runs (fig. 5.7). The turbulence also shows a very similar pattern, which is shifted approximately 3 m onshore for $d_{ADV} = -0.7$ m compared to $d_{ADV} = -0.3$ m (fig. 5.9).

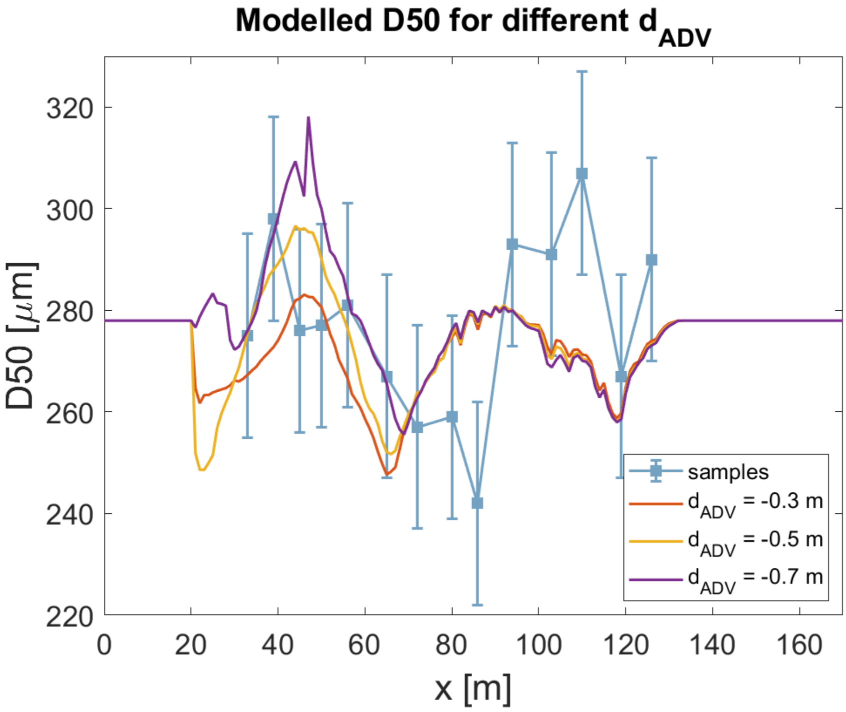

Figure 5.6: Sensitivity of the D_{50} to d_{ADV}. D_{50} for a d_{ADV} of -0.3, -0.5 and -0.7 m at the end of the model period ranging from 29-2-2020 02:00 to 1-3-2020 02:00

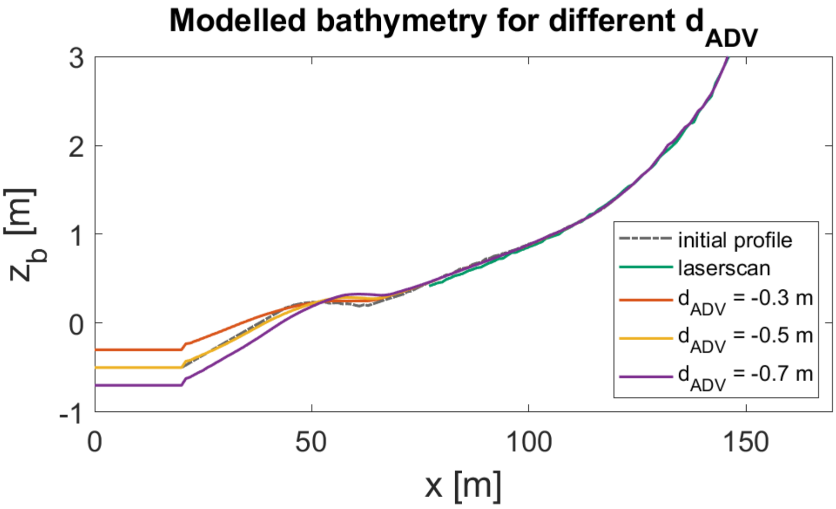

Figure 5.7: Sensitivity of the bathymetry to d_{ADV}. Bathymetry for a d_{ADV} of -0.3, -0.5 and -0.7 m at the end of the model period ranging from 29-2-2020 02:00 to 1-3-2020 02:00

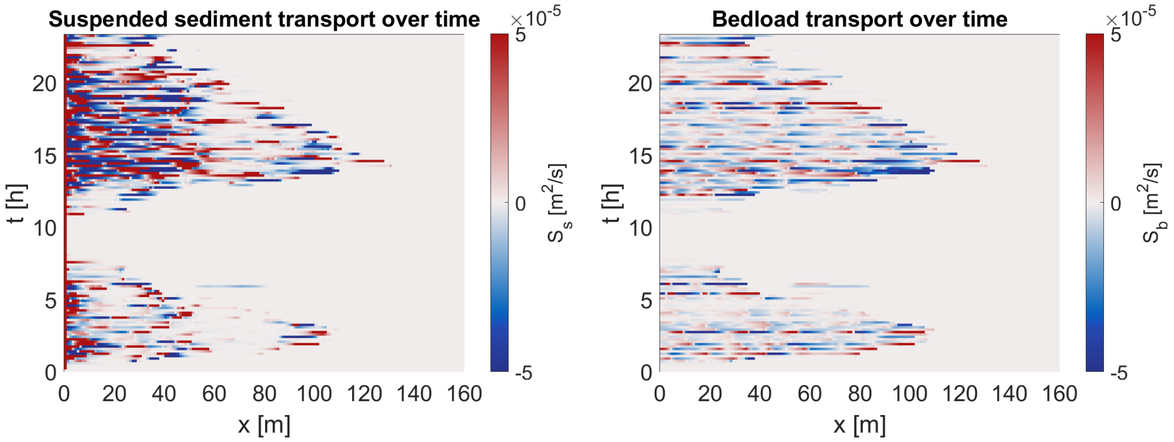

(a) $d_{ADV} = -0.7$

(b) $d_{ADV} = -0.7$

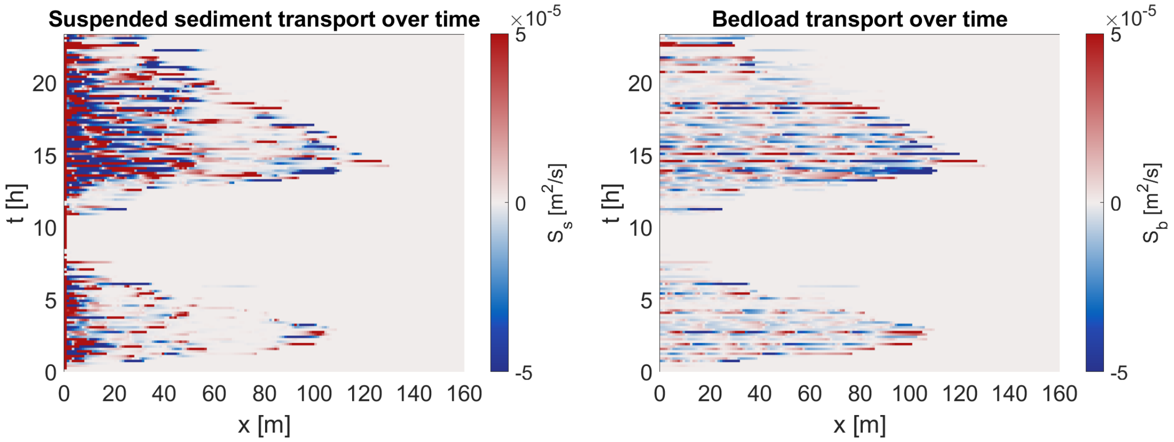

(c) $d_{ADV} = -0.5$

(d) $d_{ADV} = -0.3$

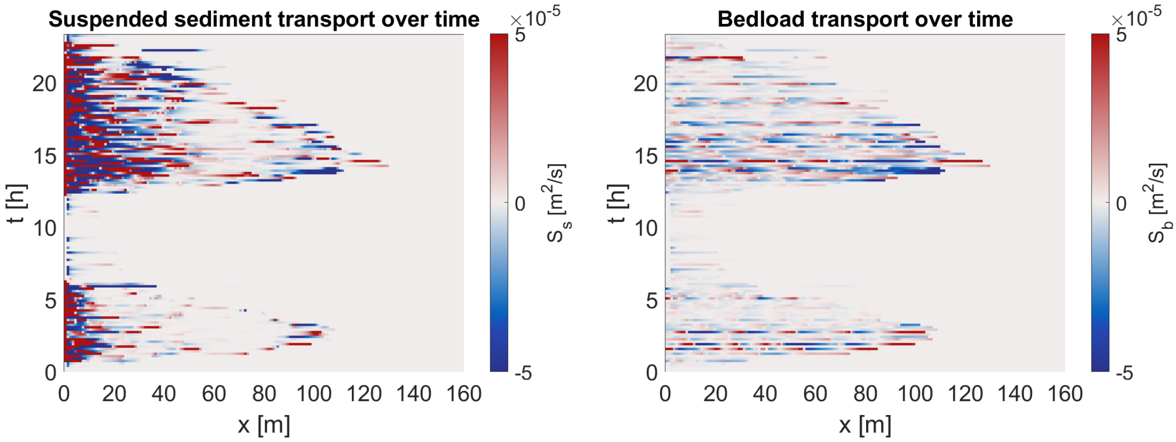

(e) $d_{ADV} = -0.3$

(f) $d_{ADV} = -0.3$

Figure 5.8: Sensitivity of sediment transports to d_{ADV}. Modelled sediment transports from 29-2-2020 02:00 to 1-3-02:00. Positive transport rates correspond to onshore transport. a)c)e) suspended sediment transport for a d_{ADV} of -0.3, -0.5 and -0.7 m respectively. b)d)f) bed load sediment transport for a d_{ADV} of -0.3, -0.5 and -0.7 m respectively.

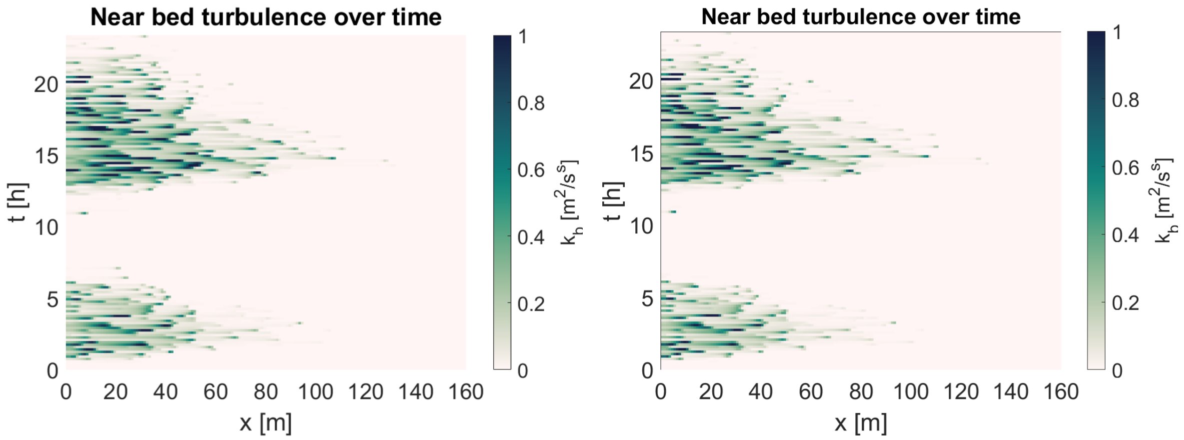

(a) $d_{ADV} = -0.7$ (b) $d_{ADV} = -0.5$

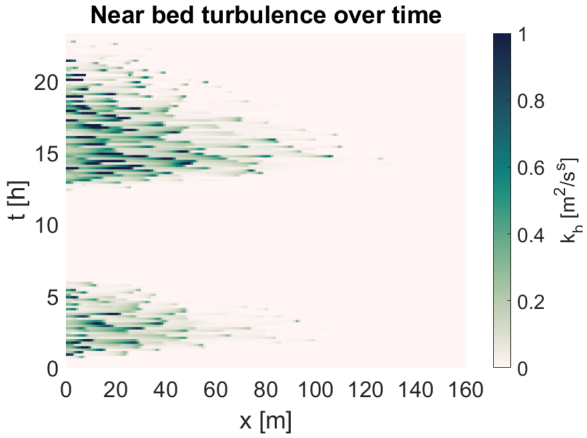

(c) $d_{ADV} = -0.3$

Figure 5.9: Sensitivity of the near bed turbulent kinetic energy to d_{ADV}. Near bed turbulent kinetic energy from 29-2-2020 02:00 to 1-3-02:00 for a $\mathrm{d}_{\mathrm{ADV}}$ of -0.3, -0.5 and -0.7 m

5.3.2. Suspended sediment parameters

Five of the tested parameters (γ, m_{cr}, ϵ_s, c_r and c_k) influence the suspended sediment transport, either via the turbulence model or suspended sediment concentration (fig. 4.9). The results of the sensitivity runs show many similarities, but some differences were found in the grain size distribution and bathymetry.

The modelled D_{50} at the fixed point boundary is very sensitive to different settings of γ (fig. 5.10c). For all three settings fining of sediment occurs, but the magnitude differs. The local minimum D_{50} for a γ of 0.2, 0.1 and 0.05 was found to be 223, 249 and 268 μm respectively. The cross-shore D50 curves converge towards the same maximum D_{50}. For the rest of the transect the model was not sensitive to γ.

For the other suspended sediment parameters the situation is the other way around, as the model is not sensitive at the fixed point boundary, but does show variations near the water line of approximately 20 μm between the high and the low parameter setting. For example, a c_r of 0.6 resulted more fines near the water line with a minimum of 251 μm, while the setting of 0.2 had a minimum of 270 μm (fig. 5.10b).

All the suspended sediment parameters give comparable results for the bathymetry. The sensitivity of the model bathymetry is limited to the sandbar behaviour. In all cases the sandbar migrates a couple of meters onshore and remains in the same position as in the standard run. However, either the low or high setting will show sandbar growth, while the other setting will show filling in of the trough and erosion of the sandbar. Which setting will result in which response depends on the parameter. From x = 70 m and further onshore the model is not sensitive to the suspended sediment parameters.

In case of γ the elevation at the location of the sandbar crest ranges from +0.34 m for a setting of 0.05 to +0.25 m for a setting of 0.2 (fig. 5.10c). In the initial bathymetry the difference between the sandbar crest and trough was 4 cm. For the standard setting of 0.1 the sandbar erodes and a difference of 1 cm remains. With a γ of 0.05 the sandbar grows and shows a difference of 7 cm, while with a γ of 0.2 the trough has disappeared.

5.3.3. Turbulent kinetic energy averaging

The T_{rep} sensitivity runs demonstrate that not all parameters can be chosen freely. In this case, the model computes normally with a T_{rep} of 1 or 10 seconds, while with a setting of 0.1 second the model becomes unstable. This results in complete erosion of the beach profile at the start of the run 5.11a and a unreliable cross-shore D_{50} 5.11b. The instability also extends to points that should have been fixed. Even though the first 20 meter were set as fixed points, the bathymetry and the D_{50} already start to change at x = 16 m.

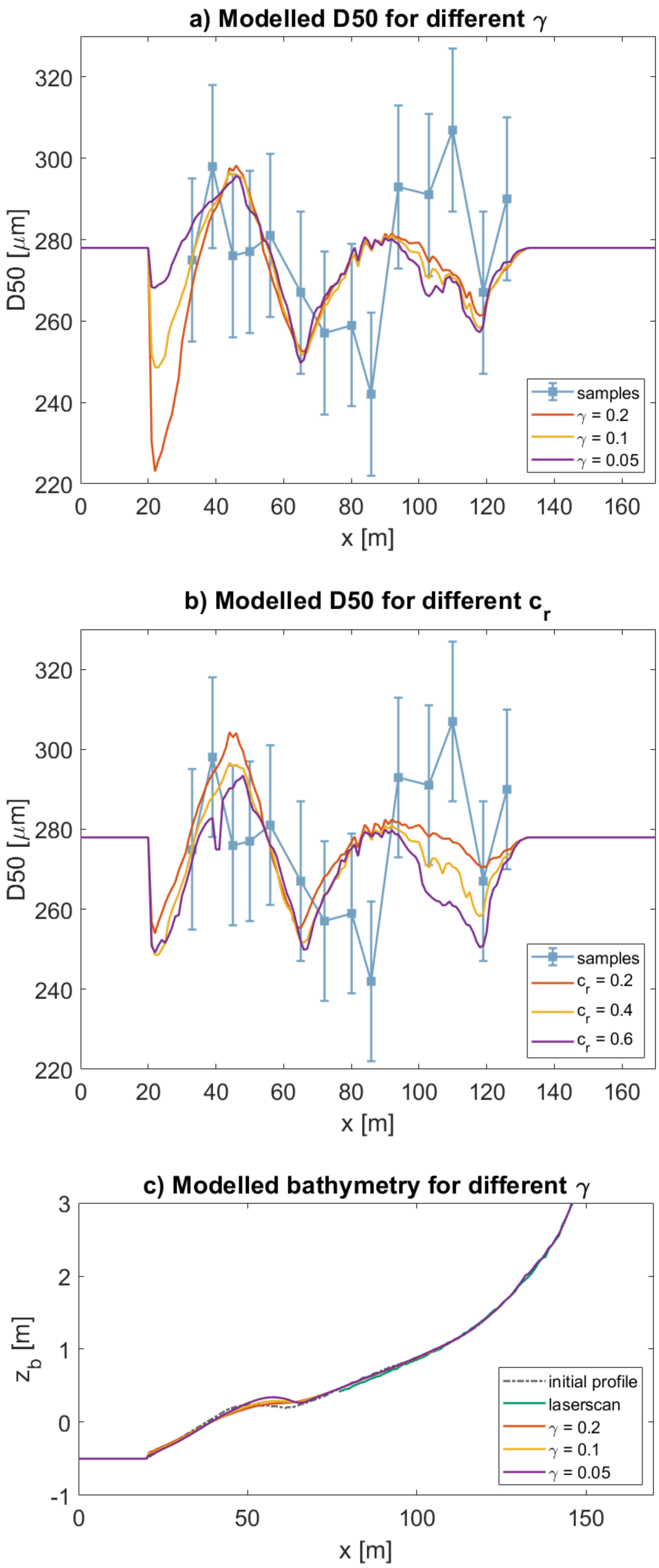

Figure 5.10: Sensitivity to suspended sediment parameters. a) D_{50} for a γ of 0.05, 0.1 and 0.2 b) D_{50} for a c_r of 0.2, 0.4 and 0.6 c) Bathymetry for a γ of 0.05, 0.1 and 0.2. Situation at the end of the model period from 29-2-2020 02:00 to 1-3-2020 02:00.

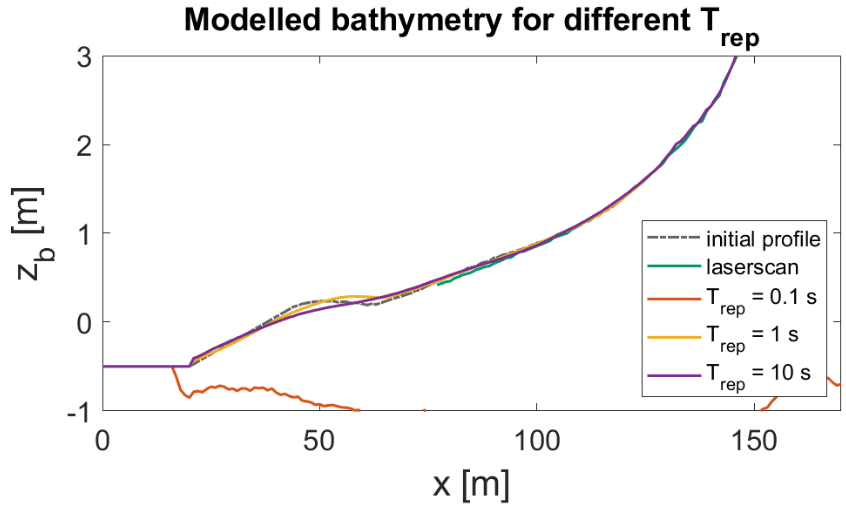

(a) Sensitivity of the bathymetry to T_{rep}. Bathymetry for a T_{rep} of 0.1, 1 and 10 seconds at the end of the model period ranging from 29-2-2020 02:00 to 1-3-2020 02:00

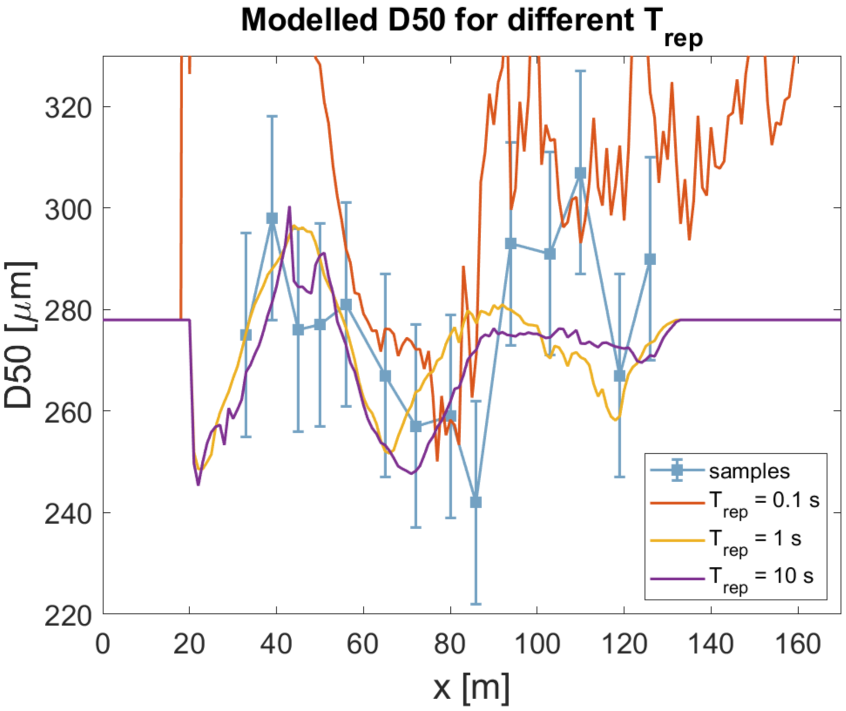

(b) Sensitivity of the D_{50} to T_{rep}. D_{50} for a T_{rep} of 0.1, 1 and 10 seconds at the end of the model period ranging from 29-2-2020 02:00 to 1-3-2020 02:00

Figure 5.11: Sensitivity to T_rep

5.4. Aeolian run

The combination of wind velocity and direction make it likely that aeolian transport has occurred. Therefore, an aeolian model run has been performed that simulates the aeolian transport in the intertidal zone.

The model results show that from t = 20 h to t = 198 h the upper part of the intertidal zone remains dry (fig. 5.2a. In this area and on the dry beach aeolian transport is possible. Therefore, a crude simulation of the aeolian transport has been performed.

The standard model run was used to reinitialize the grain size distribution at t = 198 h (on 8-3-2020 10:00). In the aeolian run the model period is completed for the remaining 50 hours. The two smallest grain size classes were removed from the top two bed layers for x > 120 m. The modelled D_{50} at t = 198 of the standard run and the initial $D_5$0 of the aeolian run are depicted in figure 5.12. On the dry beach median grain size increased from 278 to 287 μm.

The changes to the grain size distribution were introduced near the water line, which is where the largest differences in the D_{50} are found at the end of the model period (fig. 5.13b). Up until x = 105 m the cross-shore D50 is very similar to the standard run. At x = 115 m the aeolian run has a D50 of 266.6 μm which is finer than originally found. Moving further onshore the D50 follows the same pattern of local maxima and minima, but the aeolian run depicts a larger grain size. The largest difference between the aeolian and the normal runs was found at x = 124 m, with a D50 of 280.4 μm and 274.0 μm respectively.

The cross-shore variations of the D50 over the last 50 h remains fairly constant, with the areas of fine and coarse sediment remaining in position over the model period, whereas in the original run the finer sediment around x = 115 moved onshore with the rising waterline (fig. 5.13a).

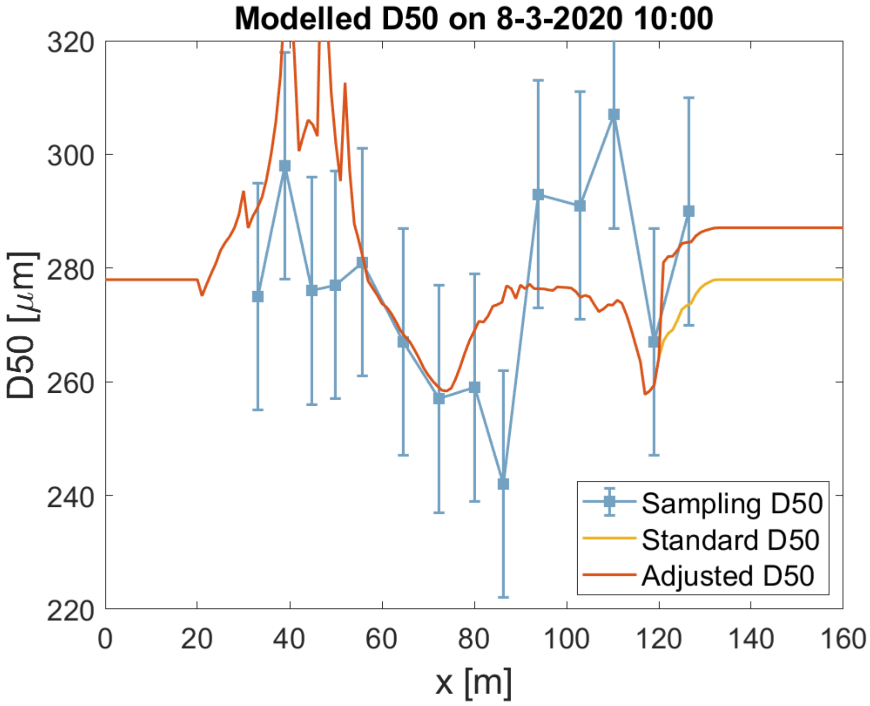

Figure 5.12: Reinitializing the grain size distribution on 8-3-2020 10:00. The yellow line is the D50 of the standard run and the red line is the D50 after reinitializing the grain size distribution for the aeolian run. The blue errorbar depicts the soil samples taken on 10-3.

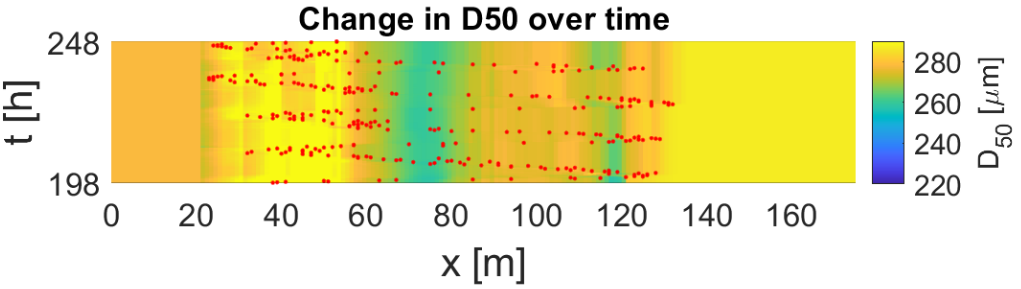

(a) Modelled D$_{50}$ over time between 8-3-2020 10:00 and 10-3-2020 13:00 after adjusting for aeolian transport and re-initializing the model run.

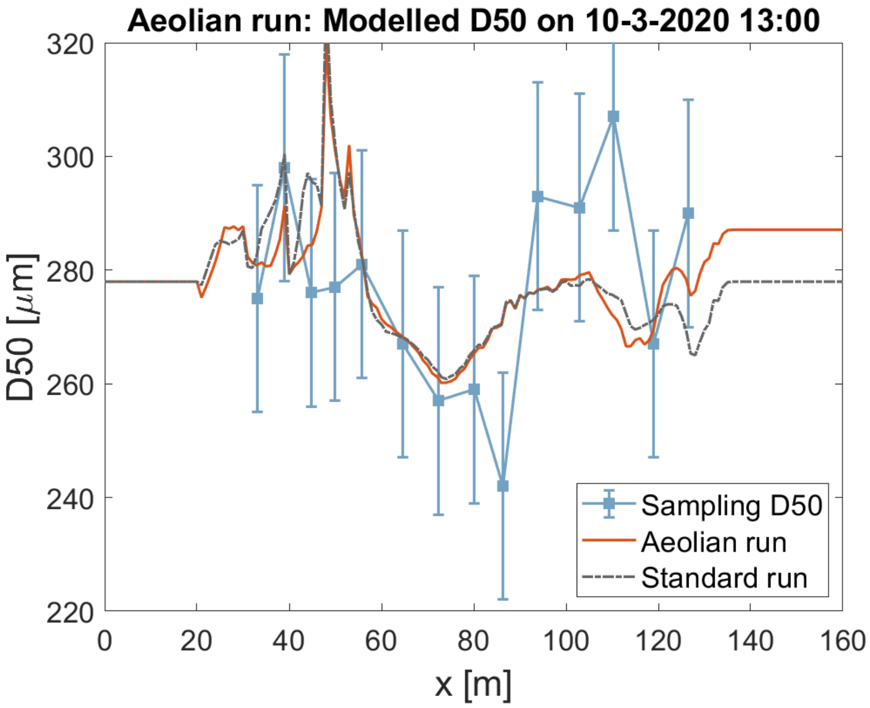

(b) Modelled cross-shore D$_{50}$ on 10-3-2020 13:00 after adjusting for aeolian transport and re-initializing the model run. The blue errorbar represent the soil samples taken on 10-3. The grey dashed line is the D50 at the end of the standard run.

Figure 5.13: Modelled D_{50} after adjusting for aeolian transport in the upper intertidal zone

6

Discussion

In the previous chapter the results of multiple model runs have been presented. In this chapter these results will be evaluated and interpreted. First, the field work data provided input and control data for this research. Uncertainties have been introduced in the field work data, which will be discussed in section 6.1. Second, three limitations of the model are discussed in section 6.2, which have resulted in differences between the model and the situation on the beach. Third, section 6.3 discusses the sensitivity of the model to different parameter settings. After the considerations about the measurements and the model the discussion continues with the interpretation of the model results. The found cross-shore variations of the morphology and the grain size are discussed in section 6.4 and compared to the laser scans and soil samples. The correlation between the morphology and the grain size is investigated in section **??**. Lastly, section 6.6 discusses the simulation of the aeolian transport and the ideas for taking into account aeolian transport.

6.1. Measurement uncertainties

The Scanex fieldwork data has been used as input of the XBeach model and as a control data set to compare the model results to. In this section two instances of uncertainties of the fieldwork data are described, the uncertainties in the soil sampling and the extra uncertainties introduced by human activity on the beach.

6.1.1. Soil sampling

The soil samples were used to determine the initial grain size distribution of the model and as a control data set for the modelled cross-shore grain size. However, the limited number of soil samples complicated the calibration and evaluation of the model.

There was one transect of soil samples available during the model period which was deliberately at the end to be able to compare the end result. As a consequence, it was not possible to discern where and under which wave conditions the modelled grain size deviated from the actual situation on the beach. When soil samples are taken on multiple days during the model period, it can aid in identifying the processes which cause problems when modelling the grain size distribution.

Furthermore, the sample D50 was based on only one realisation. The variability of the samples has been estimated based on two instances of local measurements taken on a different date and at different locations in the intertidal zone (see 3.2.3) and it is not known whether the found variability will be representative for sampling at other locations on the beach. In addition, the found variability of 20 μm was considerable. To illustrate, without the model having run at all, the $D50$ would still be within range for 11 out of 14 samples.

6.1.2. Human activity

The Noordwijk fieldwork site is a popular beach, with a beach club placed right in front of the dune foot on top of an artificial scarp. Bulldozers are employed to maintain the scarp and to remove sand that has accumulated behind the beach club under high wind conditions.

It was found that during the model scenario, bulldozers drove straight through the transect. In the laser scan point cloud of 2-3-2020 15:00 the bulldozer tracks are clearly visible (fig. 6.1). The image shows the beach when faced towards the dunes. In the top right the beach club is situated on top of an artificial berm.

The sampling transect is right where the slope is gentle enough to drive up and down the beach to reach the beach club. The tracks can be observed on the terrace, on the slope, and at the upper two sampling locations.

The bulldozers caused ground movement and mixing of the sediment, resulting in uncertainties in the cross-shore profile and soil sample measurements. It could be an explanation for the erosion and accretion found on the laser scans around x = 150 and x = 180 m (see fig. 3.15b).

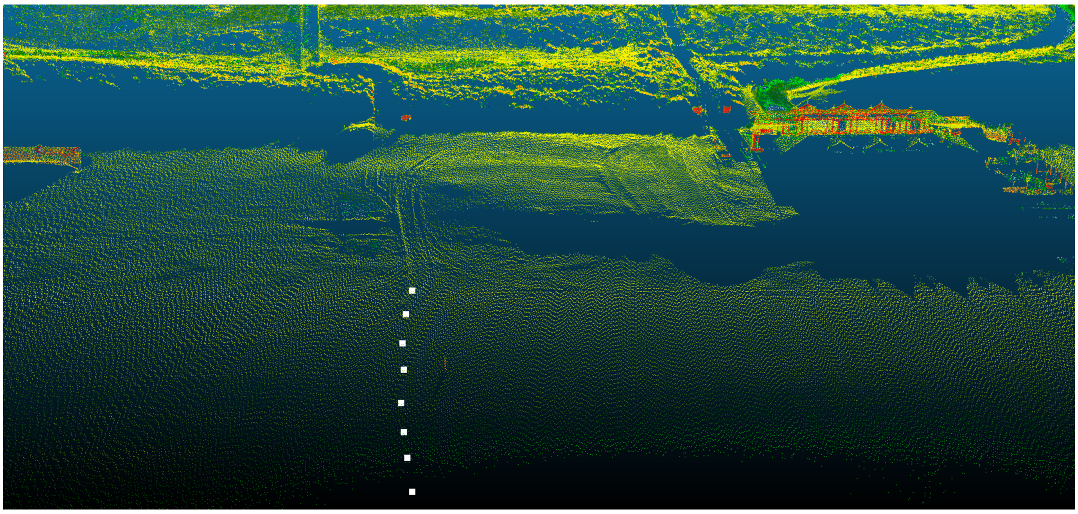

Figure 6.1: Laser scanner point cloud of 5-3-2020 18:00 showing bulldozer activity. The point cloud is faced towards the dunes. In the right of the figure the beach club can be seen. Bulldozer tracks can be observed on the berm next to the club and descending the berm at the soil sample locations (white squares).

6.2. Model limitations

In this section three limitations of the model will be elaborated upon, that have resulted in differences between the model and the situation on the beach. First, there are constraints placed on the model setup to ensure stability. Second, there is a difference between the imposed bed composition and the bed composition of the beach. Third, the 1D NLSW model does not take into account alongshore processes.

6.2.1. Model stability

The XBeach model experienced stability problems when bores approached during low water. This resulted in very high flow velocities at the boundary between fixed and free points, causing large turbulence and erosion. When more sediment is eroded than is present in the top layer the model becomes unstable (Reniers et al., 2013). Therefore, instability can be prevented by either decreasing the erosion per time step, increasing the top layer thickness or decreasing the time step. For the full description of the factors influencing model stability Appendix C can be consulted.

The model stability places constraints on the model setup. The turbulent kinetic energy had to be averaged over 1 second. For smaller averaging period the model became unstable and the beach completely eroded, as was seen in figure 5.11a. Further, a top layer of 2 cm was required to accommodate the large erosion at the fixed point boundary, which did not correspond to the 2 mm thick soil samples or the 2 mm active layer for combined aeolian and hydraulic sediment transport.

A smaller top layer would have been possible if the time step or the erosion was smaller. However, for this research the settings were chosen based on practicality. By deciding to not make any changes to the time step, the computational time was kept within reasonable limits.

6.2.2. Bed composition

The grain size distribution applied at the start of the model period is an averaged distribution based on 2 mm thick soil samples (see table 4.1). This distribution has been applied to thicker bed layers, with a top layer of 2 cm thick and underlying layers of 10 cm. This is not a correct representation of the beach, which shows a large variability in grain size in the vertical direction (C.O van IJzendoorn, personal communication, 1-4-2021). Figure 6.2 shows the variability in grain size to a depth of 44 mm of a sample taken in the intertidal zone on 20-11-2020 just after high water. The sediment in the first 10 mm shows large variations in D_{50} and is finer than in the deeper layers. The lowest D_{50} was found at 2-4 mm with a value of 245.4 μm, whereas the highest D_{50} of 351.9 μm was at 14-20 mm depth. Using only the top-layer D_{50} could either be a over- or underestimation of the underlying layers.

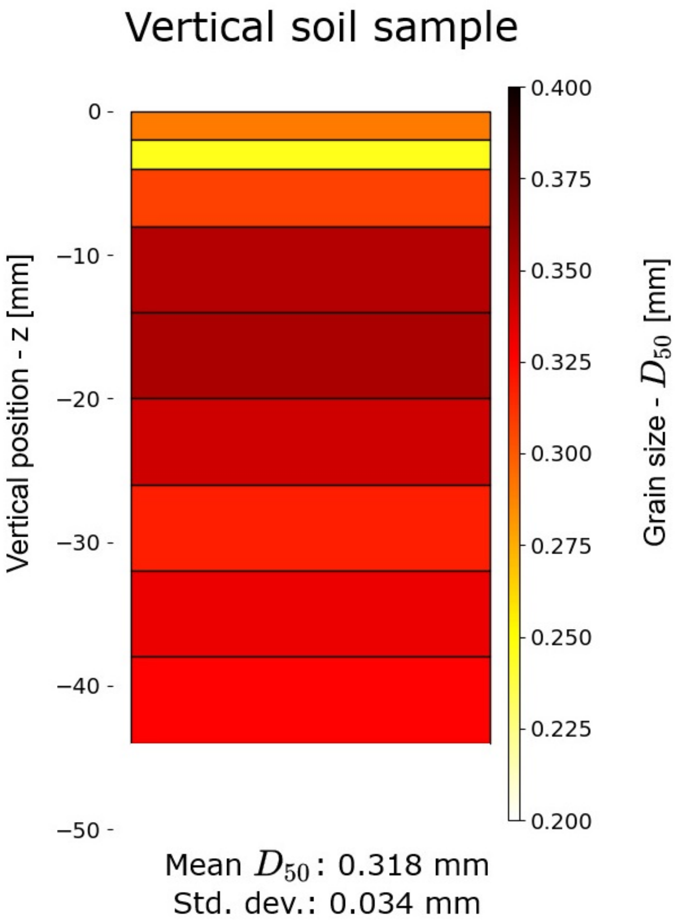

Figure 6.2: Grain size distribution over the vertical. Sample taken from the upper intertidal beach just after high water on 20-11-2020 at Noordwijk (C.O. van IJzendoorn, personal communication, 1-4-2021).

The vertical grain size distribution can contribute to grain size differences between the model and the beach. In case of erosion the layer underneath the top layer is exposed. The grain size distribution in the newly exposed layer determines whether the bed becomes coarser or finer.

If the model does not reproduce the erosion, this effect is not taken into account. Further, even if the model did show the same erosion, model differences are introduced, as the top layer will be replenished with sediment that is not representative. For instance, if the underlying sediment is finer than that would actually be present in that layer, the new top layer would have a smaller D_{50} and the transports would be overrated.

6.2.3. Alongshore processes

The XBeach 1D NLSW model only considers cross-shore processes and bathymetry. It does not take into account the effects of the intertidal bar system and the alongshore swash flow.

The emptying of the runnel could have been simulated with an outflow discharge point, but it was decided to not include this in the model setup (see section 4.1). By not including the emptying of the runnel the offshore return flows and transports over the intertidal bar will have been overestimated.

Alongshore swash flows were present during the model period, as the ADV measurements registered an, albeit small, alongshore component (see figure 3.8). These flows hinder the deposition of sediment in the upper swash zone as it prevents particles from settling during flow reversal. Consequently particles are transported offshore again during the backwash (Masselink & Puleo, 2006). Thus, by not taking into account the swash flow the model will overestimate the onshore transport of fine sediment in the upper intertidal zone.

6.3. Model sensitivity

In general the sensitivity analysis has shown that the seven investigated parameters mainly influence the morphology and grain size distribution around the sand bank. Changing the parameters can result in changing the sandbar behavior from sand bar growth to sandbar erosion. Careful calibration of the model is needed to ensure the right morphological behavior, which is required for correctly modelling the grain size distribution.

6.3.1. Calibration parameters

Three of the tested parameters are mentioned specifically as calibration parameters: c_r, c_k and γ. These parameters can be chosen freely during calibration to find the best result. At the fixed point boundary the model D_{50} was very sensitive to γ (see figure 5.10a). To prevent unrealistically large fining at the boundary a small value for γ is advised. The changes that this introduces to the morphology, can then be balanced by selecting appropriate values for c_r and c_k.

The other four parameters are less suitable for calibration. The m_{cr} and ϵ_s represent physical aspects of the hydraulic processes and as such should be chosen based on knowledge of the hydrodynamics. The choice for T_{rep} is restricted because of the model stability (see section **??**). Nevertheless, the smallest value that is still stable should be selected to keep the turbulent kinetic energy is as close to instantaneous as possible. The bed level of the ADV (d_{ADV}) determines part of the initial profile and should be based on the bathymetry. The sensitivity of the model to the bed level is further elaborated on in the following subsection.

6.3.2. Bed level at the ADV

Of the seven parameters investigated the bed-level of the ADV was found to be the most important for the grain size distribution. A considerable difference in grain size of 35 μm is found between the highest and lowest bed level and is caused by the difference in the bed slope in the lower intertidal zone.

The change in slope will affect the type of wave breaking, the moment of wave breaking, the amount of reflection and the type of wave breaking turbulence. On a lower slope waves will break further onshore. The modelled turbulence is consistent with this as for a low slope areas of high turbulence, were found 3 meter further onshore compared to the steepest slope (see figure 5.9).

Over time the effect of the initial profile will diminish, as two different profiles under the same forcing will converge to the same equilibrium profile. However, since the first twenty points of the bathymetry remained fixed, the profile differences have persisted in the lower intertidal zone.

The sensitivity of the model grain size to the depth at the ADV brought to light the importance of knowing the underwater bathymetry. As the laser scanner is not able to measure under water or on wet sand, the underwater bathymetry was reconstructed based on measurements of the d_{ADV}. The ADV was positioned in a very morphodynamically active region, while the bed level has only been measured once after installation and one month later after repositioning. In this interval the bed level had risen 0.33 m. As the d_{ADV} at the start of the model period could not be determined, the model was calibrated for it.

The model can be improved by measuring the underwater bathymetry, eliminating the need for calibration of the d_{ADV} and removing the uncertainty of a reconstructed underwater profile. The most straightforward method is using a GPS system on a large measuring pole during low water to fill in the gaps in the laser scan profile. In order to be flexible in determining the model period, the GPS transect should be taken regularly during a fieldwork campaign.

6.4. Cross-shore variations in morphology and grain size

The model was calibrated based on the idea that the morphology needs to be modelled correctly for the grain size distribution to be modelled correctly as well, since the changes in morphology are a direct result of the changes of the sediment transports per grain size class.

It was found that the XBeach model has an overactive morphological response. This is probably caused by the large computed velocities at the fixed point boundary that also led to the stability problems (see section **??**). These velocities generate large transports without updating the bed level and composition. Compared to the laser scans, the model has transported more sediment from the sand bar onshore (fig. 6.3). Between x = 20 and x = 50 the bed level of the model is on average 0.12 m lower than the scans and between x = 50 m and x = 80 m the model bed level is 0.11 m higher than the scans. In the middle of the intertidal zone from x = 80 m to x = 110 m the model has not deviated much from the initial profile, while in the laser scans erosion of the beach is observed. The differences between the model and the laser scan are approximately 4 cm. As the laser scan shows erosion, where the model does not, the vertical grain size distribution will have contributed to changes in the modelled grain size (see section **??**).

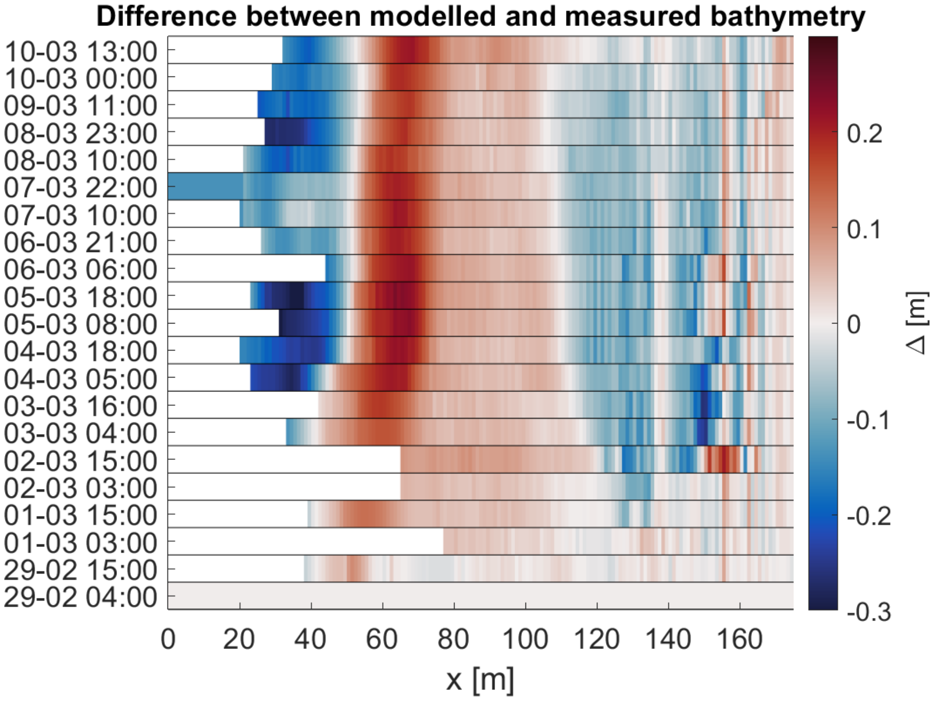

Figure 6.3: Difference between the measured laser scan bathymetry and the modelled bathymetry of the standard run during low water. A positive value corresponds to a modelled bed level higher than the laser scan bed level.

The cross-shore median grain size at the end of the standard model run is compared to the soil samples (see figure 5.1a). The mean absolute difference is 15.6 μm Compared to the variations found in the cross-shore, this seems a large difference. However, the uncertainties in the measurements complicate a direct quantitative comparison between the model result and the soil samples. Nevertheless, it can be observed that the modelled cross-shore variation of the D_{50} follows the same trend as the soil samples. Both show an increase in grain size in the lower intertidal zone, a decrease in grain size in the middle intertidal zone and an increasing grain size in the upper tidal zone. The differences are in the magnitude of the grain size variations. In the lower intertidal zone the model has coarser sediment with a large peak of 329 μm. In the middle intertidal zone the model follows the soil samples at first, but at x = 74 the model grain size starts to rise again, while the sample grain size continues to decrease. In the upper intertidal zone the model underestimates the grain size, as it remains around the initial grain size, whereas the soil samples show coarser sediment of approximately 300 μm. Both the alongshore swash flows and aeolian transport (see section **??** and 6.6 respectively) could have contributed to the underestimation of the grain size in the upper intertidal zone.

6.4.1. Intra-/intertidal variations

The grain size is coarser when the beach is submerged compared to when the beach is emerged, except for the fine sediment that is found at the water line during submersion (see fig. 5.2b). Under water the finer sediment will be brought into suspension leaving the coarser sediment. As the tide rises fine sediment is transported high up the beach, leaving behind coarser sediment. The falling tide brings finer sediment back to original location, apart from fines that remain near the high water line due to scour lag.

On a longer timescale the contribution of these intratidal variations is small. In the five-day run it can still be seen that fines are deposited at the waterline (see fig. 5.4b). For each higher high water the fines also moved further onshore. However, this effect is cannot be discerned in the original model run (see fig. 5.2a). The original model run started with storm conditions just after high water spring. The grain size variations that were established over the cross-shore did not change until the high water spring at the end of the model period. The effect of a single tide in depositing fines around the waterline, did not significantly change the grain size. This leads to the hypothesis that not a single tide but the highest water levels are governing for the cross-shore D50 on the beach. The impact of a storm in this respect is that the highest water levels can be caused by storm set-up. As a consequence the supply of fine sediment for aeolian transport would also be governed by the water level.

Using the storm at the start of the model period greatly reduced the spin up time of the model as a constant cross-shore grain size variation was reached after 15 hours in stead of 75 hours in the 5-day run without a storm. This can be a good way to quickly establish the actual grain size distribution on the beach based on the averaged bed composition. The standard run showed a better result for the cross-shore D_{50}. The inclusion of a storm introduces more mixing of the initial grain size distribution. This improves the result during erosion, as the mixed sediment is exposed in stead of the initial sediment.

6.5. Correlation between morphology and grain size

A correct modelled morphology implies that the total sediment transports have been modelled correctly. This in turn implies that the transports for individual sediment classes, the changes to the amount of sediment in each class and the grain size distribution have been modelled correctly. Hence, the assumption that a correctly modelled morphology results in a correctly modelled grain size. If the assumption is valid, a relation exists between the morphology and the grain size distribution, which is investigated in this section as it might be used to develop a method to predict the grain size on the beach. This could provide an alternative to the time consuming soil sampling.

The model shows a strong negative correlation between the change in bathymetry over time and the change in grain size over time with respect to the initial model settings, such that $\Delta z_b = z_b - z_{b,0}$ and $\Delta D_{50} = D_{50} - D_{50,0}$. For twenty low waters the correlation between the change in bed level and the change in $D50$ has been computed (see the example in figure 6.4a). A mean correlation coefficient of $r = -0.767$ was found.

A similar correlation was not found in the field work data. Computing the correlation between the bed level change and the D_{50} based on the soil samples and the laser scan data resulted in a correlation coefficient of $r = -0.099$ (fig. 6.4b). However, the correlation of the control data includes large uncertainties because of the local variability of the soil samples (see 6.1) and the limited number of 14 data points.

To further explore whether the modelled correlation can be found on the beach, more research is required. On at least two different days soil samples should be taken along a transect and the bed level measured at each sampling location. The required number of sampling locations for computing the correlation can be determined beforehand using for instance Bonett and Wright (2000) (2000). To decrease the uncertainty of local variations in the soil sampling, more than one sample should be taken per sampling location and the averaged D_{50} should be used.

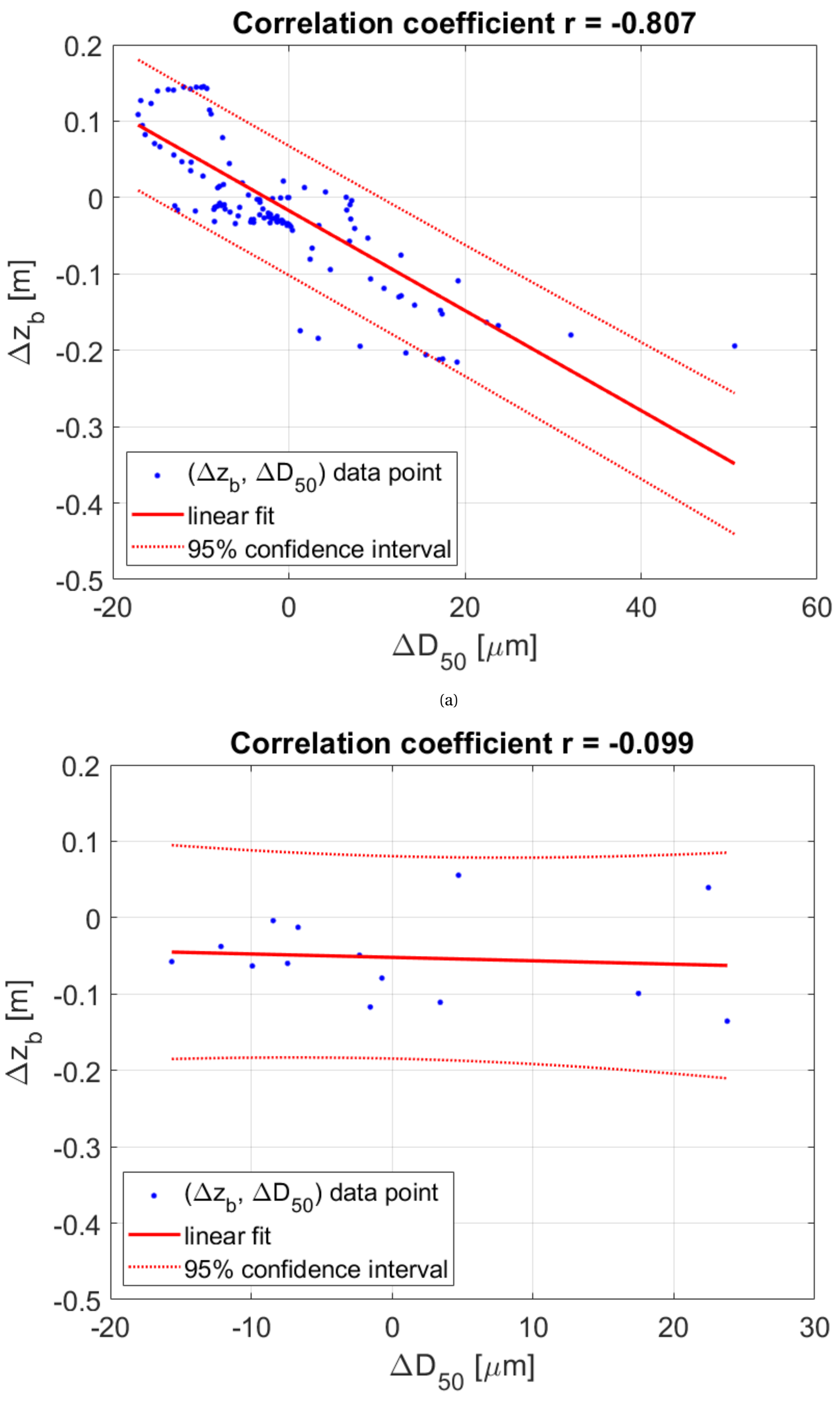

(a)

(b)

Figure 6.4: Correlation between the modelled (a) and measured (b) change in bed level and the change in grain size with respect to the initial values: $\Delta z_b = z_b = z_{b,0}$, $\Delta D_{50} = D_{50} = D_{50,0}$. The dashed lines show the 95% confidence interval. Both correlations are computed for the situation at 10-3-2020 13:00

6.6. Simulating aeolian transport

The original model run shows an underestimation of the grain size near the water line. A possible explanation was sought in the fact that aeolian transport is not included in the XBeach model, while the combination of wind velocities and wind direction show that aeolian transport from the beach towards the dunes has likely occurred. As aeolian transport will mostly affect the smallest grain sizes, this effect was simulated by removing the two smallest sediment classes from the grain size distribution right before the upper intertidal zone would be submerged by the approaching spring tide.

The aeolian model run has improved the result near the water line. Although the differences in grain size between the aeolian and original run were small, the aeolian run has local minima and maxima that are more in line with the soil samples. The aeolian run still underestimates the grain size in the upper intertidal zone, so it is possible that other underlying processes are also contributing to this.

The D_{50} on the dry beach is a better match with the last soil sample in the intertidal zone. It is in line with the expectation that including the aeolian transport will better represent the grain size distribution on the dry beach. However, as the water level does not reach the last sampling location, the D_{50} is still the initial grain size.

The aeolian run is a very crude simulation in time as well as space. Aeolian transport does not cause such an abrupt change in grain size as was imposed in the aeolian model run, but is a continuous process with a gradual effect over time. All emerged parts of the beach will be under the influence of the wind, not just the upper intertidal zone and dry beach. The effect of aeolian transport will gradually diminish in the offshore direction as the beach is emerged for shorter periods of time.

The aeolian transports are relatively small compared to the hydraulic transports. On short timescales the influence of aeolian transport may not be apparent. However, over a spring-neap cycle parts of the upper intertidal zone remain dry for days, allowing the aeolian sediment transports to add up.

The cross-shore variations of the grain size in the top layer determine where sediment is available for transport, as finer sediments are more easily picked up by the wind. The deposition of fine sediment near the waterline and the long exposure to the wind make the upper intertidal zone the primary source of sediment in the intertidal zone.

To completely include the effect aeolian transport the XBeach model should be coupled to an aeolian transport model. With the coupling sediment transports and morphology can be computed for entire transect from the sea towards the dunes. The aeolian model adjusts the grain size distribution over the entire length of the transect, providing better input for the hydraulic model, whereas the cross-shore variations caused by the hydraulic model provide information on the sediment available for aeolian transport.

Coupling with an aeolian transport model comes with difficulties. First, the top layer of the XBeach model (2 cm) does not correspond to the active layer of the combined aeolian and hydraulic sediment transport (2 mm) due to model instability. If in a coupled model the used top layer is too thick, grain size changes in the active layer get lost. Instead, the choice can be made to set the top layer of XBeach to 2 mm and accept the model instabilities. The instabilities occur at the offshore side near the fixed point boundary, where the effect of aeolian transport will be minimal. As long as the instabilities do not extent to the upper intertidal zone, which is the region of interest for aeolian transport, this will not cause a problem.

Second, more attention needs to be paid to the ground water modelling, as moisture content of the soil will influence the sediment availability for aeolian transport. In the XBeach model standard groundwater model settings were used, but in a coupled model it is advised to determine the right parameter settings for the region of interest.

Running an hydraulic and an aeolian model for the same model period will greatly increase computational effort. Whether this is worthwhile depends on the considered timescale. The cross-shore grain size does not show large variation over a model period of eleven days and the effect a the single tide does not stand out. This implies that the location of fine sediments, and thus the aeolian sediment supply, in this model scenario is controlled on the spring-neap tidal time scale or storm time scale and not on the time scale of a single tide. Nevertheless, it should be considered that aeolian transport has not been taken into account yet. In the upper intertidal zone the fine sediment could have been removed and an armor layer could have formed. In that case, the supply of fine sediment near the water line on the scale of a single tide could be more important than is visible in the results.

7

Conclusions

This thesis set out to investigate the influence of marine processes on the the cross shore grain size variation in the top layer of the intertidal zone based on five research questions. In this chapter an answer is given to the research questions and concrete recommendations for improvements and further research are made.

- What are the dominant processes for modelling the cross-shore grain size distribution on the beach? The grain size distribution and the sediment transports influence each other. On one hand the grain size distribution is a direct result of the sediment transports. On the other hand, since the entrainment and settling of an individual sediment particle is dependent on the grain size, the sediment transports are dependent on the grain size as well.

  Cross-shore sediment transport can be seen as sediment that is stirred from the bed and moved along by the cross-shore flows. Turbulence is responsible for stirring sediment from the bed and keeping sediment in suspension. Also, turbulence keeps sediment particles in suspension. In the surf zone the breaking induced turbulence is the most important source of turbulence. In the swash zone most turbulence is generated when bores collapse at the start of the uprush. In modelling of the grain size the importance of turbulence shows in the turbulence model that is added to the NLSW equations and the many calibration and set up parameters that are related to it.

- How do marine processes change the grain size distribution of the top layer on a intra-tidal timescale?

  Over a single tide fine sediment is deposited near the water line. Within one tidal cycle sand becomes coarser when the intertidal zone submerges and finer once it emerges. The net effect over a single tide is small. Fine sediments are deposited near the water line. When a high water is higher than previous high waters, the fines are migrated onshore.

  Under storm conditions a thicker layer of sediment is stirred up. This determines the bed composition during erosion, as it exposes the sediment underneath the top layer.

- How do marine processes change the grain size distribution of the top layer on a inter-tidal timescale?

  The cross-shore grain size is governed by the highest high waters and remained fairly constant over a period of 11 days. At the start of the model period the high water set the grain size distribution on the transect and the variations over a single tide are negligible. Only as spring tide approaches, does the water line exceed the one at the start and is a new cross-shore pattern established. Based on this it is hypothesized that either the high high water spring or the storm set-up, is governing for the cross-shore grain size variations on the beach.

  Under storm conditions a thicker layer of sediment is stirred up. This influences the bed composition during erosion in later tidal cycles, as it exposes the sediment underneath the top layer.

- What are the implications of the grain size variations in the intertidal zone for aeolian transport?

  Aeolian transport will lead to a coarser sediment in the intertidal zone. The lower in the intertidal zone, the less the aeolian influence will be. In the upper intertidal zone the beach is emerged for longer periods of time and aeolian transport can have a significant contribution to the grain size.

The cross-shore variations of the grain size in the top layer determines where sediment is available for aeolian transport. It is likely that during the model period the deposition of fine sediment near the high water line was the primary supply of sediment from the intertidal zone. As the cross-shore grain size does not show much variation over a period of 11 days and the effect on the grain size over a single tide does not stand out, it implies that the largest aeolian sediment supply in this model scenario was mainly controlled on the spring-neap tidal time scale or storm scale and not on the time scale of a single tide. Nevertheless, when considering that coarsening of the sediment and possible formation of an armor layer due to aeolian transport could have occurred in the upper intertidal zone, the supply of fine sediment near the water line on the scale of a single tide could be more important than is visible in the results.

- To what extent is the XBeach 1D-NLSW model suitable for predicting the development of the grain size diameter in the field?

  The XBeach 1D non linear shallow water model is able to model the cross-shore grain size in the intertidal zone. It does experience difficulties in modelling the erosion and the fine sand in the middle intertidal zone and underestimates the grain size in the upper intertidal zone. There were uncertainties in the soil sampling measurements as well as the model. Still, the model reproduced the trend of the cross-shore grain size on the beach showing a similar pattern of increasing and decreasing grain size over the transect.

  The model stability restricted the top layer to a thickness to 2 cm, while the active layer for combined aeolian en hydraulic transport is 2 mm. Instability occurs when the erosion is larger than the thickness of the top layer over a single timestep. If the top layer is chosen too small, a smaller time step is required and the model becomes computationally too expensive.

  The XBeach model is very sensitive to the underwater bathymetry at the offshore edge of the model, causing large grain size variations in the lower intertidal zone. Better input for the underwater bathymetry is required.

7.1. Recommendations

Underwater bathymetry
The sensitivity of the model to the d_{ADV} showed the importance of knowing the underwater bathymetry. The model result could be improved by taking GPS measurements of the underwater bathymetry to fill in the gaps of the laser scanner in the cross-shore profile. As the underwater bathymetry in the intertidal zone is highly dynamic, it is desirable to take measurements every few days in order to be flexible in selecting the model period.

Soil sampling control data
During the model period one transect of soil samples was taken. As a consequence, it was not possible to determine when and under which conditions the model D_{50} had deviated from the situation on the beach. In future research it will be helpful to have multiple sampling transects available over the model period.

Initial bed compostion
The initial bed composition for all the layers in the XBeach model were based on the average grain size distribution of 2 mm samples, which is not representative for the vertical grain size distribution found on the beach. As the model seems to have redistributed initial sediment reasonably well over the intertidal zone, it can be tested whether thicker soil samples in combination with high energetic conditions can be used to improve the bed composition over the vertical.

Correlation
To further investigate the correlation between the change in morphology and the change in grain size a soil sampling study can be performed. First, the number of sample locations needed for the correlation should be determined. Then, on two different days, samples should be taken at the sample locations. As stated above, multiple samples can be taken per location to reduce the measurement uncertainty. At each location the bed level is measured as well, with for instance a GPS. Based on the soil samples and GPS measurements the

change in morphology and D_{50} can be computed and the correlation can be determined.

Aeolian transport
The aeolian transport was not taken into account in XBeach and the aeolian run was a crude simulation. An aeolian transport model can be used to further research the effect of aeolian transport on the cross-shore grain size in the intertidal zone. This will provide a better understanding of the relative importance of marine and aeolian transport on the grain size distribution. A further step would be to integrate the marine and aeolian transport processes into a coupled XBeach/aeolian transport model. When considering a coupled model, special attention should be given to specifying the top layer and the groundwater modelling. The top layer thickness should be thin enough to notice changes caused by aeolian transport, but this could result in instability of the XBeach model. In a coupled model the influence of moisture content on the aeolian sediment availability, increases the importance of groundwater modelling. In stead of the default settings that were used in this research it is recommended to determine the right parameter settings for the groundwater modelling.

References

Bagnold, R. A. (1941). *The physics of blown sand and desert dunes,.* London: Methuen & Co.

Bertin, X., de Bakker, A., van Dongeren, A., Coco, G., André, G., Ardhuin, F., … Tissier, M. (2018, February). Infragravity waves: From driving mechanisms to impacts. *Earth-Science Reviews*, *177*, 774–799. Retrieved 2020-06-02, from `http://www.sciencedirect.com/science/article/pii/S0012825217303239` doi: 10.1016/j.earscirev.2018.01.002

Boers, M. (2005). *Surf zone turbulence.* Retrieved 2021-10-24, from `http://resolver.tudelft.nl/uuid:71428ad5-0658-49f7-b83e-0deb26b668cf`

Bonett, D., & Wright, T. (2000, 02). Sample size requirements for estimating pearson, kendall and spearman correlations. *Psychometrika*, *65*, 23-28. doi: 10.1007/BF02294183

Bosboom, J., & Stive, M. (2015). *Coastal dynamics i lecture notes cie 4305.* Delft Academic Press.

Bujan, N., Cox, R., & Masselink, G. (2019, November). From fine sand to boulders: Examining the relationship between beach-face slope and sediment size. *Marine Geology*, *417*, 106012. Retrieved 2021-10-24, from `https://www.sciencedirect.com/science/article/pii/S0025322718304365` doi: 10.1016/j.margeo.2019.106012

Christensen, D. F., Brinkkemper, J., Ruessink, G., & Aagaard, T. (2018, November). Field observations of turbulence in the intertidal and shallow subtidal zones. *Continental Shelf Research*, *170*, 21–32. Retrieved 2021-02-23, from `https://www.sciencedirect.com/science/article/pii/S027843431830147X` doi: 10.1016/j.csr.2018.10.002

Christensen, D. F., Hughes, M. G., & Aagaard, T. (2019). Wave Period and Grain Size Controls on Short-Wave Suspended Sediment Transport Under Shoaling and Breaking Waves. *Journal of Geophysical Research: Earth Surface*, *124*(12), 3124–3142. Retrieved 2020-05-27, from `https://agupubs.onlinelibrary.wiley.com/doi/abs/10.1029/2019JF005168` (_eprint: https://agupubs.onlinelibrary.wiley.com/doi/pdf/10.1029/2019JF005168) doi: 10.1029/2019JF005168

Cohn, N., Ruggiero, P., de Vries, S., & Kaminsky, G. M. (2018). New Insights on Coastal Foredune Growth: The Relative Contributions of Marine and Aeolian Processes. *Geophysical Research Letters*, *45*(10), 4965–4973. Retrieved from `https://agupubs.onlinelibrary.wiley.com/doi/abs/10.1029/2018GL077836` doi: 10.1029/2018GL077836

Davidson-Arnott, R. G. D., MacQuarrie, K., & Aagaard, T. (2005). The effect of wind gusts, moisture content and fetch length on sand transport on a beach. *Geomorphology*, *68*(1), 115 – 129. Retrieved from `http://www.sciencedirect.com/science/article/pii/S0169555X04002922` doi: https://doi.org/10.1016/j.geomorph.2004.04.008

de Vriend, H. J., van Koningsveld, M., Aarninkhof, S. G. J., de Vries, M. B., & Baptist, M. J. (2015, June). Sustainable hydraulic engineering through building with nature. *Journal of Hydro-environment Research*, *9*(2), 159–171. Retrieved 2020-05-28, from `http://www.sciencedirect.com/science/article/pii/S1570644314000653` doi: 10.1016/j.jher.2014.06.004

De Vries, S., Harley, M. D., De Schipper, M. A., & Ruessink, G. (2015, July). Dune growth due to aeolian sediment transport and the role of the beach and intertidal zone. In *The Proceedings of the Coastal Sediments 2015.* San Diego, USA: WORLD SCIENTIFIC. Retrieved 2020-02-12, from `http://www.worldscientific.com/doi/abs/10.1142/9789814689977_0043` doi: 10.1142/9789814689977_0043

De Vries, S., Stive, M. J. F., Van Rijn, L., & Ranasinghe, R. (2012). A new conceptual model for aeolian transport rates on beaches. *ICCE 2012: Proceedings of the 33rd International Conference on Coastal Engineering, Santander, Spain, 1-6 July 2012.* Retrieved 2020-02-17, from `https://repository.tudelft.nl/islandora/object/uuid%3Acdf83719-5f36-42c8-afbe-6a4be4e3f19e`

Gatto, V. M., van Prooijen, B. C., & Wang, Z. B. (2017). Net sediment transport in tidal basins: quantifying the tidal barotropic mechanisms in a unified framework. *Ocean Dynamics*, *67*(11), 1385–1406.

GoogleEarth. (n.d.). *[combined google earth images of the netherlands and noordwijk]*.

Guza, R., Thornton, E., & Holman, R. (1985). Swash on Steep and Shallow Beaches. In (pp. 708–723). doi: 10.1061/9780872624382.049

Holthuijsen, L. H. (2007). Linear wave theory (oceanic waters). In *Waves in oceanic and coastal waters* (p. 106–144). Cambridge University Press. doi: 10.1017/CBO9780511618536.006

Hoonhout, B., & de Vries, S. (2017, February). Field measurements on spatial variations in aeolian sediment availability at the Sand Motor mega nourishment. *Aeolian Research*, *24*, 93–104. Retrieved 2020-05-27, from `http://www.sciencedirect.com/science/article/pii/S1875963716301264` doi: 10.1016/j.aeolia.2016.12.003

Masselink, G., & Puleo, J. A. (2006, April). Swash-zone morphodynamics. *Continental Shelf Research*, *26*(5), 661–680. Retrieved 2020-02-18, from `https://linkinghub.elsevier.com/retrieve/pii/S0278434306000318` doi: 10.1016/j.csr.2006.01.015

McKenna Neuman, C., Li, B., & Nash, D. (2012). Micro-topographic analysis of shell pavements formed by aeolian transport in a wind tunnel simulation. *Journal of Geophysical Research: Earth Surface*, *117*(F4). Retrieved from `https://agupubs.onlinelibrary.wiley.com/doi/abs/10.1029/2012JF002381` doi: 10.1029/2012JF002381

Nortek. (2018). *The comprehensive manual for velocimeters* [Manual]. Retrieved 2020-07-20, from `https://support.nortekgroup.com/hc/en-us/articles/360029839351-The-Comprehensive-Manual-Velocimeters`

Reniers, A., Gallagher, E., Macmahan, J., Brown, J., van Rooijen, A., Thiel de Vries, J., & Prooijen, B. (2013, 02). Observations and modeling of steep-beach grain-size variability. *Journal of Geophysical Research: Oceans*, *118*, 577-591. doi: 10.1029/2012JC008073

Sarre, R. D. (1989). Aeolian sand drift from the intertidal zone on a temperate beach: Potential and actual rates. *Earth Surface Processes and Landforms*, *14*(3), 247–258. Retrieved 2020-05-11, from `https://onlinelibrary.wiley.com/doi/abs/10.1002/esp.3290140306` (_eprint: https://onlinelibrary.wiley.com/doi/pdf/10.1002/esp.3290140306) doi: 10.1002/esp.3290140306

Schiereck, H., G.J.and Verhagen. (2016). *Introduction to bed, bank and shore protection.* Delft Academic Press.

Shakoor, A. (2018). Characterization of Soils. In P. T. Bobrowsky & B. Marker (Eds.), *Encyclopedia of Engineering Geology* (pp. 108–114). Cham: Springer International Publishing. Retrieved from `https://doi.org/10.1007/978-3-319-73568-9_48` doi: 10.1007/978-3-319-73568-9_48

Terwindt, J. H. J. (1962). Onderzoek korrelgrootte-variaties voor de kust van Katwijk 1962. *RWS report-324.* Retrieved 2021-02-15, from `https://repository.tudelft.nl/islandora/object/uuid%3Ac6882743-ed21-4f2e-8440-7575fc1345c1` (Publisher: Rijkswaterstaat)

Ting, F. C. K., & Kirby, J. T. (1995, March). Dynamics of surf-zone turbulence in a strong plunging breaker. *Coastal Engineering*, *24*(3), 177–204. Retrieved 2021-10-24, from `https://www.sciencedirect.com/science/article/pii/037838399400036W` doi: 10.1016/0378-3839(94)00036-W

Ting, F. C. K., & Kirby, J. T. (1996, July). Dynamics of surf-zone turbulence in a spilling breaker. *Coastal Engineering*, *27*(3), 131–160. Retrieved 2021-10-24, from `https://www.sciencedirect.com/science/article/pii/0378383995000372` doi: 10.1016/0378-3839(95)00037-2

Van der Spek, A., & Lodder, Q. (2015, 07). A new sediment budget for the netherlands; the effects of 15 years of nourishing (1991-2005).. doi: 10.1142/9789814689977_0074

Van der Zwaag, J. (2014). *Modelling sediment sorting near the large scale nourishment 'the sand motor': Understanding cause and impact of sediment sorting processes.* Retrieved 2020-12-29, from `https://repository.tudelft.nl/islandora/object/uuid%3A328250df-6038-4582-97d8-e7ba743e0761`

Van Rijn, L. (1997). *Cross-shore modelling of graded sediments* (Report No. z2181). Delft, The Netherlands: Delft Hydraulics.

Van Rijn, L. (2019, 07 05). *Aeolian transport over a flat sediment surface.* `leovanrijn-sediment.com`. (accessed on 2020-03-23)

Verruijt, A. (2002). *Grondmechanica.* Delft University of Technology.

Vos, S. E., Lindenbergh, R. C., & de Vries, S. (2017). Coastscan: Continuous monitoring of coastal change using terrestrial laser scanning. *Proceedings of Coastal Dynamics 2017*. Retrieved 2020-02-06, from `https://repository.tudelft.nl/islandora/object/uuid%3Aefc89a17-564d-4074-a83c-7dee975313c5`

Wiggs, G., Baird, A., & Atherton, R. (2004, April). The dynamic effects of moisture on the entrainment and transport of sand by wind. *Geomorphology*, *59*(1-4), 13–30. Retrieved 2020-05-19, from `https://linkinghub.elsevier.com/retrieve/pii/S0169555X03003106` doi: 10.1016/j.geomorph.2003.09.002

XBeachDocs. (2020). *Welcome to xbeach's documentation.* (documentation version v:latest)

A

Appendix A Sample grain size distributions

In this Appendix the grain size distribution the results of the sieve tower analysis is shown for each soil sample taken along the transect. Sampling and sieving has been performed by Christa van IJzendoorn. Fractions do not always round up to 1 due to rounding errors and differences between the measured dry weight and the total mass retrieved from the sieves.

Table A.1: Grain size distribution at sample location 1

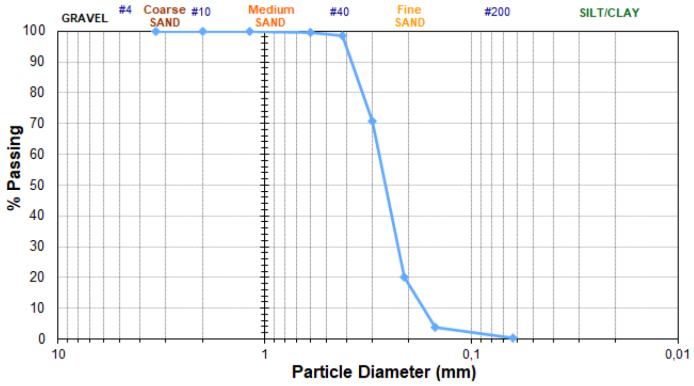

D_{50} **[mm]**		0.275	
Range [mm]	**Mass [g]**	**Soil retained [%]**	**Soil passing [%]**
> 3.5	0.0	0.0	100.0
2.0 - 3.35	0.0	0.0	100.0
1.18 -2.0	0.2	0.1	99.8
0.6 - 1.18	0.6	0.4	99.5
0.42 - 0.6	1.4	0.9	98.6
0.3 - 0.42	42.6	27.8	70.8
0.212 - 0.3	78.0	50.8	20.0
0.15 - 0.212	24.9	16.2	3.8
0.063 - 0.15	5.3	3.5	0.4
< 0.063	0.1	0.0	0.3
Total	153.1	99.7	

Table A.2: Grain size distribution at sample location 2

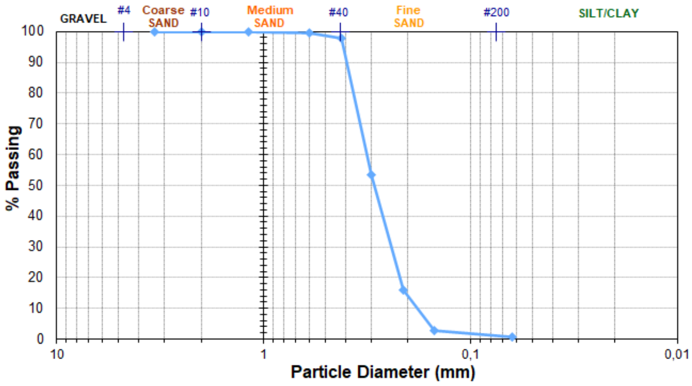

D_{50} [mm]		0.298	
Range [mm]	**Mass [g]**	**Soil retained [%]**	**Soil passing [%]**
> 3.5	0.0	0.0	100.0
2.0 - 3.35	0.0	0.0	100.0
1.18 -2.0	0.3	0.2	99.8
0.6 - 1.18	0.6	0.4	99.4
0.42 - 0.6	2.9	1.7	97.7
0.3 - 0.42	74.5	44.2	53.6
0.212 - 0.3	63.6	37.7	15.9
0.15 - 0.212	22.1	13.1	2.7
0.063 - 0.15	3.7	2.2	0.6
< 0.063	0.1	0.0	0.5
Total	167.7	99.5	

Table A.3: Grain size distribution at sample location 3

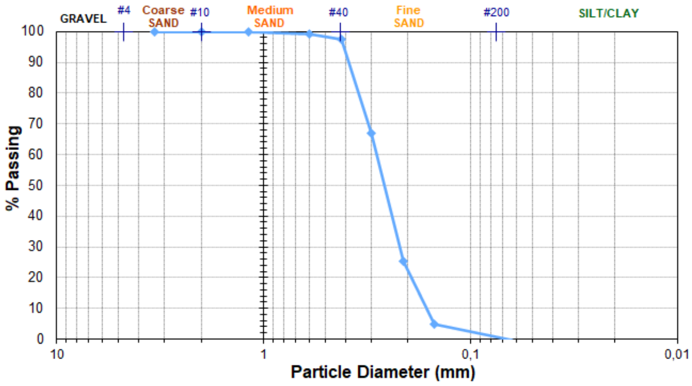

D_{50} [mm]		0.276	
Range [mm]	**Mass [g]**	**Soil retained [%]**	**Soil passing [%]**
> 3.5	0.0	0.0	100.0
2.0 - 3.35	0.0	0.0	100.0
1.18 -2.0	0.2	0.1	99.9
0.6 - 1.18	1.3	0.8	99.1
0.42 - 0.6	2.7	1.7	97.4
0.3 - 0.42	47.4	30.4	67.0
0.212 - 0.3	65.0	41.7	25.3
0.15 - 0.212	31.6	20.3	5.0
0.063 - 0.15	8.1	5.2	-0.2
< 0.063	0.1	0.0	-0.3
Total	156.3	100.3	

Table A.4: Grain size distribution at sample location 4

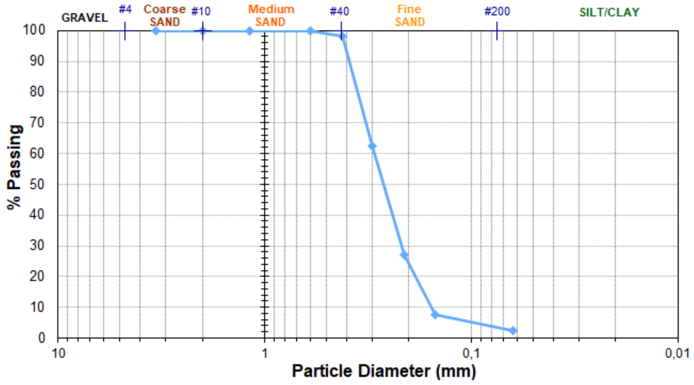

D_{50} **[mm]**		0.277	
Range [mm]	**Mass [g]**	**Soil retained [%]**	**Soil passing [%]**
> 3.5	0.0	0.0	100.0
2.0 - 3.35	0.0	0.0	100.0
1.18 -2.0	0.1	0.1	99.9
0.6 - 1.18	0.1	0.1	99.9
0.42 - 0.6	2.6	1.6	98.2
0.3 - 0.42	56.6	35.9	62.3
0.212 - 0.3	55.5	35.2	27.1
0.15 - 0.212	30.9	19.6	7.5
0.063 - 0.15	8.3	5.3	2.3
< 0.063	0.1	0.1	2.2
Total	154.1	97.8	

Table A.5: Grain size distribution at sample location 5

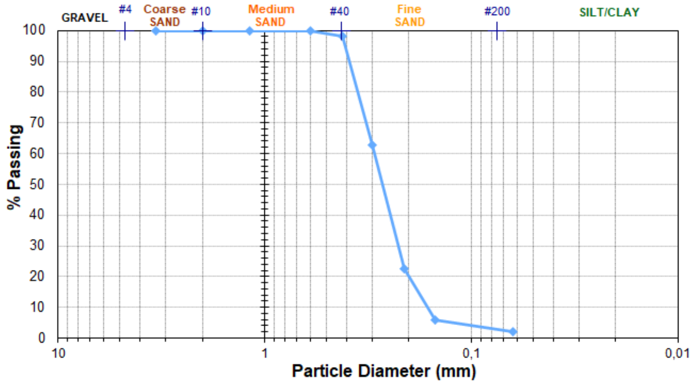

D_{50} **[mm]**		0.281	
Range [mm]	**Mass [g]**	**Soil retained [%]**	**Soil passing [%]**
> 3.5	0.0	0.0	100.0
2.0 - 3.35	0.0	0.0	100.0
1.18 -2.0	0.1	0.0	99.9
0.6 - 1.18	0.1	0.1	99.9
0.42 - 0.6	2.8	1.7	98.1
0.3 - 0.42	57.1	35.2	62.9
0.212 - 0.3	65.8	40.5	22.5
0.15 - 0.212	26.6	16.4	6.1
0.063 - 0.15	6.6	4.0	2.0
< 0.063	0.1	0.1	2.0
Total	159.2	98.0	

Table A.6: Grain size distribution at sample location 6

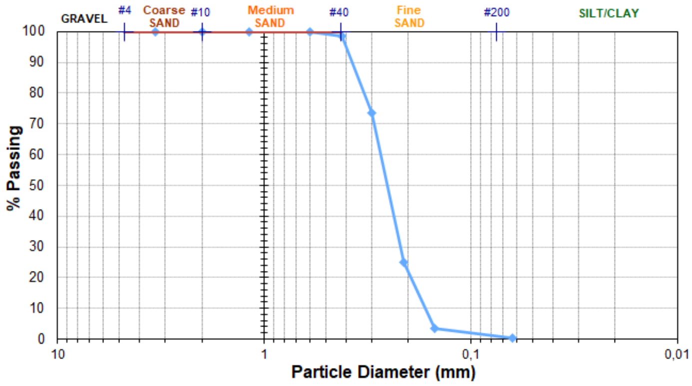

D_{50} [mm]		0.267	
Range [mm]	**Mass [g]**	**Soil retained [%]**	**Soil passing [%]**
> 3.5	0.0	0.0	100.0
2.0 - 3.35	0.0	0.0	100.0
1.18 -2.0	0.1	0.1	99.9
0.6 - 1.18	0.2	0.1	99.8
0.42 - 0.6	2.2	1.3	98.5
0.3 - 0.42	41.0	25.0	73.5
0.212 - 0.3	79.6	48.6	24.9
0.15 - 0.212	35.3	21.5	3.4
0.063 - 0.15	4.8	3.0	0.4
< 0.063	0.0	0.0	0.4
Total	163.2	99.6	

Table A.7: Grain size distribution at sample location 7

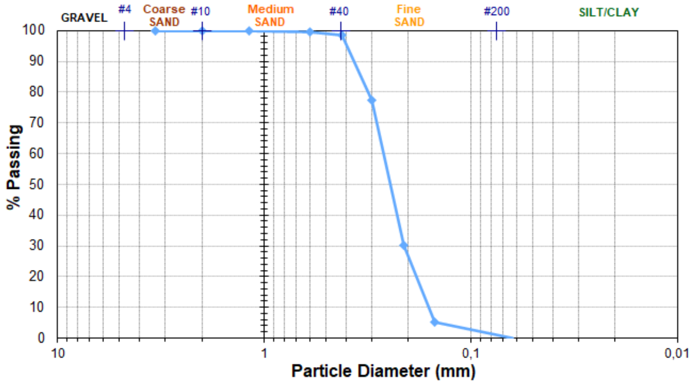

D_{50} [mm]		0.257	
Range [mm]	**Mass [g]**	**Soil retained [%]**	**Soil passing [%]**
> 3.5	0.0	0.0	100.0
2.0 - 3.35	0.0	0.0	100.0
1.18 -2.0	0.1	0.1	99.9
0.6 - 1.18	0.3	0.2	99.7
0.42 - 0.6	1.9	1.1	98.6
0.3 - 0.42	36.3	21.3	77.3
0.212 - 0.3	80.2	47.1	30.2
0.15 - 0.212	42.5	25.0	5.3
0.063 - 0.15	9.1	5.3	-0.1
< 0.063	0.1	0.1	-0.1
Total	170.5	100.1	

Table A.8: Grain size distribution at sample location 8

<table>
<tr><td colspan="4">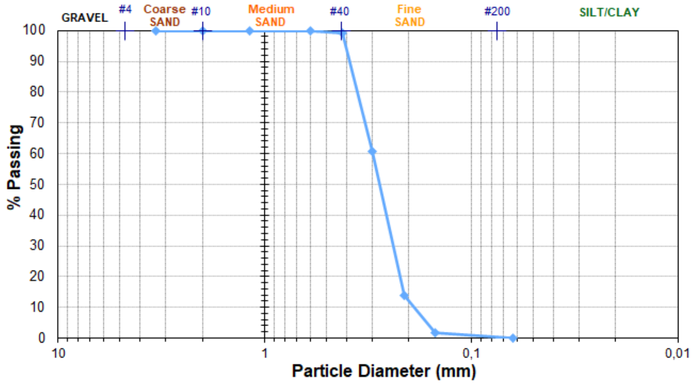
</td></tr>
<tr><td colspan="2">D_{50} [mm]</td><td colspan="2">0.259</td></tr>
<tr><td>Range [mm]</td><td>Mass [g]</td><td>Soil retained [%]</td><td>Soil passing [%]</td></tr>
<tr><td>> 3.5</td><td>0.0</td><td>0.0</td><td>100.0</td></tr>
<tr><td>2.0 - 3.35</td><td>0.0</td><td>0.0</td><td>100.0</td></tr>
<tr><td>1.18 -2.0</td><td>0.1</td><td>0.1</td><td>99.9</td></tr>
<tr><td>0.6 - 1.18</td><td>0.1</td><td>0.1</td><td>99.8</td></tr>
<tr><td>0.42 - 0.6</td><td>0.6</td><td>0.4</td><td>99.4</td></tr>
<tr><td>0.3 - 0.42</td><td>30.9</td><td>20.8</td><td>78.7</td></tr>
<tr><td>0.212 - 0.3</td><td>79.5</td><td>53.5</td><td>25.2</td></tr>
<tr><td>0.15 - 0.212</td><td>31.9</td><td>21.5</td><td>3.7</td></tr>
<tr><td>0.063 - 0.15</td><td>5.6</td><td>3.7</td><td>0.0</td></tr>
<tr><td>< 0.063</td><td>0.0</td><td>0.0</td><td>0.0</td></tr>
<tr><td>Total</td><td>148.7</td><td>100.0</td><td></td></tr>
</table>

Table A.9: Grain size distribution at sample location 9

<table>
<tr><td colspan="4">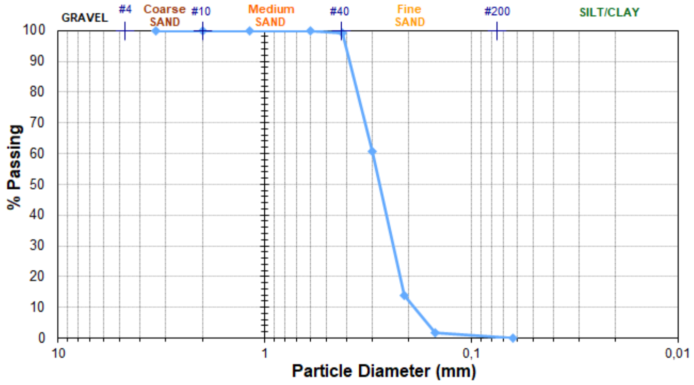
</td></tr>
<tr><td colspan="2">D_{50} [mm]</td><td colspan="2">0.242</td></tr>
<tr><td>Range [mm]</td><td>Mass [g]</td><td>Soil retained [%]</td><td>Soil passing [%]</td></tr>
<tr><td>> 3.5</td><td>0.0</td><td>0.0</td><td>100.0</td></tr>
<tr><td>2.0 - 3.35</td><td>0.0</td><td>0.0</td><td>100.0</td></tr>
<tr><td>1.18 -2.0</td><td>0.0</td><td>0.0</td><td>99.9</td></tr>
<tr><td>0.6 - 1.18</td><td>0.1</td><td>0.1</td><td>99.9</td></tr>
<tr><td>0.42 - 0.6</td><td>0.6</td><td>0.6</td><td>99.3</td></tr>
<tr><td>0.3 - 0.42</td><td>19.1</td><td>17.3</td><td>82.1</td></tr>
<tr><td>0.212 - 0.3</td><td>49.2</td><td>44.4</td><td>37.7</td></tr>
<tr><td>0.15 - 0.212</td><td>32.3</td><td>29.1</td><td>8.6</td></tr>
<tr><td>0.063 - 0.15</td><td>9.6</td><td>8.6</td><td>-0.1</td></tr>
<tr><td>< 0.063</td><td>0.1</td><td>0.0</td><td>-0.1</td></tr>
<tr><td>Total</td><td>110.9</td><td>100.1</td><td></td></tr>
</table>

Table A.10: Grain size distribution at sample location 10

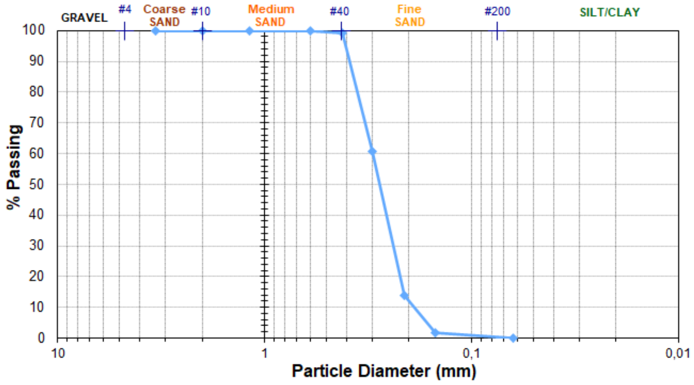

D_{50} **[mm]**		0.293	
Range [mm]	**Mass [g]**	**Soil retained [%]**	**Soil passing [%]**
> 3.5	0.5	0.4	99.6
2.0 - 3.35	0.3	0.2	99.4
1.18 -2.0	0.5	0.3	99.1
0.6 - 1.18	1.5	1.0	98.1
0.42 - 0.6	8,1	5.3	92.9
0.3 - 0.42	38.4	25.1	67.7
0.212 - 0.3	51.9	34.0	33.7
0.15 - 0.212	40.9	26.8	6.9
0.063 - 0.15	10.5	6.9	0.0
< 0.063	0.0	0.0	0.0
Total	152.7	100.0	

Table A.11: Grain size distribution at sample location 11

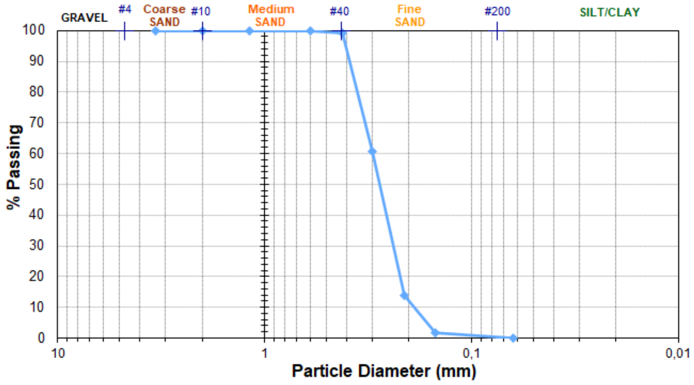

D_{50} **[mm]**		0.291	
Range [mm]	**Mass [g]**	**Soil retained [%]**	**Soil passing [%]**
> 3.5	1.0	0.7	99.3
2.0 - 3.35	0.1	0.1	99.3
1.18 -2.0	0.1	0.0	99.2
0.6 - 1.18	0.2	0.1	99.1
0.42 - 0.6	1.8	1.1	98.0
0.3 - 0.42	50.9	32.9	65.0
0.212 - 0.3	53.3	34.5	30.5
0.15 - 0.212	36.5	23.6	6.9
0.063 - 0.15	10.7	6.9	0.0
< 0.063	0.1	0.0	-0.1
Total	154.6	100.1	

Table A.12: Grain size distribution at sample location 12

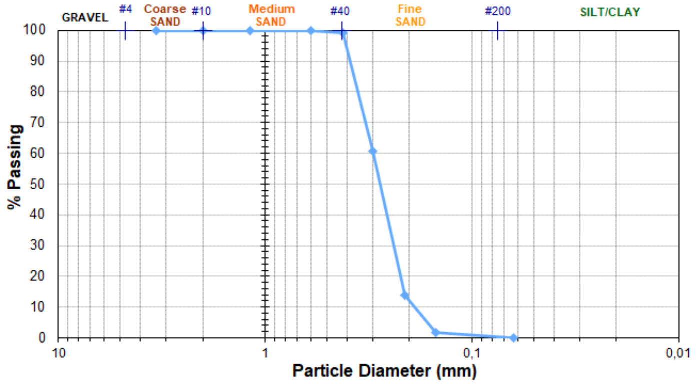

D_{50} [mm]		0.307	
Range [mm]	**Mass [g]**	**Soil retained [%]**	**Soil passing [%]**
> 3.5	1.3	0.9	99.1
2.0 - 3.35	0.1	0.0	99.0
1.18 -2.0	0.1	0.1	99.0
0.6 - 1.18	0.3	0.2	98.7
0.42 - 0.6	2.2	1.5	97.2
0.3 - 0.42	46.5	31.6	65.7
0.212 - 0.3	62.5	42.4	23.2
0.15 - 0.212	27.6	18.8	4.5
0.063 - 0.15	6.5	4.4	0.1
< 0.063	0.1	0.0	0.0
Total	147.3	100.0	

Table A.13: Grain size distribution at sample location 13

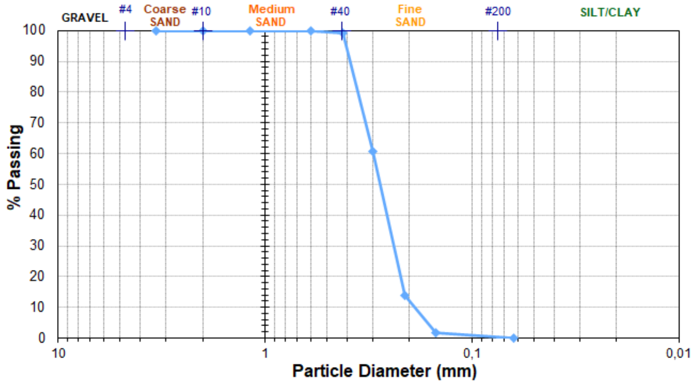

D_{50} [mm]		0.267	
Range [mm]	**Mass [g]**	**Soil retained [%]**	**Soil passing [%]**
> 3.5	0.2	0.2	99.8
2.0 - 3.35	0.0	0.0	99.8
1.18 -2.0	0.0	0.0	99.8
0.6 - 1.18	0.1	0.1	99.8
0.42 - 0.6	1.5	1.0	98.8
0.3 - 0.42	41.6	27.1	71.6
0.212 - 0.3	65.7	42.9	28.8
0.15 - 0.212	33.8	22.0	6.7
0.063 - 0.15	10.3	6.7	0.0
< 0.063	0.1	0.0	0.0
Total	153.3	100.0	

Table A.14: Grain size distribution at sample location 14

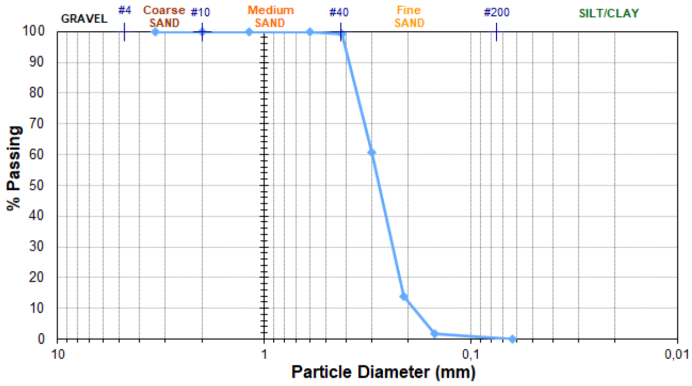

D_{50} **[mm]**	0.290

Range [mm]	**Mass [g]**	**Soil retained [%]**	**Soil passing [%]**
> 3.5	1.2	0.8	99.2
2.0 - 3.35	0.1	0.0	99.2
1.18 -2.0	0.0	0.0	99.2
0.6 - 1.18	0.1	0.1	99.1
0.42 - 0.6	2.2	1.4	97.7
0.3 - 0.42	43.9	28.7	69.1
0.212 - 0.3	63.2	41.2	27.8
0.15 - 0.212	35.3	23.0	4.8
0.063 - 0.15	10.0	6.5	-1.7
< 0.063	0.1	0.0	-1.8
Total	155.9	100.3	

B

Sensitivity Analysis

B.1. Sensitivity runs: m_{cr}

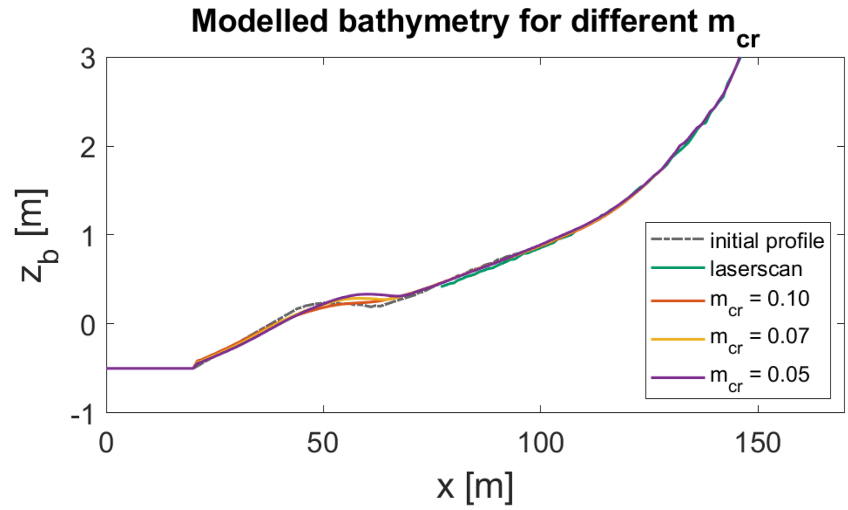

(a) Bathymetry

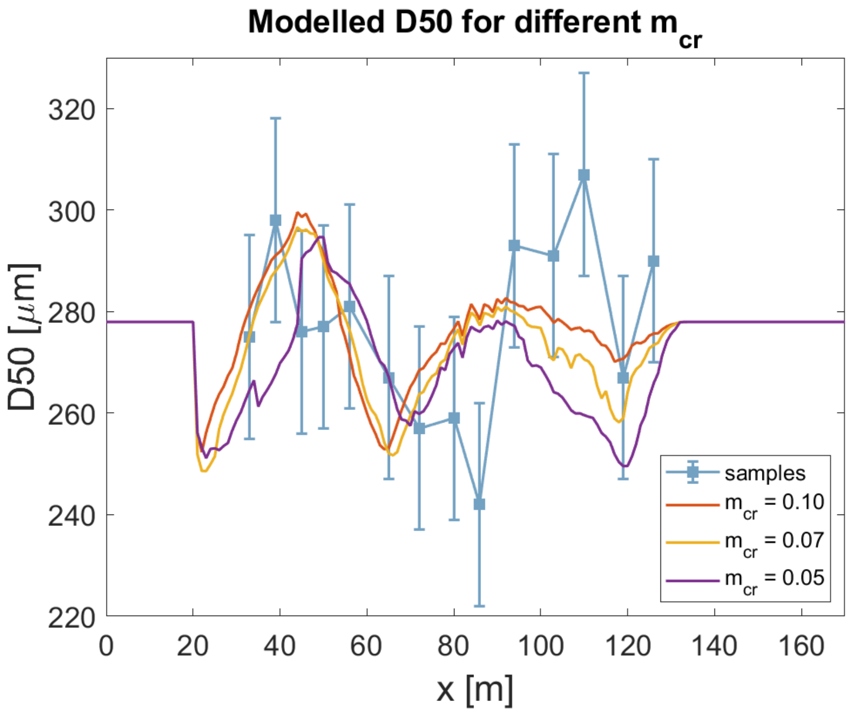

(b) Cross-shore D50

Figure B.1: Sensitivity to m_{cr}. a) Bathymetry and b) D_{50} for an m_{cr} of 0.05, 0.07 and 0.10 at the end of the model period ranging from 29-2-2020 02:00 to 1-3-2020 02:00

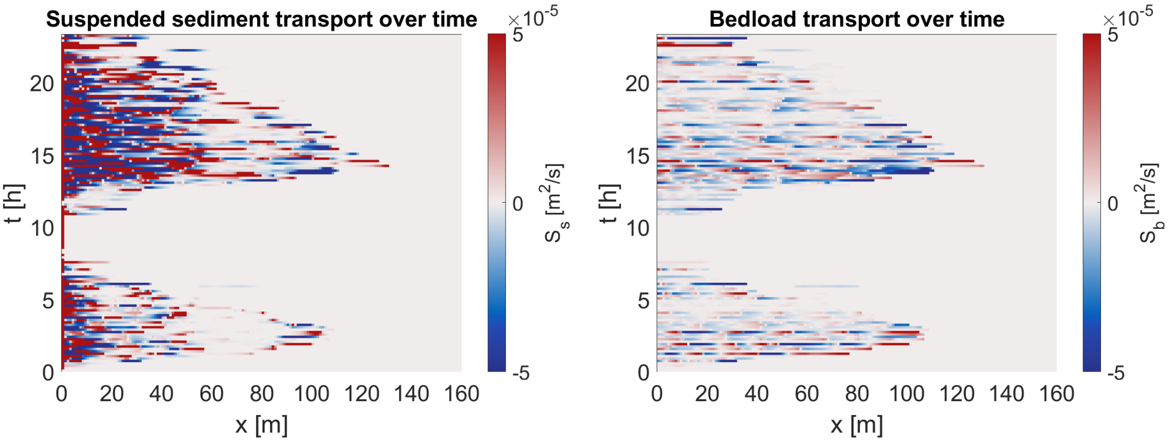

(a) $m_{cr} = 0.05$ (b) $m_{cr} = 0.05$

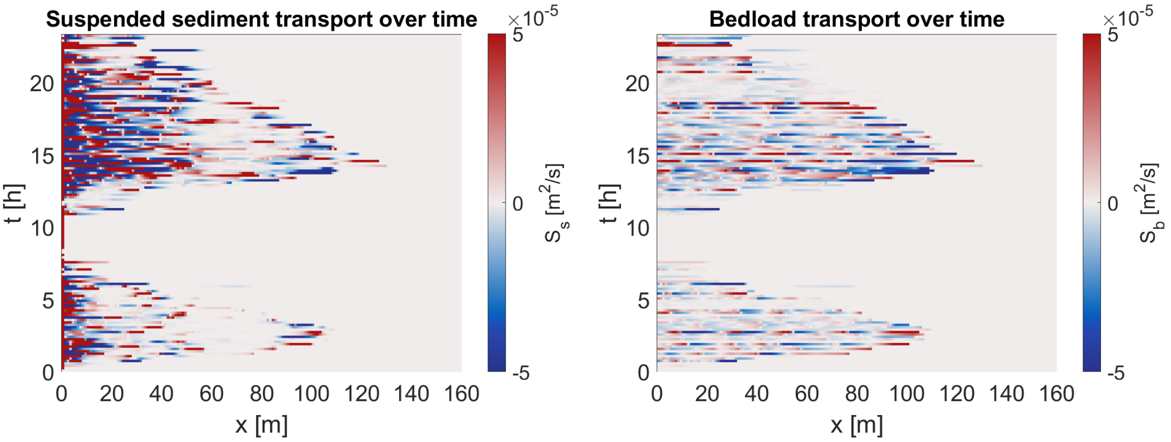

(c) $m_{cr} = 0.07$ (d) $m_{cr} = 0.07$

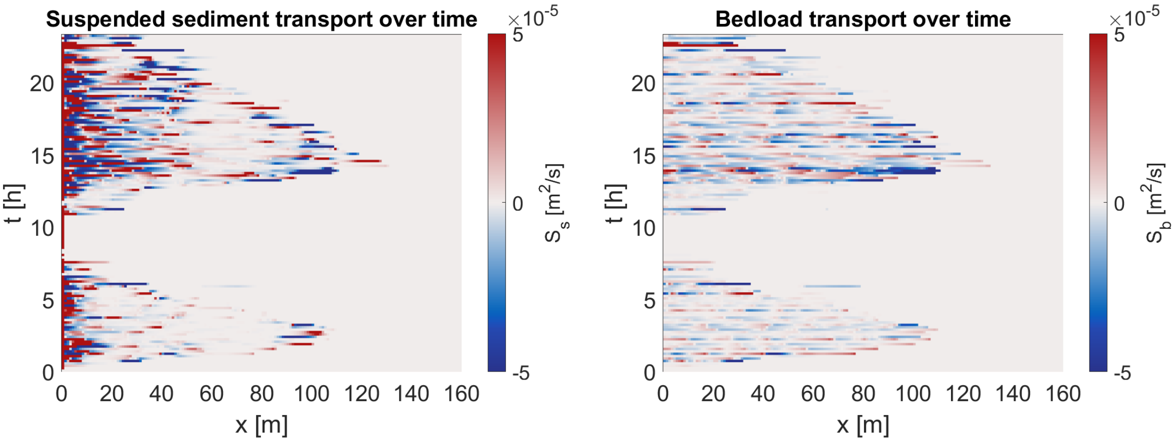

(e) $m_{cr} = 0.1$ (f) $m_{cr} = 0.1$

Figure B.2: Sensitivity of sediment transports to m_{cr}. Modelled sediment transports from 29-2-2020 02:00 to 1-3-02:00. Positive transport rates correspond to onshore transport. a)c)e) suspended sediment transport for a m_{cr} of 0.05, 0.07 and 0.10 respectively. b)d)f) bed load sediment transport for a m_{cr} of 0.05, 0.07 and 0.10 respectively.

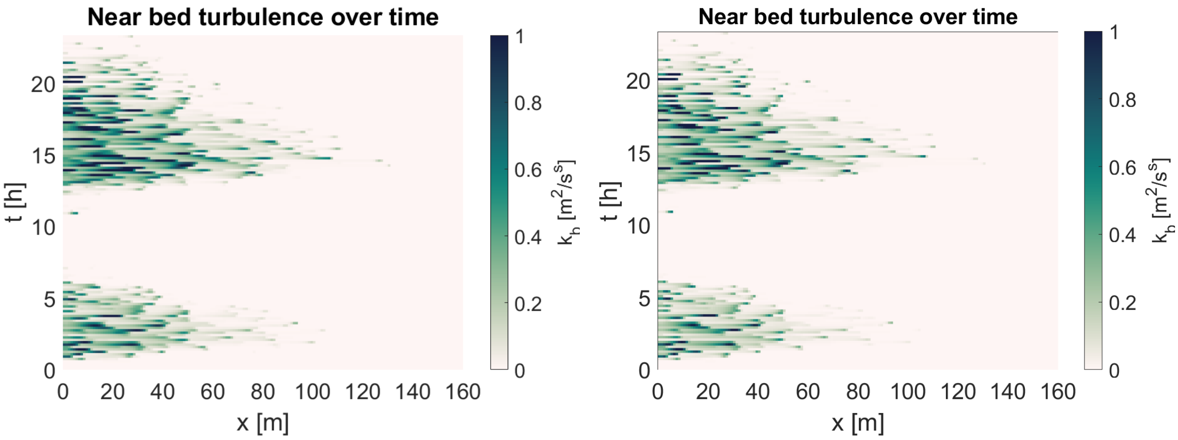

(a) $m_{cr} = 0.05$

(b) $m_{cr} = 0.07$

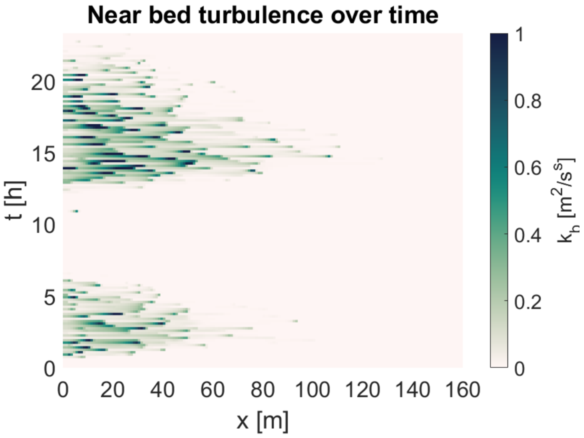

(c) $m_{cr} = 0.1$

Figure B.3: Sensitivity of the near bed turbulent kinetic energy to m_{cr}. Near bed turbulent kinetic energy from 29-2-2020 02:00 to 1-3-02:00 for a m_{cr} of 0.05, 0.07 and 0.10.

B.2. Sensitivity runs: c_r

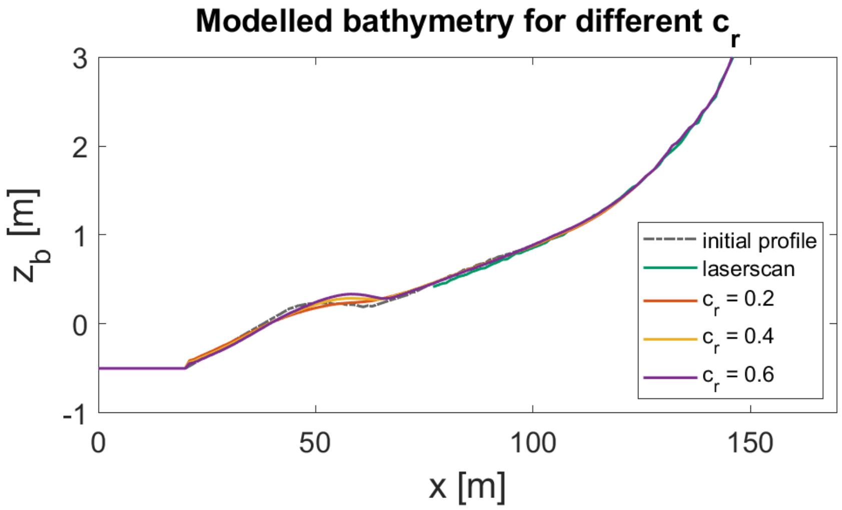

(a) Bathymetry

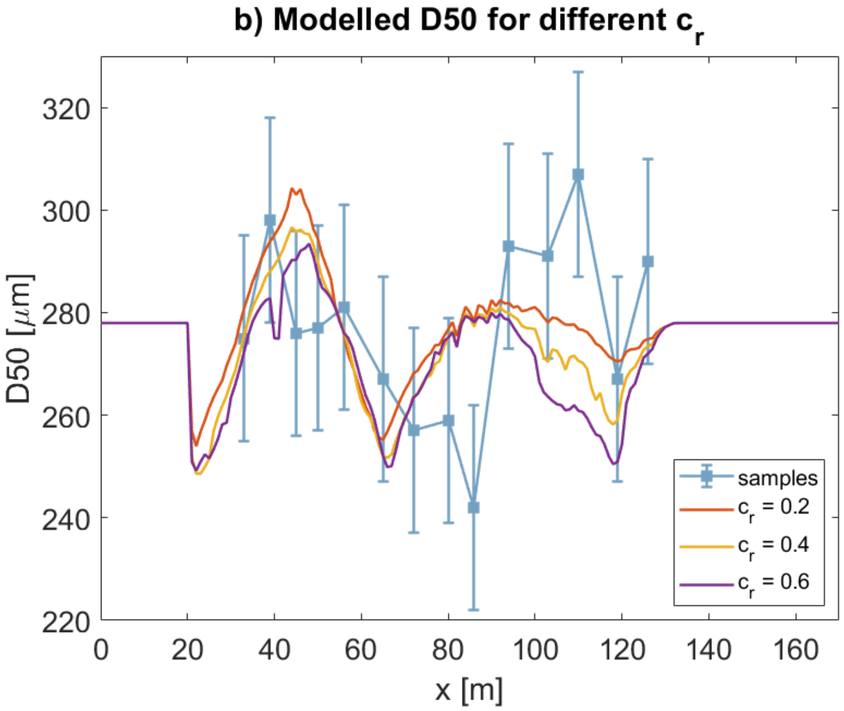

(b) Cross-shore D50

Figure B.4: Sensitivity to c_r. a) Bathymetry and b) D_{50} for an c_r of 0.2, 0.4 and 0.6 at the end of the model period ranging from 29-2-2020 02:00 to 1-3-2020 02:00

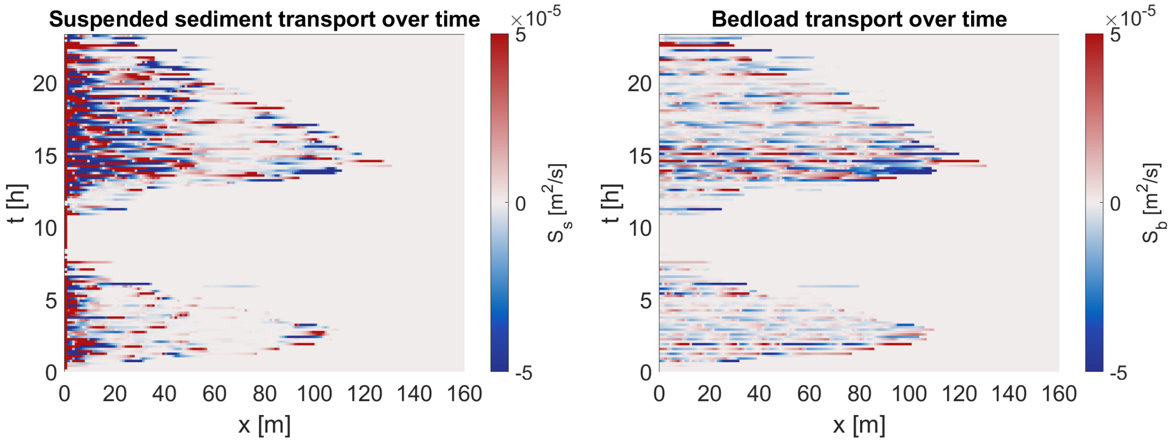

(a) $c_r = 0.2$

(b) $c_r = 0.2$

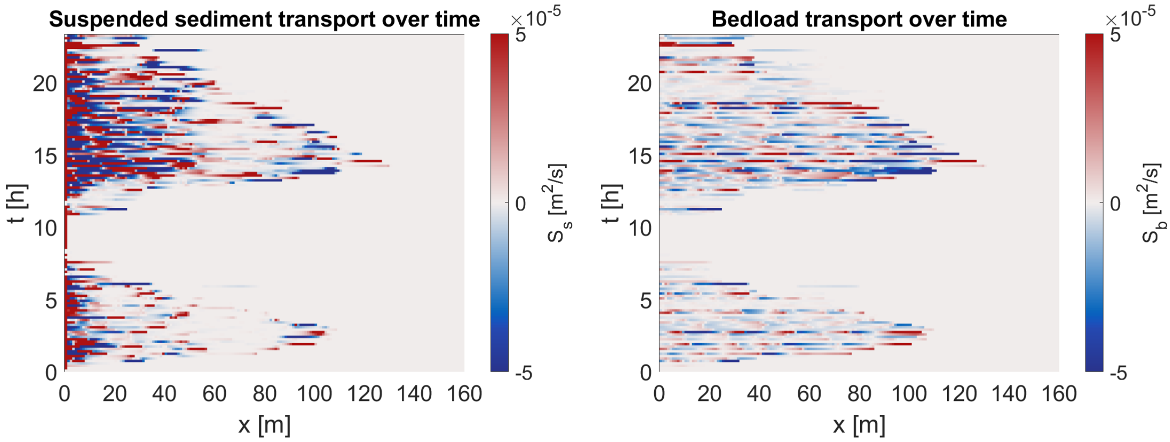

(c) $c_r = 0.4$

(d) $c_r = 0.4$

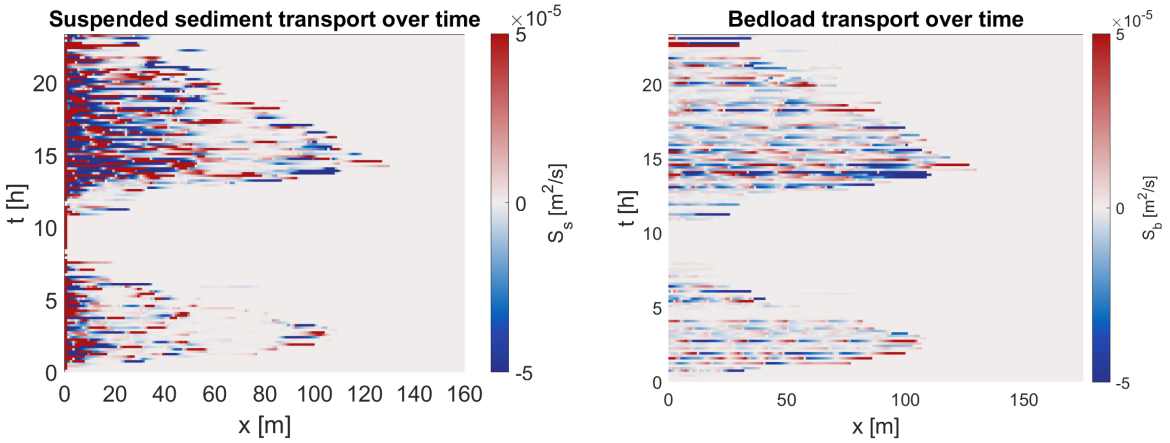

(e) $c_r = 0.6$

(f) $c_r = 0.6$

Figure B.5: Sensitivity of sediment transports to c_r. Modelled sediment transports from 29-2-2020 02:00 to 1-3-02:00. Positive transport rates correspond to onshore transport. a)c)e) suspended sediment transport for a c_r of 0.2, 0.4 and 0.6 respectively. b)d)f) bed load sediment transport for a c_r of 0.2, 0.4 and 0.6 respectively.

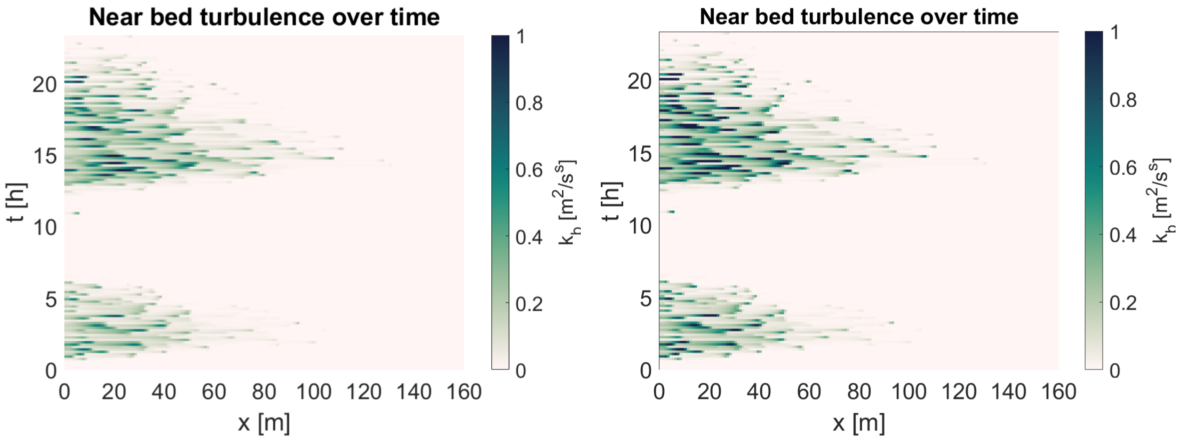

(a) $c_r = 0.2$ (b) $c_r = 0.4$

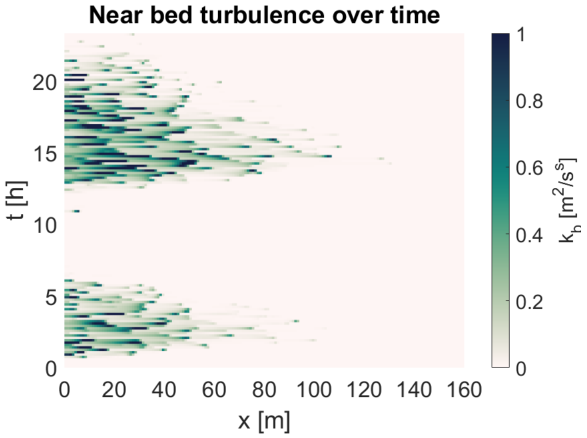

(c) $c_r = 0.6$

Figure B.6: Sensitivity of the near bed turbulent kinetic energy to c_r. Near bed turbulent kinetic energy from 29-2-2020 02:00 to 1-3-02:00 for a c_r of 0.2, 0.4 and 0.6.

B.3. Sensitivity runs: c_k

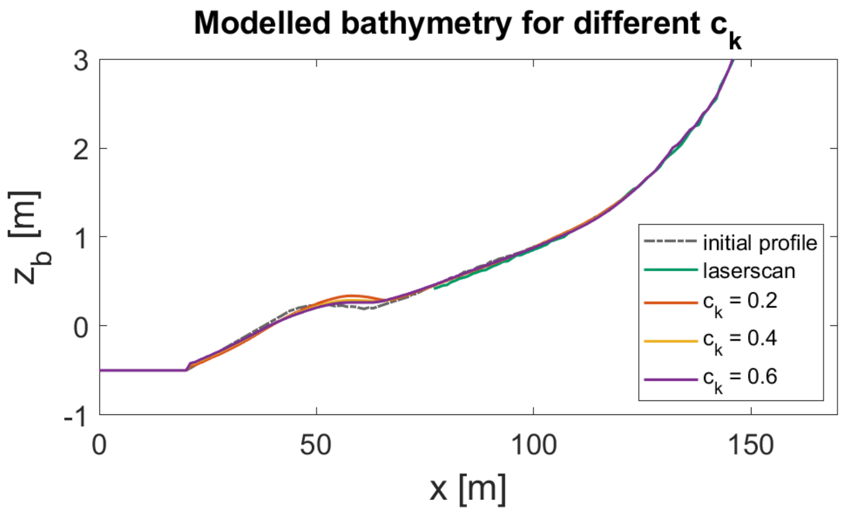

(a) Bathymetry

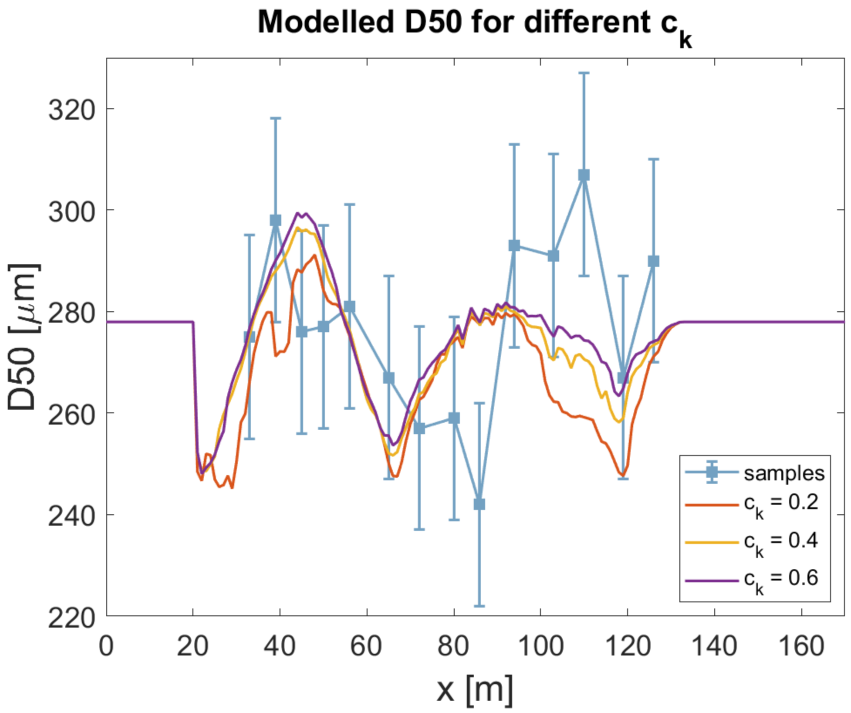

(b) Cross-shore D50

Figure B.7: Sensitivity to c_k. a) Bathymetry and b) D_{50} for an c_k of 0.2, 0.4 and 0.6 at the end of the model period ranging from 29-2-2020 02:00 to 1-3-2020 02:00

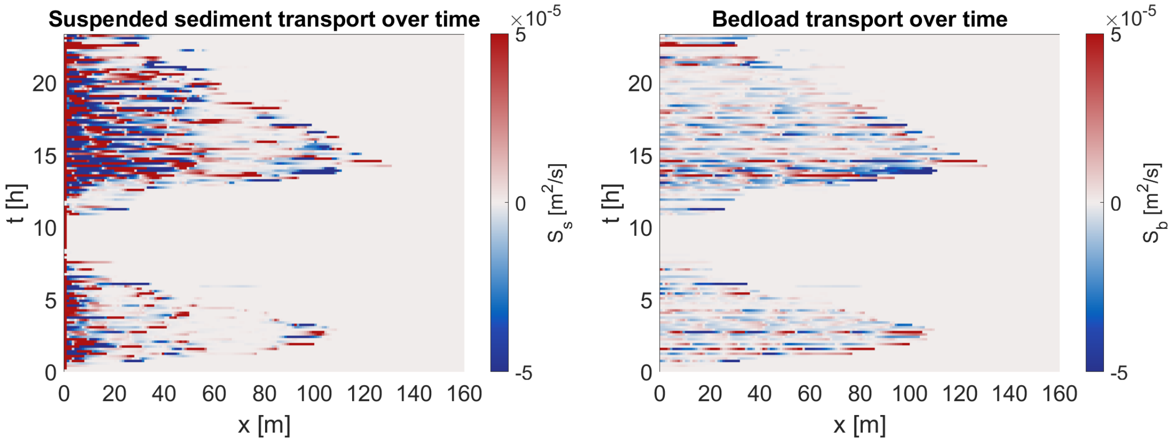

(a) $c_k = 0.2$

(b) $c_k = 0.2$

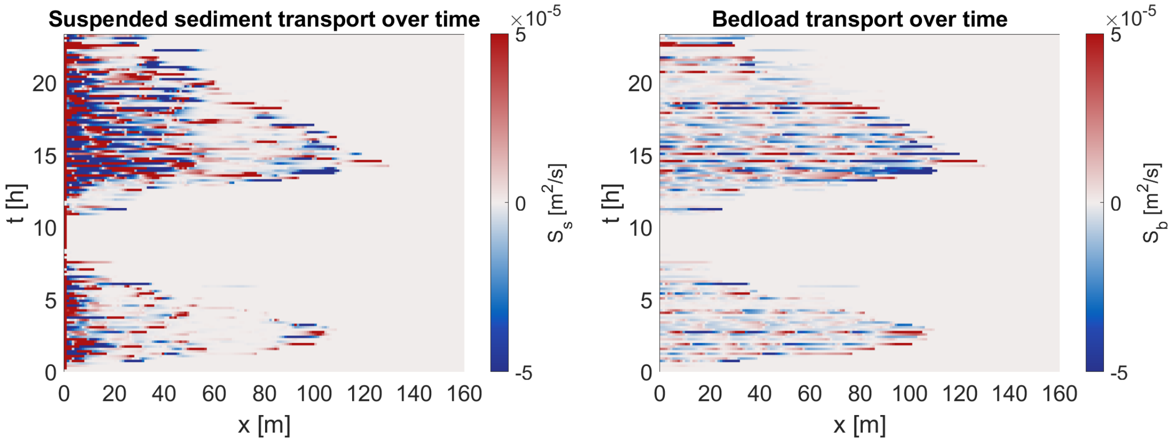

(c) $c_k = 0.4$

(d) $c_k = 0.4$

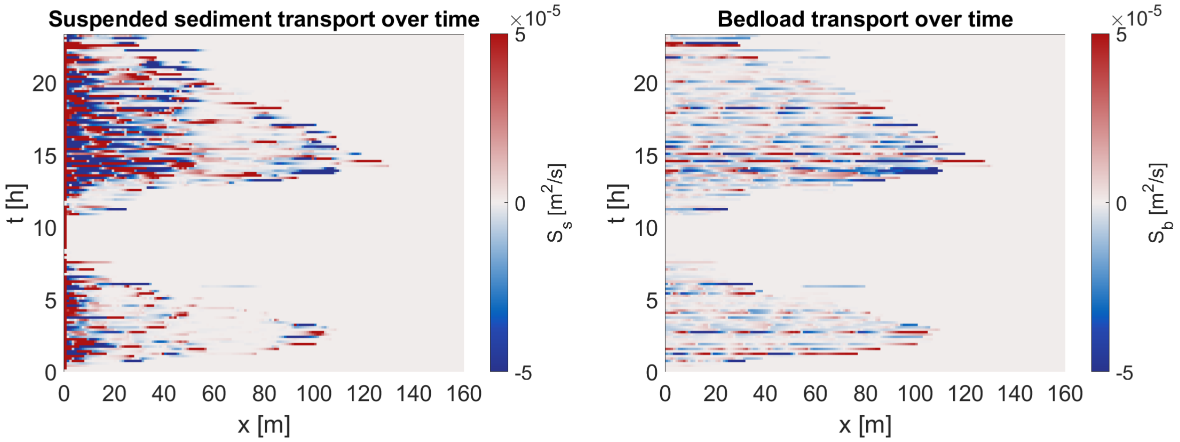

(e) $c_k = 0.6$

(f) $c_k = 0.6$

Figure B.8: Sensitivity of sediment transports to c_k. Modelled sediment transports from 29-2-2020 02:00 to 1-3-02:00. Positive transport rates correspond to onshore transport. a)c)e) suspended sediment transport for a c_k of 0.2, 0.4 and 0.6 respectively. b)d)f) bed load sediment transport for a c_k of 0.2, 0.4 and 0.6 respectively.

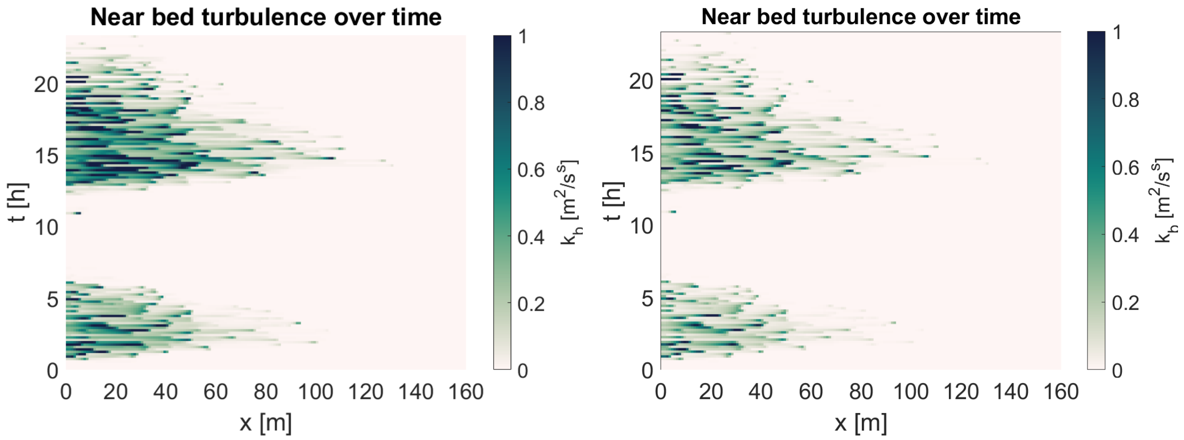

(a) $c_k = 0.2$

(b) $c_k = 0.4$

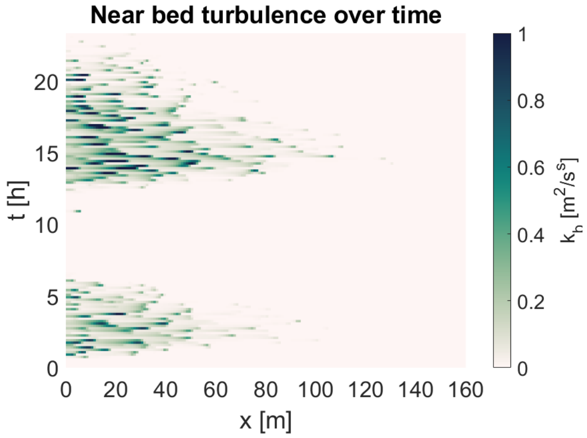

(c) $c_k = 0.6$

Figure B.9: Sensitivity of the near bed turbulent kinetic energy to c_k. Near bed turbulent kinetic energy from 29-2-2020 02:00 to 1-3-02:00 for a c_k of 0.2 0.4 and 0.6.

B.4. Sensitivity runs: ε_s

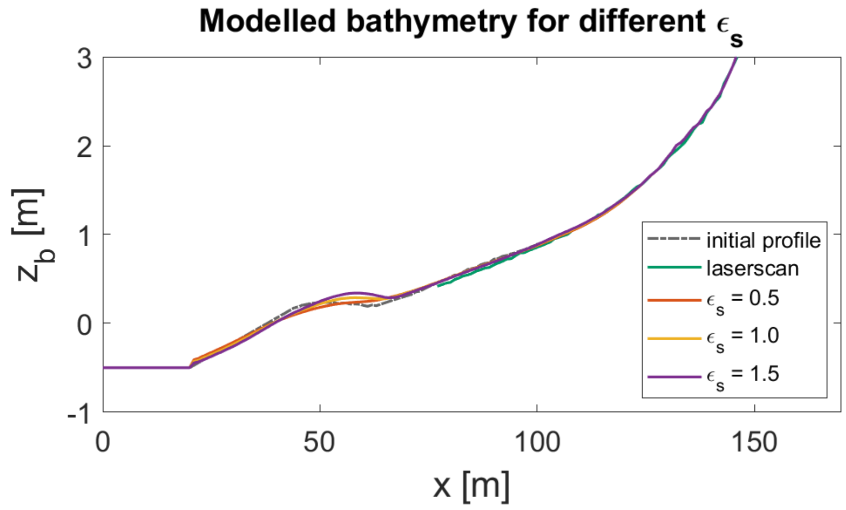

(a) Bathymetry

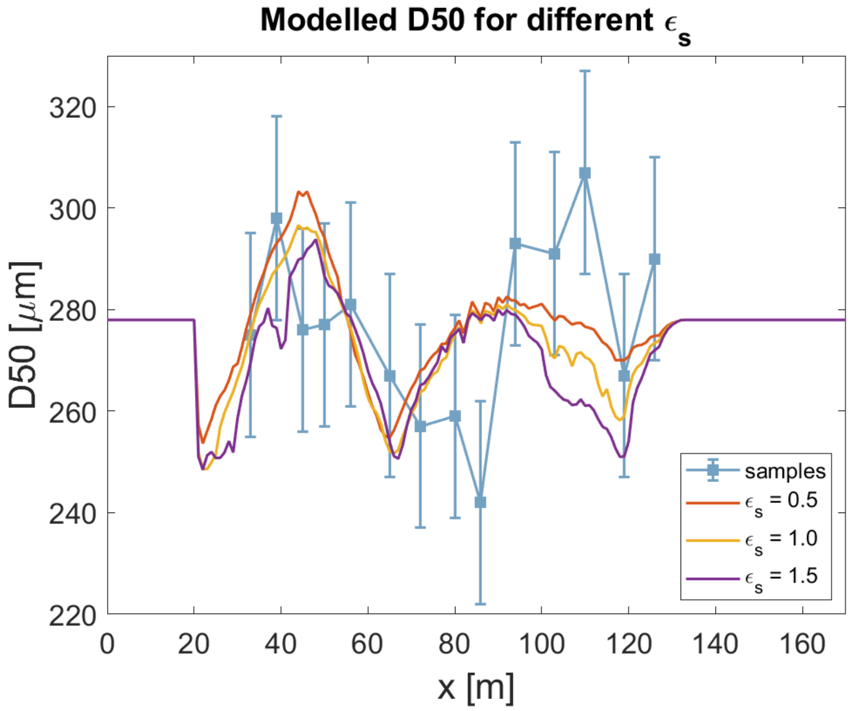

(b) Cross-shore D50

Figure B.10: Sensitivity to ϵ_s. a) Bathymetry and b) D_{50} for an ϵ_s of 0.005, 0.01 and 0.015 at the end of the model period ranging from 29-2-2020 02:00 to 1-3-2020 02:00

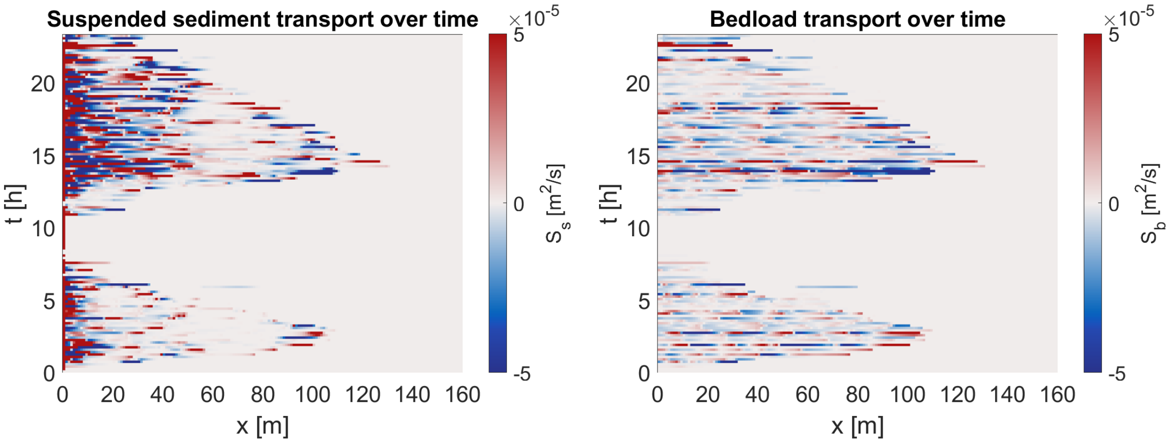

(a) $\epsilon_s = 0.005$ (b) $\epsilon_s = 0.005$

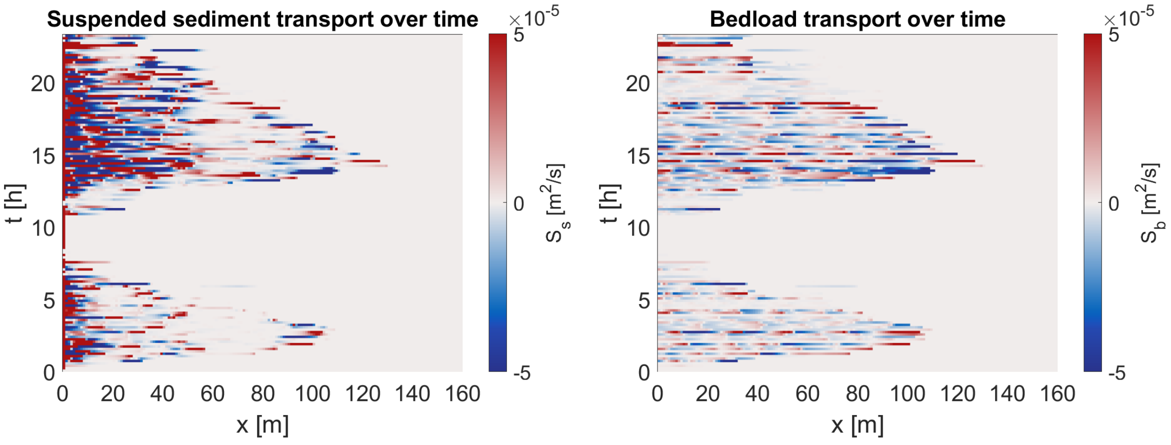

(c) $\epsilon_s = 0.01$ (d) $\epsilon_s = 0.01$

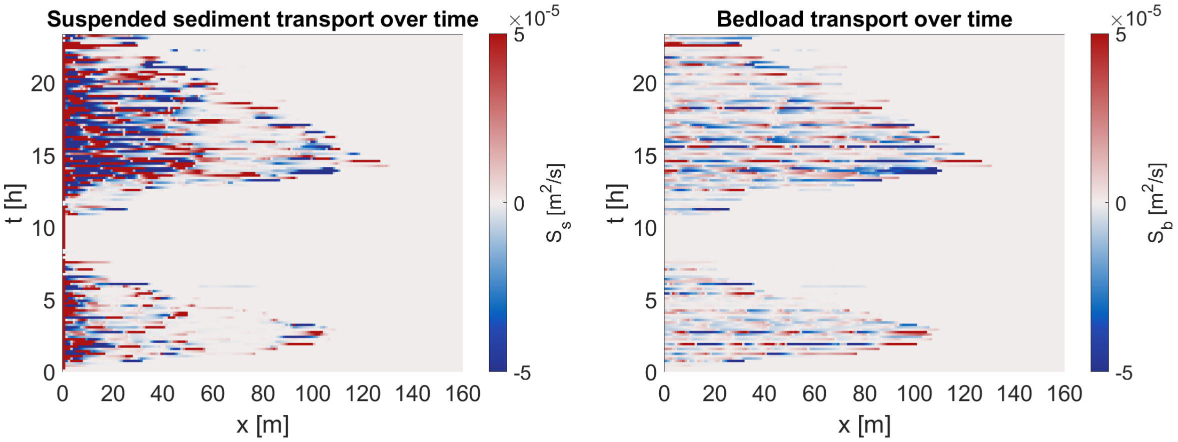

(e) $\epsilon_s = 0.015$ (f) $\epsilon_s = 0.015$

Figure B.11: Sensitivity of sediment transports to ϵ_s. Modelled sediment transports from 29-2-2020 02:00 to 1-3-02:00. Positive transport rates correspond to onshore transport. a)c)e) suspended sediment transport for a ϵ_s of 0.005, 0.01 and 0.015 respectively. b)d)f) bed load sediment transport for a ϵ_s of 0.005, 0.01 and 0.015 respectively.

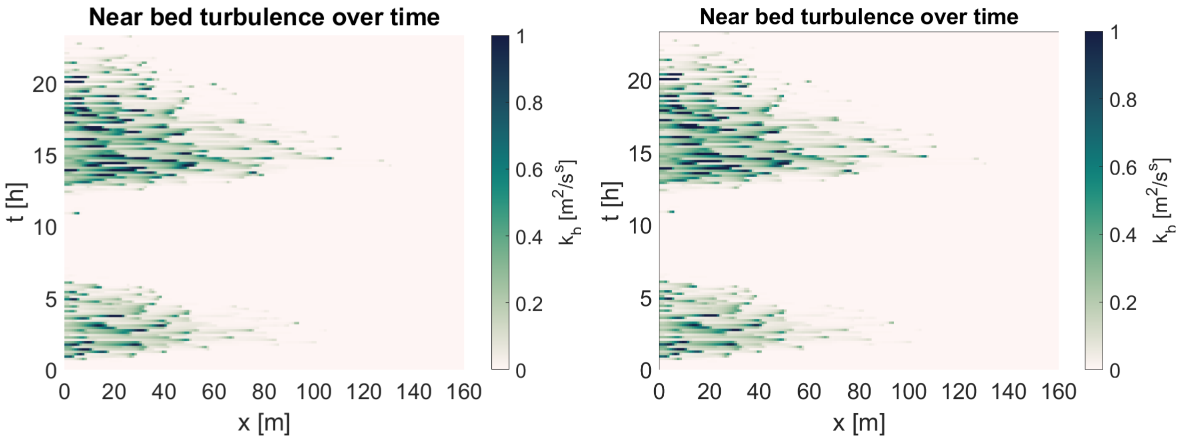

(a) $\epsilon_s = 0.005$

(b) $\epsilon_s = 0.01$

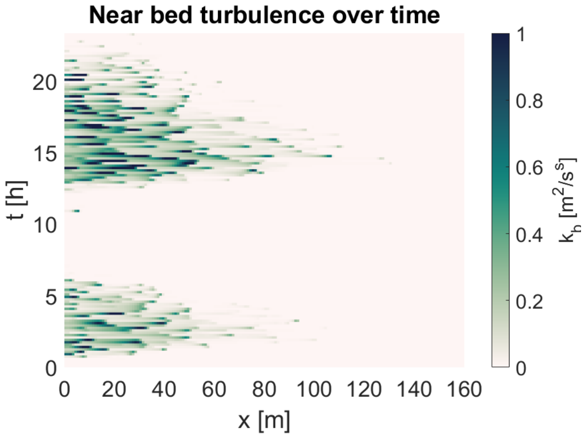

(c) $\epsilon_s = 0.015$

Figure B.12: Sensitivity of the near bed turbulent kinetic energy to ϵ_s. Near bed turbulent kinetic energy from 29-2-2020 02:00 to 1-3-02:00 for a ϵ_s of 0.005, 0.01 and 0.015.

B.5. Sensitivity runs: T_{rep}

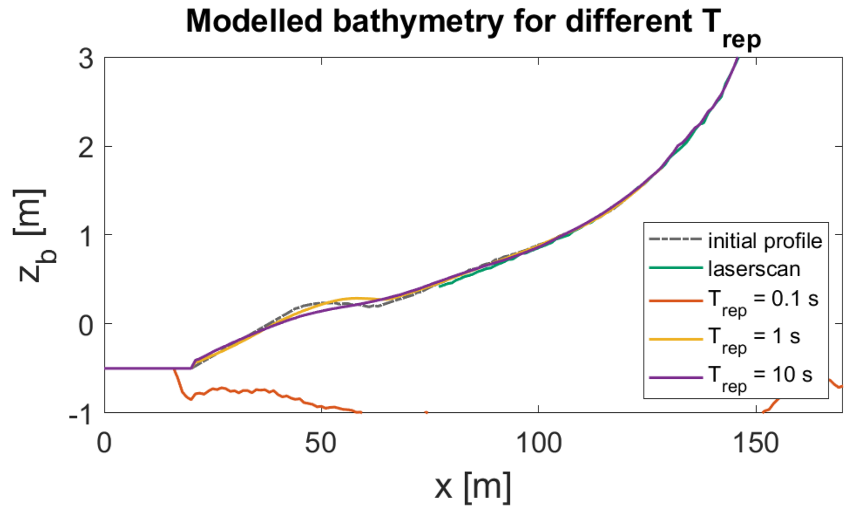

(a) Bathymetry

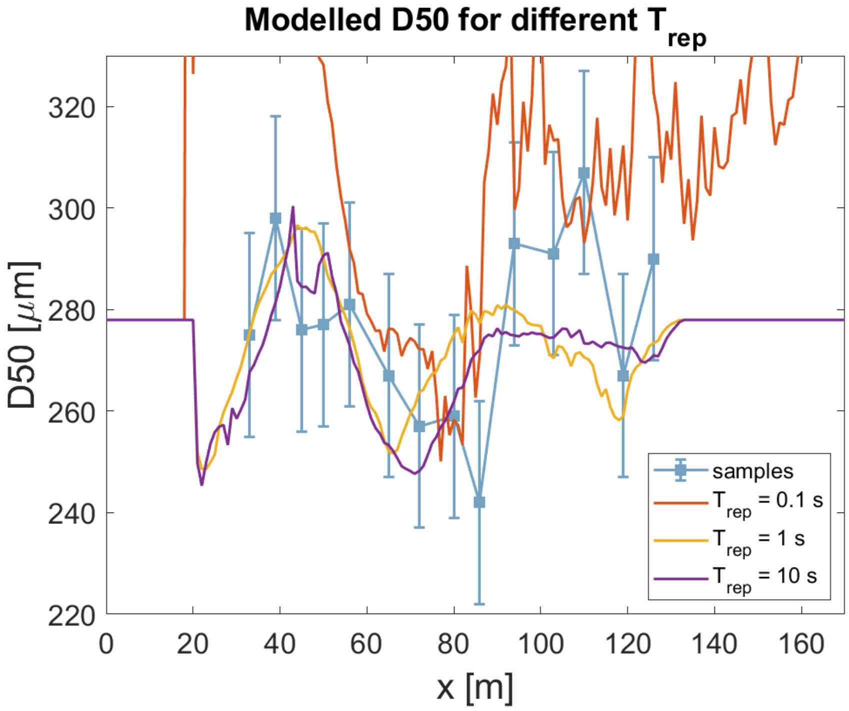

(b) Cross-shore D50

Figure B.13: Sensitivity to T_{rep}. a) Bathymetry and b) D_{50} for an T_{rep} of 0.1, 1 and 10 s at the end of the model period ranging from 29-2-2020 02:00 to 1-3-2020 02:00

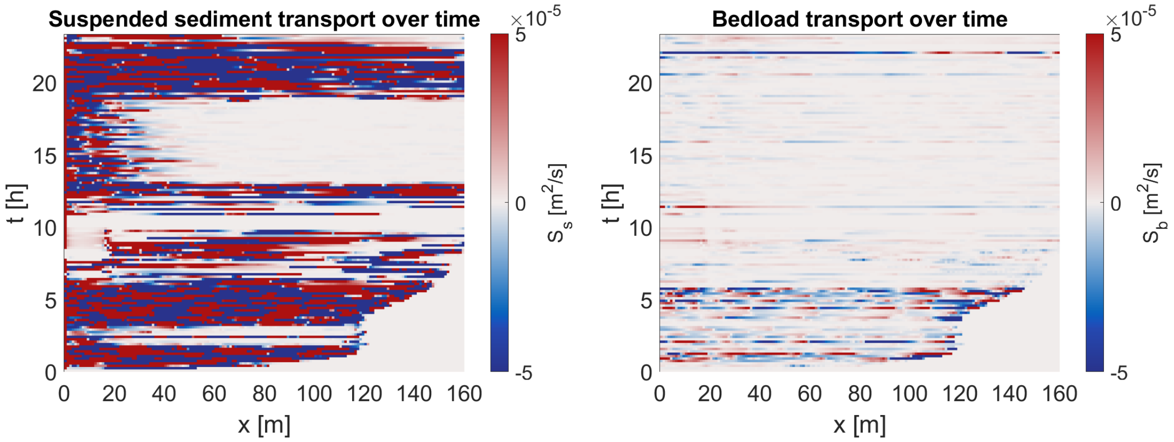

(a) $T_{rep} = 0.1$ s (b) $T_{rep} = 0.1$ s

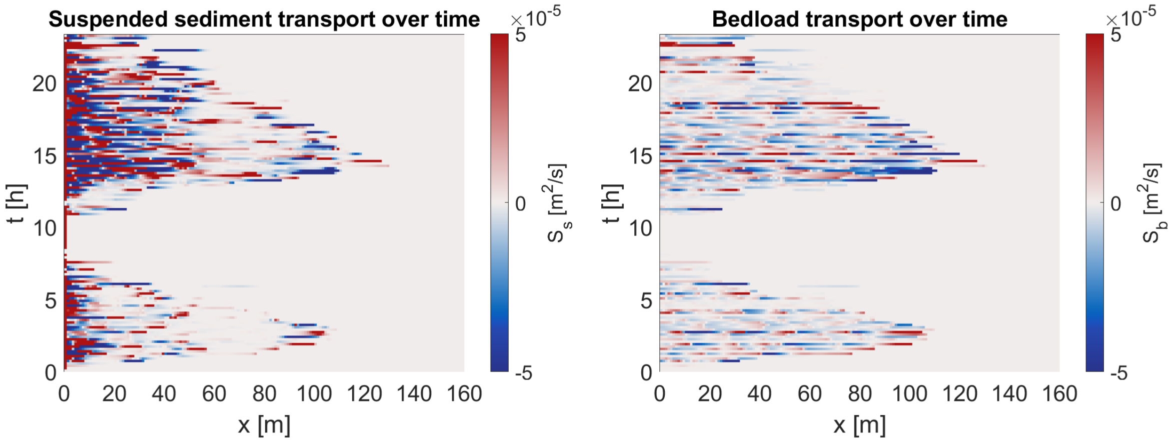

(c) $T_{rep} = 1.0$ s (d) $T_{rep} = 1.0$ s

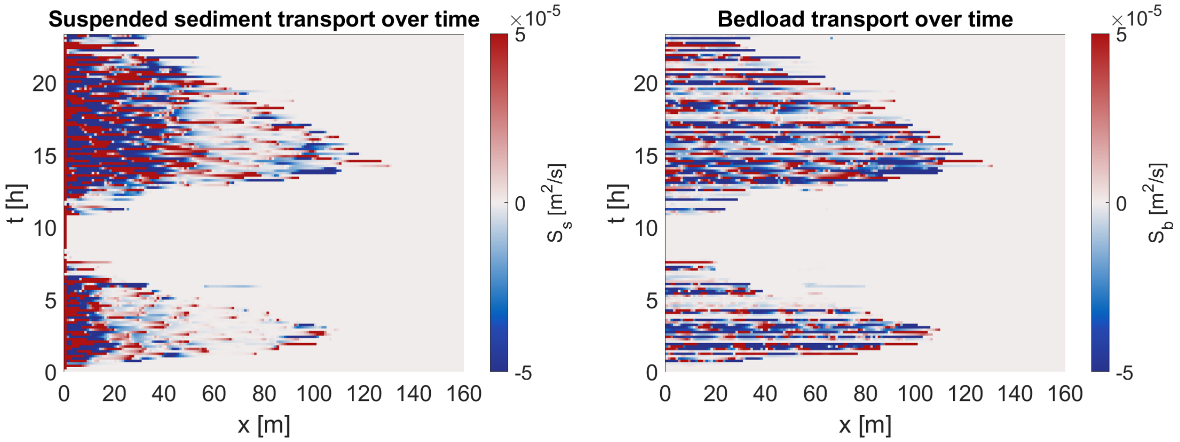

(e) $T_{rep} = 10$ s (f) $T_{rep} = 10$ s

Figure B.14: Sensitivity of sediment transports to T_{rep}. Modelled sediment transports from 29-2-2020 02:00 to 1-3-02:00. Positive transport rates correspond to onshore transport. a)c)e) suspended sediment transport for a T_{rep} of 0.1, 1 and 10 s respectively. b)d)f) bed load sediment transport for a T_{rep} of 0.1, 1 and 10 s respectively.

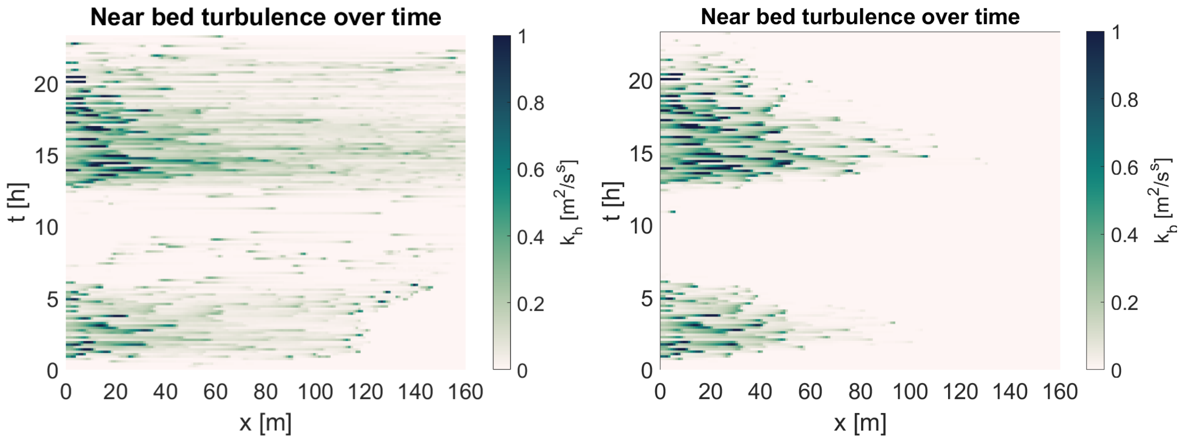

(a) $T_{rep} = 0.1$ s

(b) $T_{rep} = 1.0$ s

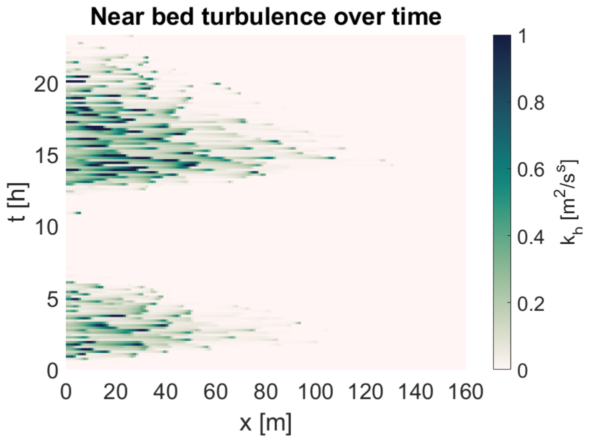

(c) $T_{rep} = 10$ s

Figure B.15: Sensitivity of the near bed turbulent kinetic energy to T_{rep}. Near bed turbulent kinetic energy from 29-2-2020 02:00 to 1-3-02:00 for a T_{rep} of 0.005, 0.01 and 0.015.

B.6. Sensitivity runs: γ

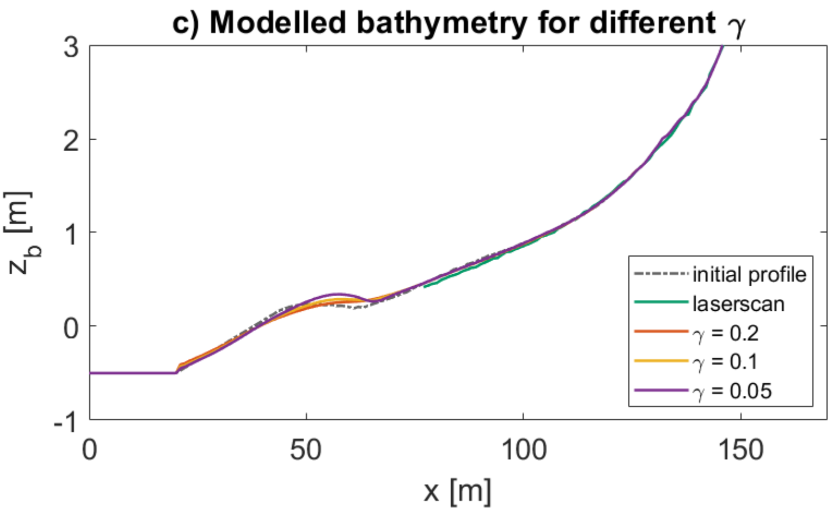

(a) Bathymetry

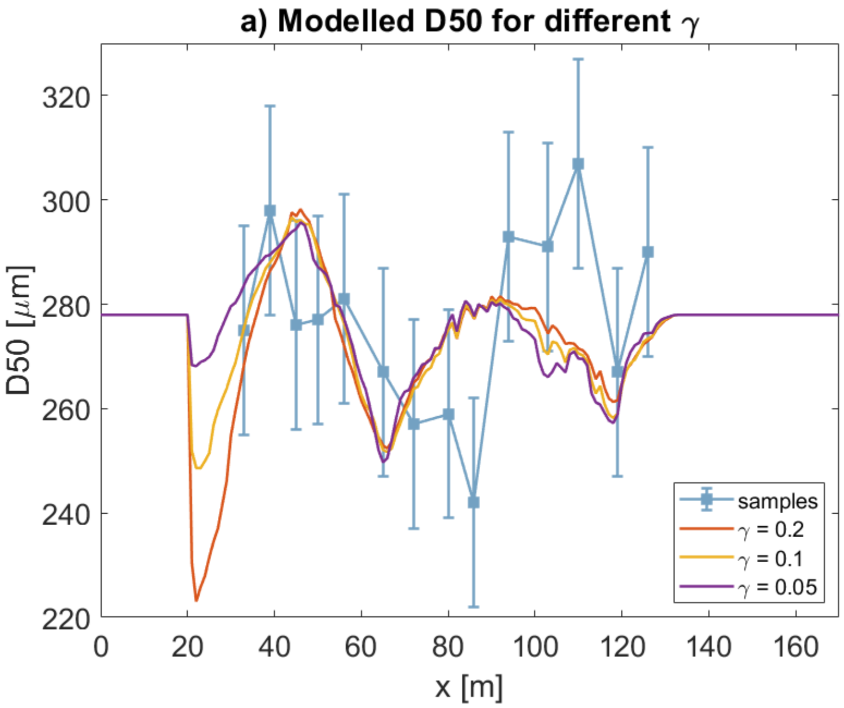

(b) Cross-shore D50

Figure B.16: Sensitivity to γ. a) Bathymetry and b) D_{50} for an γ of 0.05, 0.1 and 0.2 at the end of the model period ranging from 29-2-2020 02:00 to 1-3-2020 02:00

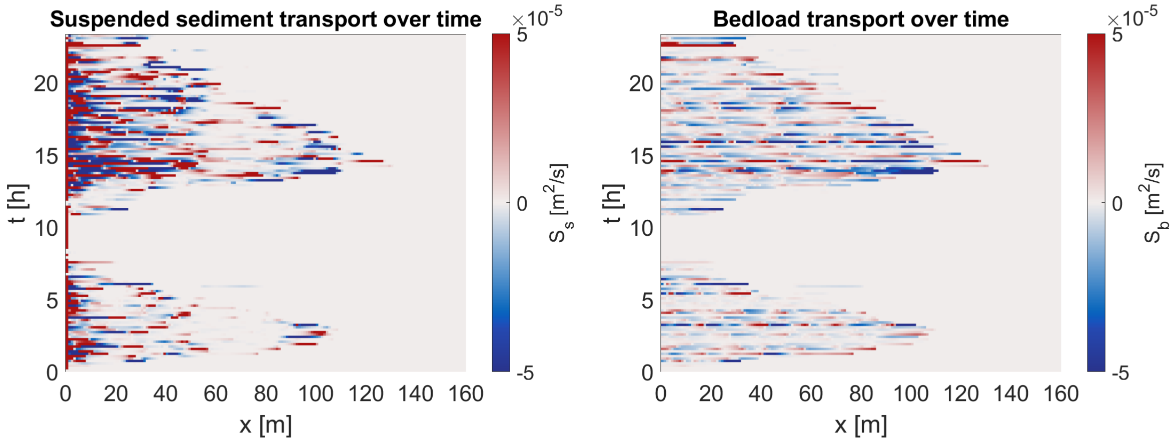

(a) $\gamma = 0.05$ (b) $\gamma = 0.05$

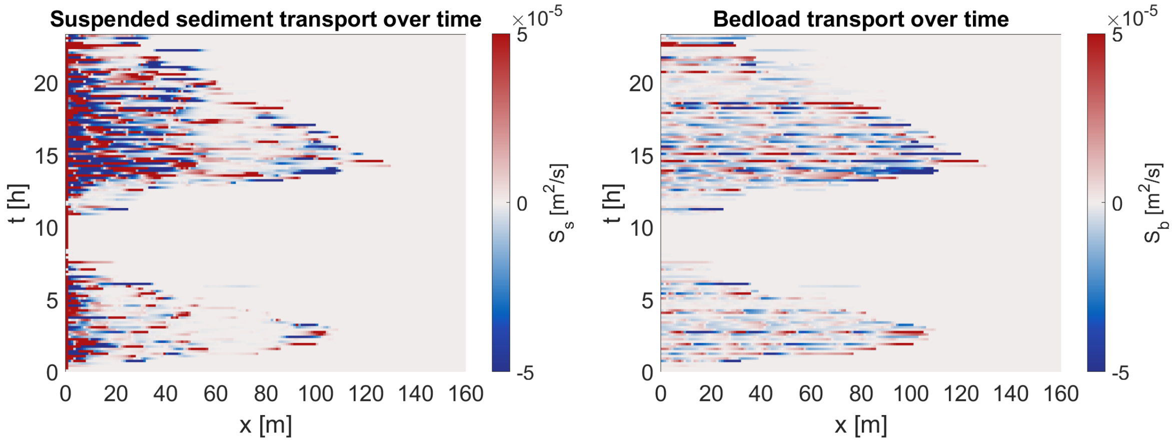

(c) $\gamma = 0.1$ (d) $\gamma = 0.1$

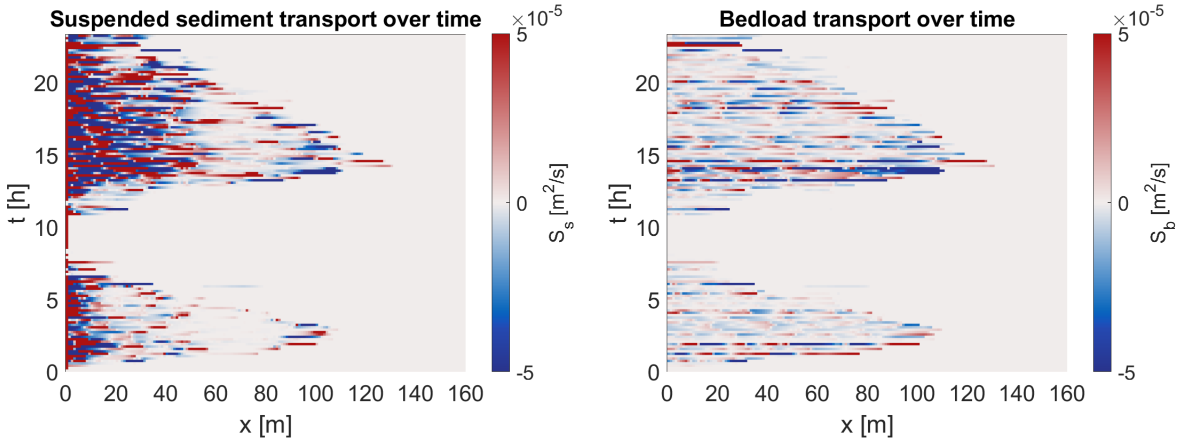

(e) $\gamma = 0.2$ (f) $\gamma = 0.2$

Figure B.17: Sensitivity of sediment transports to γ. Modelled sediment transports from 29-2-2020 02:00 to 1-3-02:00. Positive transport rates correspond to onshore transport. a)c)e) suspended sediment transport for a γ of 0.05, 0.1 and 0.2 respectively. b)d)f) bed load sediment transport for a γ of 0.05, 0.1 and 0.2 respectively.

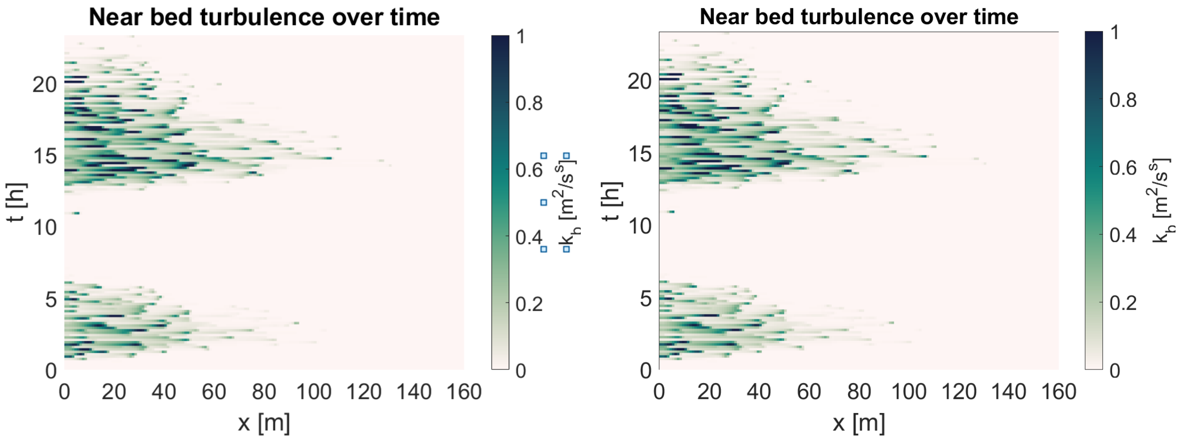

(a) $\gamma = 0.05$

(b) $\gamma = 0.05$

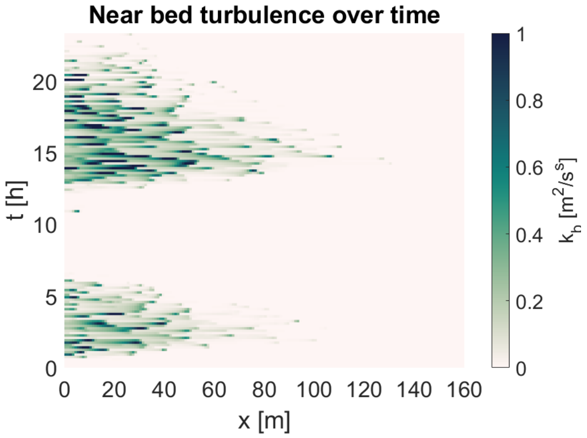

(c) $\gamma = 0.2$

Figure B.18: Sensitivity of the near bed turbulent kinetic energy to γ. Near bed turbulent kinetic energy from 29-2-2020 02:00 to 1-3-02:00 for a γ of 0.05, 0.1 and 0.2.

B.7. Sensitivity runs: d_{ADV}

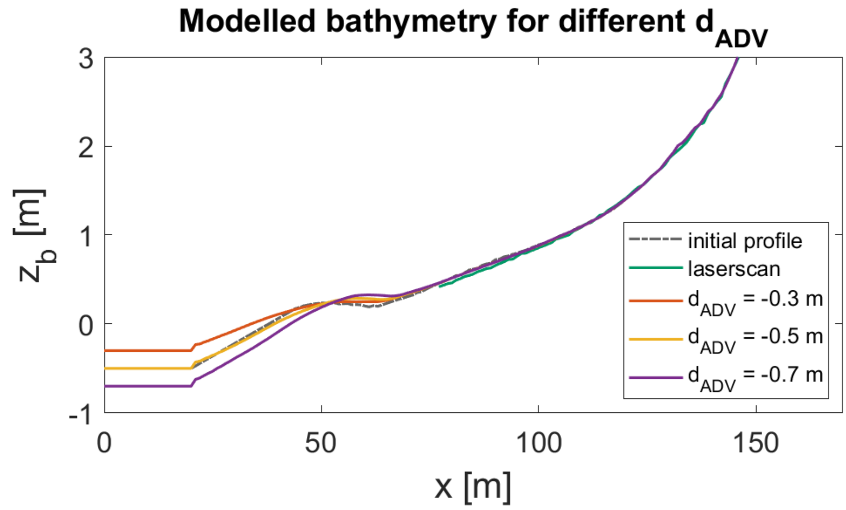

(a) Bathymetry

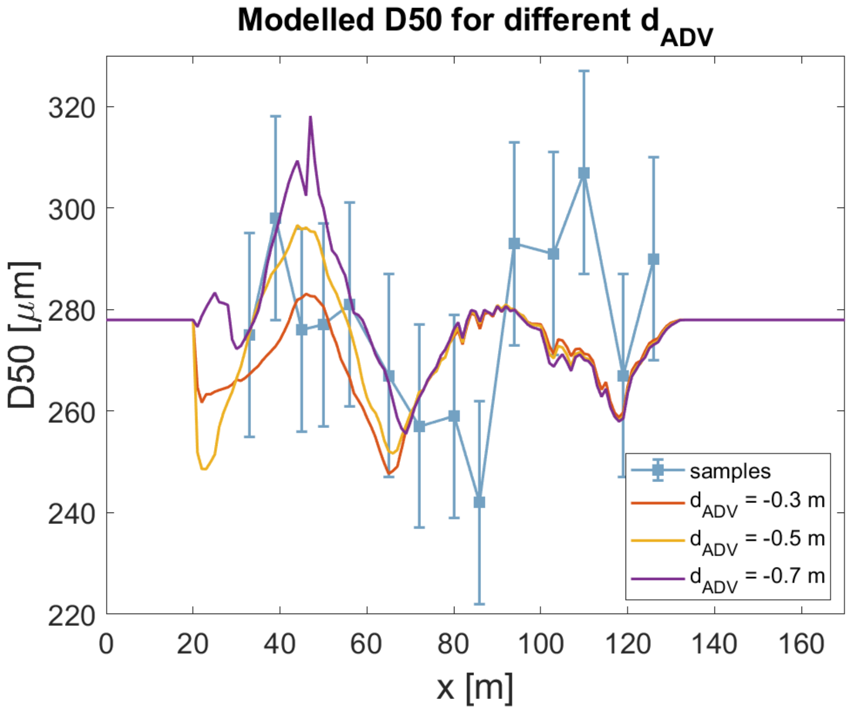

(b) Cross-shore D50

Figure B.19: Sensitivity to d_{ADV}. a) Bathymetry and b) D_{50} for an d_{ADV} of -0.7, -0.5 and -0.3 m at the end of the model period ranging from 29-2-2020 02:00 to 1-3-2020 02:00

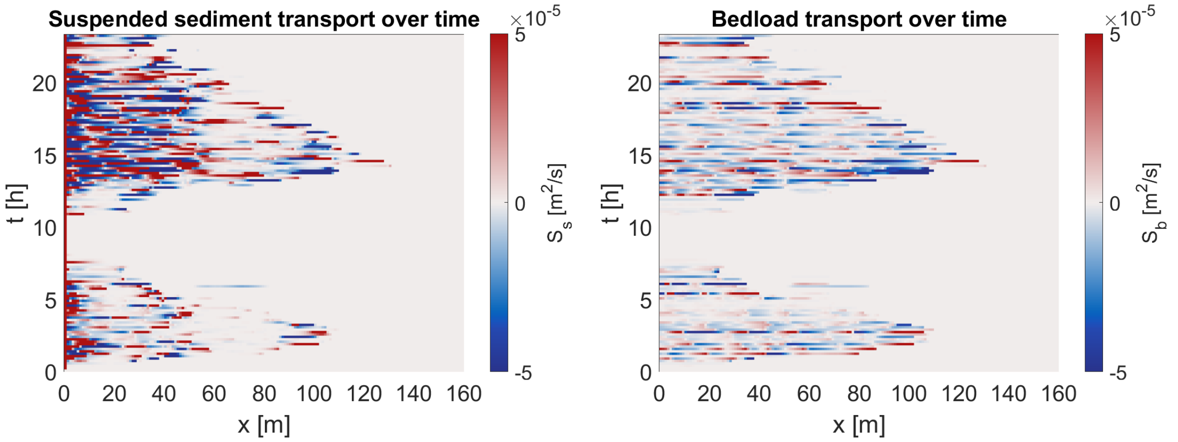

(a) $d_{ADV} = -0.7$ m (b) $d_{ADV} = -0.7$ m

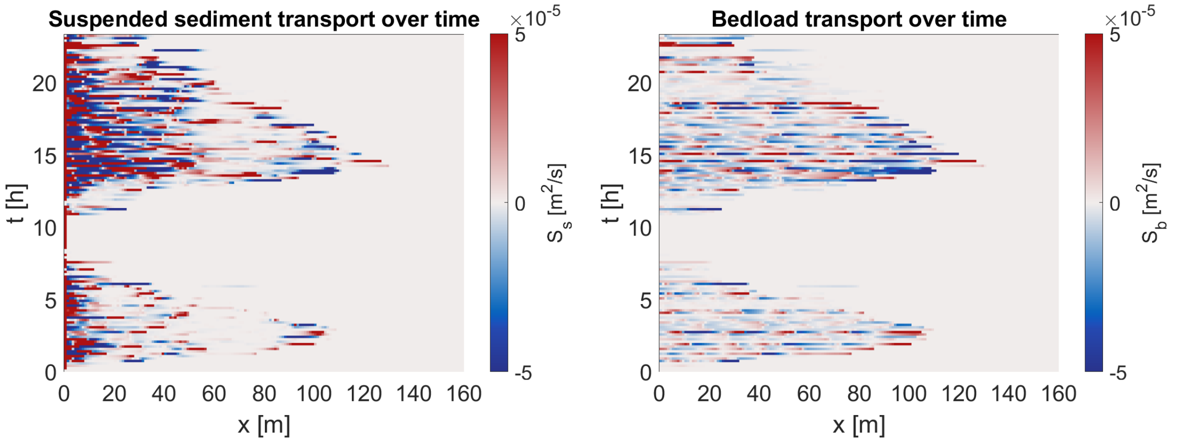

(c) $d_{ADV} = -0.5$ m (d) $d_{ADV} = -0.5$ m

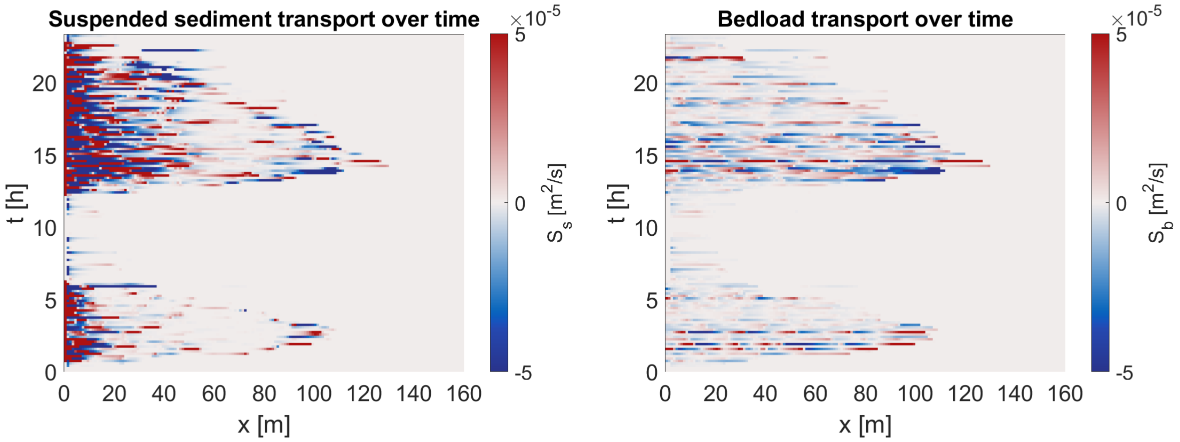

(e) $d_{ADV} = -0.3$ m (f) $d_{ADV} = -0.3$ m

Figure B.20: Sensitivity of sediment transports to d_{ADV}. Modelled sediment transports from 29-2-2020 02:00 to 1-3-02:00. Positive transport rates correspond to onshore transport. a)c)e) suspended sediment transport for a d_{ADV} of −0.7, −0.5 and −0.3 m respectively. b)d)f) bed load sediment transport for a d_{ADV} of −0.7, −0.5 and −0.3 m respectively.

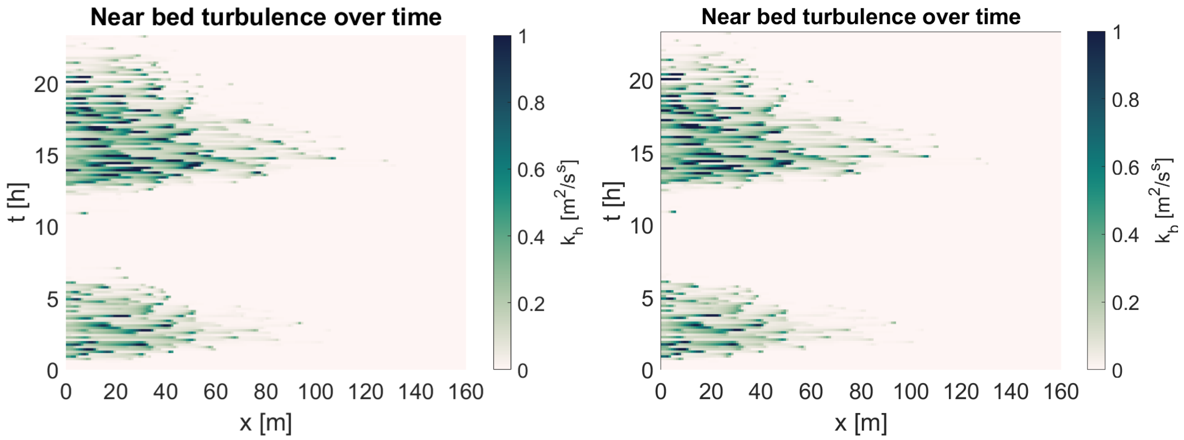

(a) d_{ADV} = −0.7 m

(b) d_{ADV} = −0.5 m

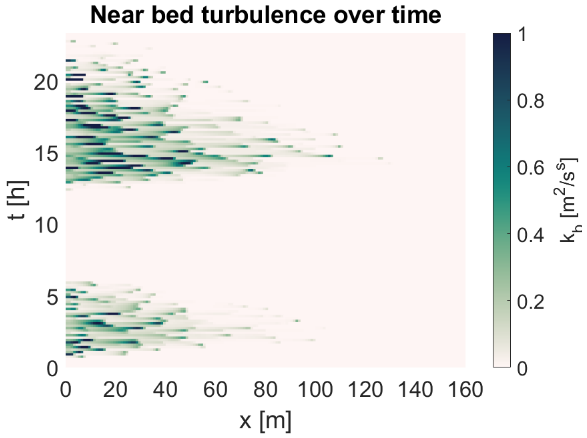

(c) d_{ADV} = −0.3 m

Figure B.21: Sensitivity of the near bed turbulent kinetic energy to d_{ADV}. Near bed turbulent kinetic energy from 29-2-2020 02:00 to 1-3-02:00 for a d_{ADV} of −0.7, −0.5 and −0.3 m.

C

Model stability

The XBeach model experienced stability problems when bores approached during low water. This resulted in very high flow velocities at the boundary between fixed and free points, causing large turbulence and erosion.

XBeach uses explicit numerical schemes for the hydraulics and the bed level update (XBeachDocs, 2020). These schemes are conditionally stable when the time step is chosen small enough. For the flow conditions this time step is based on the Courant number and for the bed level update the restriction is based on the fact that no more sediment can be eroded than is present in the top layer (Reniers et al., 2013). Normally, the time step for the hydraulics is more restrictive, so XBeach uses the Courant number to determine the the time step. However, in case of large erosion and/or small top layers, this time step can become insufficient and the model becomes unstable. In order to mitigate this effect multiple routes are available (fig. C.1), which will be explained below.

There are two parameters built in to avoid unrealistic flow processes in very shallow water: h_{min} and eps. The h_{min} is the threshold water depth above which Stokes' drift is taken into account and prevents very high return flows and the eps sets the threshold that determines whether cells are wet or dry (XBeachDocs, 2020). Larger values of these parameters make the modelled look unrealistic as during low tide parts of the beach remained covered under a significant layer of water (fig. C.2), but will aid in model stability. For the model runs the lowest values that still gave stable results were chosen.

Additionaly, the XBeach 1D-NLSW mode has been adjusted in two ways compared to the model described by Reniers et al. to improve the stability (2013). First, the average turbulence over a period T_{rep} is used in stead of the instantaneous turbulence. This smooths the turbulence signal and decreases the effect of sudden high turbulence peaks caused by unrealistically high velocities. Second, the numerical implementation of the Riemann boundary condition at the offshore boundary was adjusted. In the old situation the flow velocity at the offshore boundary was computed using the water depth at the point next to the boundary point, but in the adjustment the maximum value of either the boundary point ($x = 0$) or the point next to it ($x - 1$) was used (eq. C.1). Also, the water depth was linked to the h_{min} to ensure a minimum water depth. The new implementation of the Riemann boundary prevents computing of very high velocities for very low water depths.

$$\begin{aligned} u(x=0.5) &= \sqrt{\frac{g}{h_t}}\, max\left(\eta(x=0), \eta(x=1)\right) \\ h_t &= max\left(h(x=1), h_{min}\right) \end{aligned} \tag{C.1}$$

where:

u = flow velocity
x = grid point
h_t = governing water depth
η = surface elevation
h = water depth
h_{min} = threshold water depth above which Stokes drift is taken into account

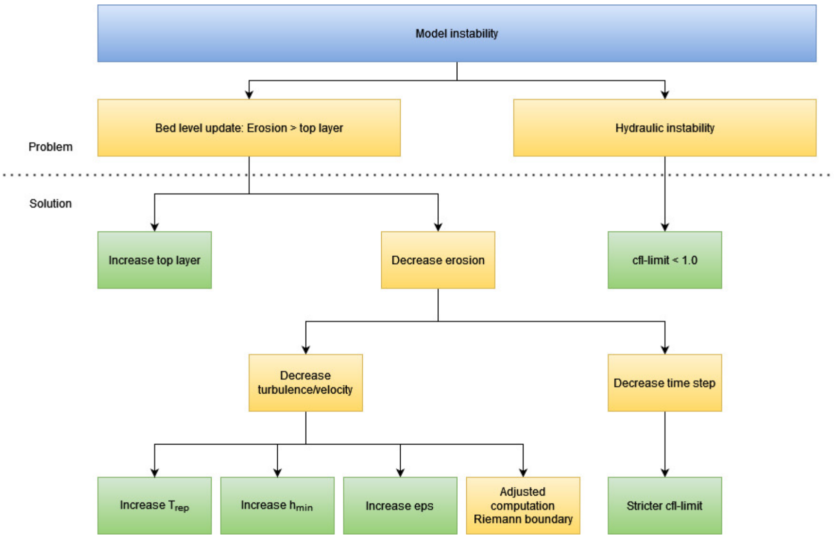

Figure C.1: Causes for XBeach model instability and preventative measures that can be taken. The green parameters can be specified in the model input. The adjusted implementation of the Riemann boundary is part of the XBeach executable.

Instability of the model can not only be prevented by decreasing the erosion per time step, but also by ensuring that the top layer of the model is able to accommodate the large erosion at the fixed point boundary. For the model runs a top layer of 2 cm was required, which did not correspond to the 2 mm sampling.

In the end, the combination of cfl-limit, T_{rep}, h_{min}, eps and the top-layer thickness determines whether the model is stable. For instance, a smaller top layer would have been possible if the time step was smaller or the velocities were lower. For this research, the settings were chosen based on practicality. By deciding to not make any changes to the cfl-limit, the computational time was kept within reasonable limits. For the other settings different combinations were tried and the settings that provided the best stable result were selected.

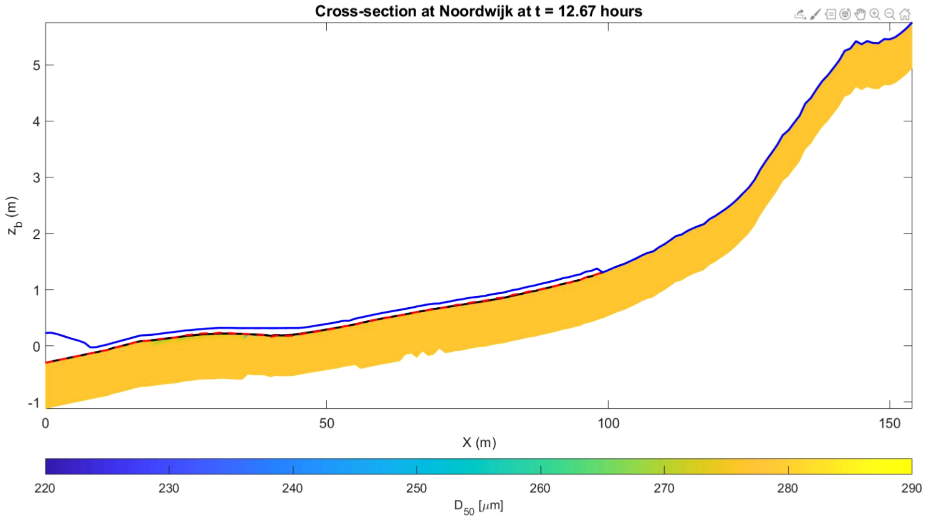

Figure C.2: A model run with both h_{min} and eps set at 0.10 m, resulting in an unrealistic layer of water that remains on the beach during low tide. The blue line is the surface elevation, the black line the bed level and the red dashed line the intitial surface elevation. Beneath the bed level the D_{50} over all the bed layers is shown with a colorbar.